Thermodynamic and conformational analysis of monomeric Aβ isoforms binding with A$\beta_{(1\text{-}42)}$ fibril - insights into the secondary nucleation of amyloidosis

Inaugural Dissertation

for the attainment of the title of doctor
in the Faculty of Mathematics and Natural Sciences
at the Heinrich Heine University Düsseldorf

presented by

SOUMAV NATH
from Kalyani, India

Düsseldorf, April 2022

From the Institut für Physikalische Biologie
at the Heinrich Heine University Düsseldorf

Published by permission of the
Faculty of Mathematics and Natural Sciences
at the Heinrich Heine University Düsseldorf

Supervisor: Prof. Dr. Alexander Kai Büll
Co-supervisor: Dr. Bogdan Barz

Date of the oral examination: May 12, 2022

Doctoral Dissertation

Thermodynamic and conformational analysis of monomeric Aβ isoforms binding with A$\beta_{(1\text{-}42)}$ fibril - insights into the secondary nucleation of amyloidosis

From the Institut für Physikalische Biologie
in the Mathematisch-Naturwissenschaftlichen Fakultät
at the Heinrich-Heine-Universität Düsseldorf
to obtain the degree of

Dr. rer. nat.

by

M. Sc. SOUMAV NATH
(Immatr. Nr. - 2810081)

Advisor:
Prof. Dr. Alexander Kai Büll
Co-Advisor:
Dr. Bogdan Barz

Düsseldorf, Germany
April, 2022

Life is the mode of action of Proteins
.....

Declaration

I, Soumav Nath, hereby assure that the present dissertation entitled **"Thermodynamic and conformational analysis of monomeric Aβ isoforms binding with A$\beta_{(1\text{-}42)}$ fibril - insights into the secondary nucleation of amyloidosis"** is written independently, without outside help and without using sources other than those specified. All of the outside works taken over directly or indirectly are marked as such. This dissertation was not submitted in any other doctoral procedure. I declare under oath that I have produced my thesis independently and without any undue assistance by third parties under consideration of the "Principles for the Safeguarding of Good Scientific Practice at Heinrich Heine University Düsseldorf". With this I am striving to obtain the academic degree Doctor of Natural Sciences (Dr. rer. nat.)

Düsseldorf, 15.06.2022

Place, Date

Soumav Nath

Signature

Acknowledgements

I would like to thank my PhD supervisor - Prof. Dr. Alexander Kai Büll, for his valuable guidance. Not only did he help me develop a methodical and critical thinking, but his enthusiasm and passion for science motivated me every day to face the challenges that research holds. Also, my co-supervisor Dr. Bogdan Barz for his utmost help and continuous support towards developing knowledge in computational research field from scratch. I also want extend my gratitude towards Prof. Dr. Birgit Strodel for being my mentor throughout the journey.

I am also very much thankful to Prof. Dr. Sara Linse for the fruitful collaboration and hosting me without any issues during the crisis moment of COVID-19 pandemic and Dr. Dev Thacker for utmost help with the scientific work throughout the research stay at Lund University, Sweden as part of collaboration.

I would like to thank all the people that are and were part of the AG Büll at HHU Düsseldorf, in particular Dr. Alessia Peduzzo, Dr. Nicola Vettore and Dr. Rebecca Sternke-Hoffmann.

I am grateful for the thorough and insightful comments of Dr. Lothar Gremer which was as fruitful as it was stimulating and the constant support of Jun.-Prof. Dr. Wolfgang Hoyer at the institute. I am also thankful to Dr. Sigrun Wegener-Feldbrügge from JUNO-HHU department for the utmost help with the administrative processes whenever required.

My special thanks are due to Mr. Sarnava Datta, Dr. Totan Mondal, Mr. Md Yusuf Ali, Mr. Mridhul Ram, Dr. Mohanraj Gopalswamy, Ms. Fatima Escobedo, Mr. Robin Backer, Dr. Pranav Joshi, Mr. Ci Chu and Dr. Hamed Shaykhalishahi whose role in my journey extends beyond their scientific contribution. A big thanks to Mr. Senthil Devan for maintaining the Indian community at HHU Düsseldorf.

These years would have been less bright if it wasn't for the wonderful atmosphere with wonderful team of staffs at the Institut für Physikalische Biologie. I extend my gratitude to all the past and present members of IPB. Last but not the least I want to thank DFG and COST for the funding opportunities and the Federal Ministry of Germany (BAMF) which played a pivotal role towards successful completion of my doctoral thesis from administrative perspectives.

Finally, I want to thank my parents, Mr. Arun Kumar Nath and Mrs. Uma Nath for their utmost love and continuous support.

List of Abbreviations

Abbreviation	Denomination
AD	Alzheimer's Disease
$IDPs$	Intrinsically Disordered Proteins
Aβ	Amyloid-beta
pE	Pyroglutamate
AβPP	Amyloid-beta Precursor Protein
$HREMD$	Hamiltonian Replica Exchange Molecular Dynamics
US	Umbrella Sampling
$CHARMM$	Chemistry at Harvard Macromolecular Mechanics
$OPLS$	Optimized Potentials for Liquid Simulations
$AMBER$	Assisted Model Building with Energy Refinement
$TIP3P$	Transferable Intermolecular Potential with 3 Points
SPC/E	Simple Point-Charge
$GROMACS$	GROningen MAchine for Chemical Simulations
VMD	Visual Molecular Dynamics
$DSSP$	Dictionary of Secondary Structure of Proteins
$STRIDE$	Structural Identification
NMR	Nuclear Magnetic Resonance
$QCM-D$	Quartz Crystal Microbalance with Dissipation
SPR	Surface Plasmon Resonance
CD	Circular Dichroism
$HFIP$	Hexafluoro-2-propanol
EDC	1-Ethyl-3-(3-dimethylaminopropyl)carbodiimide
NHS	N-Hydroxysuccinimide
ThT	Thioflavin-T Dye
K_{D}	Equilibrium Dissociation Constant
ΔG^o	Gibbs Free Energy
HPO	Hydrophobic-Side
HPI	Hydrophilic-Side

Abstract

Understanding the molecular basis for the plausible occurrence of cross-seeding secondary nucleation in AD pathology is important since the human brain contains various Aβ isoforms like pE-Aβ(3-42) peptide besides full-length Aβ(1-40/42) peptides. This thesis aims towards understanding the thermodynamic insights into the secondary nucleation of monomeric Aβ isoforms, pE-Aβ(3-42) & Aβ(1-42) peptide on the Aβ(1-42) fibril surface and investigating the process at the atomic scale through the analysis of monomeric conformations of these Aβ isoforms both in the presence/absence of fibril surface, leading a pathway towards understanding the mechanistic insights and developing potential molecular candidates for a therapeutic approach in AD pathology. Conformational analysis of IDPs using MD simulations depends on the choice of initial parameters. Chapter 2 establishes CHARMM36mW forcefield/HREMD method as the good choice of initial parameters for conformational analysis of Aβ(1-42) peptide, which not only shows greater resemblance with the observed experimental parameters but also for the first time showed that Aβ(1-42) monomer can significantly adopt the S-shaped fibril-like conformation which impels towards higher aggregation propensity of fibril elongation for Aβ(1-42) peptide *in-vivo*. Chapter 3 establishes the significant differences in the monomeric structure of pE-Aβ(3-42) peptide compared with that of Aβ(1-42) monomer obtained through computational study using the same set of parameters from Chapter 2. The pE-Aβ(3-42) monomer has more exposed hydrophobic residues, two unique salt bridges and a free D23 residue for inter-peptide interaction besides a higher β-sheet and helix propensity per residue compared to that of Aβ(1-42) monomer. This structural dissimilarity seems to be accountable for the observed higher aggregation propensity and toxicity of the pE-Aβ(3-42) monomer in bulk solution compared to that of Aβ(1-42) monomer. In Chapter 4, combined results from surface-based bio-sensing experiments show that the binding mode of pE-Aβ(3-42) to the Aβ(1-42) fibril surface is pH-dependent and it has a higher affinity compared to that of Aβ(1-42) monomer. Computational investigation reveals the possible binding sites for both Aβ isoforms, along with the comparison of free energy of binding and subsequent secondary structural changes between the two isoforms upon binding with the fibril surface. The outcomes rationalize the previously observed behaviour of inhibition of cross-secondary nucleation of pE-Aβ(3-42) monomers by Aβ(1-42) fibrils, through exclusive tighter binding of the monomer to the hydrophobic side of the fibril surface and increase in β-sheet propensity per residue compared to that of Aβ(1-42) monomer.

Together the whole thesis signifies the investigation of the mixed peptides system to understand the insights into the *in-vivo* mechanism of AD pathology and the potential of combined experimental-cum-computational methodology, using a wise choice of initial parameters for the later one which paves the pathway for the investigation through complementing each other in the manner of understanding the observable from the bulk solution to atomic-scale.

Contents

List of Figures

List of Tables

1 Introduction

1.1 Alzheimer's disease and amyloid-beta peptide

Alzheimer's disease (AD) is the notable and most common type of neuro-degenerative disease causing dementia affecting millions of people worldwide which is rising dramatically. The amyloid hypothesis proposes either 40/42 residue long β-amyloid (Aβ) peptide as the main cause of the disease since Aβ peptide misfolds extracellularly and are accumulated in the senile plaques of the human brain and the misfolded tau protein deposits intracellularly in neurofibrillary tangles causing memory loss and confusion, which results in personality and cognitive decline with time [57, 88, 117, 122]. In 1907, the first case of fatal progressive dementia associated with the AD pathology which is diagnosed using modern day techniques was described by the renowned psychiatrist Alois Alzheimer; after whom the disease was named. With the development of modern day science, Aβ peptide was identified as the major components occurring in the amyloid plaques of patients diagnosed with AD and Down's Syndrome in 1984 [2, 91]. Mainly, two categories of AD cases have been established - the (pseudo-) sporadic late-onset AD (LOAD) and early-onset familial AD (FAD); besides the apolipoprotein E (ApoE) gene on chromosome 19 has also been considered to be a major genetic risk factor. The usual suspects for the roots of AD cases are believed to be the amyloid precursor protein (AβPP) and presenilin (PS) sub-units [116, 115]. The sequential proteolytic cleavage of a larger glycoprotein AβPP, is considered to be the main cause of accumulation of Aβ peptides in human brain and PS resembles the active site of the main proteolytic enzyme invloved in the generation of Aβ peptides in-vivo.

The AβPP is the type 1 membrane glycoprotein expressed in many tissues, especially in the synapses of neurons - plays significant roles in the biological activities like intracellular transport, neuronal development, signaling, iron export and neuronal homeostasis. The neuronal dysfunction caused by different AβPP cleavage products, play the central role in Alzheimer's disease (AD) pathogenesis. AβPP consists of a large extracellular glycosylated N-terminus and a shorter cytoplasmic C-terminus, integrated in a single membrane-spanning domain, acts as the precursor molecule which upon cleavage by β-secretases and γ-secretases produces the Aβ peptide consisting of 37 to 49 amino acid residues [320, 93, 58, 239, 148, 145]. Biologically, the cleavage of APP occurs either by the α-secretase (nonamyloidogenic pathway) or β-secretase (amyloidogenic pathway) releasing the sAPPα or sAPPβ from the cell surface and leaving either an 83-amino-acid or 99-amino-acid C-terminal AβPP fragment (C83 or C99), which is the main precursor for the γ-secretases cleavage sites; ultimately producing full length Aβ(1-40) or Aβ(1-42) peptides along with AβPP intracellular domains (AICD). The production of sAPPα increases in response to the neuronal activity of human body which suggests that dominantly the α-secretase cleavage of AβPP increases in the human

brain. The aggregated species of Aβ peptides formed as a result of amyloidogenic pathway cleavage of AβPP, in the form of amyloid fibrils are found as the primary component of amyloid plaques in the brains of Alzheimer's disease patients [127, 238, 308, 100]. However, a diverse range of clinical trials centered on amyloid hypothesis and targeting the depletion of full length Aβ peptides generation or neutralizing it by immunotherapy towards finding a solution to AD pathology have failed intensely. It is thus a challenge to reconcile the Aβ(1-40/42)-centric amyloid hypothesis which is possibly a simplified view of a complicated systems involved in the AD pathology.

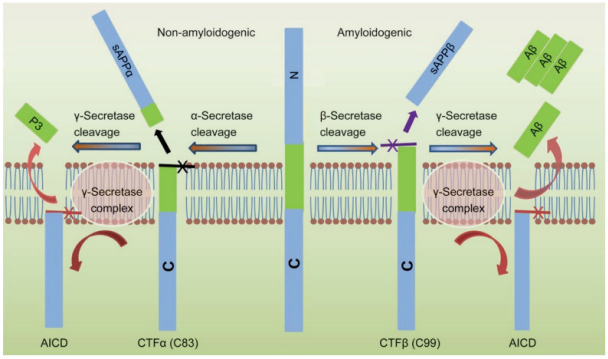

Figure **1-1**: Proteolytic mechanisms in human AβPP. Proteolysis of human AβPP in the non-amyloidogenic and amyloidogenic pathways. The sequential processing of APP by membrane bound α-secretases, which cleave inside the Aβ domain to yield the membrane-attached α-C terminal fragment CTFα (C83) and the N-terminal fragment sAPPα, is referred to as non-amyloidogenic processing of AβPP. γ-secretases then cleave CTFα to produce extracellular P3 and the AβPP intracellular domain (AICD). Membrane-bound β- and γ-secretases work together to process AβPP in an amyloidogenic manner. AβPP is cleaved into membrane-tethered C-terminal fragments β (CTFβ or C99) and N-terminal sAPPβ by β-secretase. CTFβ is then cleaved into the extracellular Aβ and intracellular AβPP domains by γ-secretases (AICD). Adapted with permission from [62].

Contribution of the Aβ-derived fragments that are present in the amyloid plaques as derived from the analysis of brain samples of non-demented control cases, pathological aging (prodromal phase of AD), and AD is believed to be playing an important role in the amyloid pathology. Furthermore, several aspects of physiological AβPP processing e.g. Eta (η) cleavage site on the AβPP giving rise to a subset of new Aβ fragments (A$\eta\alpha$, A$\eta\beta$ and ηCTF) as a result of cleaving action by matrix metalloproteinase enzyme MT5-MMP also thought to be contributing towards the AD pathology [195, 161]. Although the brain analysis found different types of Aβ fragments including C-terminally and N-terminally modified isoforms; but the N-terminal truncated Aβ fragments have been found in major portion in the senile plaques, hypothesized to be generated via primary cleavage of AβPP protein and post-translation modification of Aβ peptide [254, 159]. Out of the various N-terminally truncated isoforms of Aβ that have been found in the brain analysis, the major fragments include Aβ(2-X), Aβ(3-X), Aβ(11-X), Aβ(17-X) and the pyroglutamate-modified Aβ beginning with the lactam ring instead of glutamate in position 3 of Aβ (pE-Aβ3-X) has also been described.

pE-Aβ(3-X) has been found similar in quantities to the full-length Aβ in the senile plaques, diffuse plaques along with the vascular wall [129, 248]. In the patients with AD, the pE-Aβ(3-42) peptide has appeared to be a dominant isoform in the hippocampus and cortex inside the diseased brain. pE-Aβ(3-X) peptide formation is postulated to be a two-step process involving removal of the first two Aβ residues Asp–Ala leading to the N-terminal truncation followed by the cyclization of the glutamyl in position 3 the lactam ring named pyroglutamate through an enzymatic process, highlighted several enzyme candidates responsible for this post-translation modification of Aβ peptides. Several studies have pointed towards a mixed action of exopeptidase enzymes, notably aminopeptidase A (APA) and member of the dipeptidyl peptidase family enzymes (DPP) are responsible for the releasing of first two residues from the full-length Aβ peptides leading to the formation of Aβ(3-X) fragments. Pharmacological and genetic evidences have indicated that the the glutamate residue at position 3 after the cleavage of first two residues from Aβ peptide is converted into pyroglutamate moiety through enzymatic cyclization mechanism with the acyltransferase enzyme named glutaminyl cyclase (QC), which has been found to be up-regulated in AD-affected brains although in healthy brains this remains unevenly distributed [3, 272, 150]. In addition to these isoforms several other highly abundant truncated Aβ variants have been also detected namely Aβ(4-X), having the same level of toxicity as that of pE-Aβ(3-X) or Aβ(1-42) but little is known about the enzymatic cycle responsible for the generation of these variants.

Although Aβ peptide has been best described as intrinsically disorder protein (IDP) having the disordered monomer conformations but studies have found that both Aβ(1-40) & Aβ(1-42) bias towards having β-strand character in the CHC core and C-terminus, with β-turns occurring at specific positions within the monomer. The backbone H_α, C_α, and C_β chemical shifts as obtained from the solution-state NMR studies targeting Aβ(1-42) monomer suggest the β-strand propensities in the CHC, within the residues I31−V36 and V39−I41, as well as turn character at D7−E11 and F20−S26; characterizing Aβ(1-42) best as collapsed coil ensemble rather than a unique structure [275, 183]. Far-UV CD spectra for both Aβ(1-40) and Aβ(1-42) monomers also suggest a bias towards strand content but the signals are dominated by random coils structures. Interestingly, secondary structure for Aβ peptide is dependent on sample preparation methods since CD analysis using different preparation methods have reported 12-25% of β-strand content and 39% of α-helix content at pH 7.5 and 295 K [170, 224]. Aβ(1-42) monomer has been also found to be possessing residual secondary structure since ^{15}N spin NMR relaxation data revealed Aβ(1-42) monomer having more rigidity at the C-terminus than Aβ(1-40) in terms of both side-chain and backbone dynamics [292, 348]. Atomic-scale characterization of Aβ monomeric state is thought to be an important aspect to understand the assembly process of Aβ into disease-causing toxic oligomers and insoluble amyloid fibrils, which could be crucial for designing drug candidates towards the treatment of AD. Destitute of unambiguous stable native states featuring the intrinsically disordered property, in addition to the high aggregation propensity, has nullified the experimental efforts to characterize the Aβ(1-40/42) monomeric structures. A wide variety of computational techniques have been used to more thoroughly investigate the conformational properties of these peptides, encouraging the challenges and limitations inherent to the current experimental techniques for studying these polymorphic, aggregation-prone Aβ

monomers. Extensive simulations for Aβ have been performed over multiple microseconds using explicit and implicit solvent models using REMD, simulated tempering and metadynamics for enhanced sampling and escaping energy minima [138, 304, 236, 180, 5, 33]. As the simulation results of intrinsically disordered proteins (IDPs) e.g. Aβ, depend highly on the set of mathematical parameters (force-fields) describing the interaction energy of the peptide itself and with the surrounding molecules such as solvent; so different force-fields have been used till now to describe the Aβ monomer conformation trying to fit with the observed experimental parameters. Among these widely used force-fields for biomolecular simulation with Aβ includes OPLS-AA, AMBER99sb and its variants, CHARMM22* and it's variant etc. with the frequently used water models include the three-site models TIP3P and SPC/E and the four-site models TIP4P and TIP4P-Ew [168, 134, 43, 185, 237, 156, 133, 140].

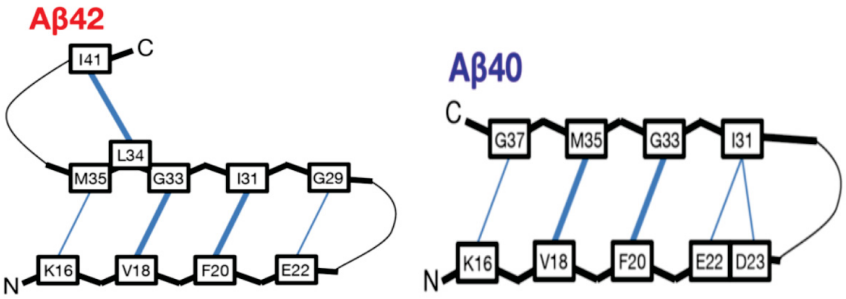

Figure **1-2**: β-Hairpin models for Aβ(1-42) and Aβ(1-40) monomers based on the most populated cross-region backbone hydrogen bonds and secondary structure proclivities in the ensemble determined from MD simulations. A bold line is drawn between residues that exhibit a large population of donor to acceptor and acceptor to donor backbone hydrogen bonds. As high-ranking centroid structures, sampled conformations that fit these models exist. Adapted with permission from [218].

Analysis of the all-atom REMD simulations with OPLS-AA/TIP3P reveals Aβ(1-42) monomer having β-hairpins between the residues L17-A21 and I31-V36 along with an extra β-hairpin occurring between V39-A42 compared to Aβ40 monomer. Characterization of Aβ(1-42) monomer using AMBER99sb/TIP4P-Ew force-field parameter sets along with the studies of Aβ(1-42) pentamers also revealed the similar double β-hairpin conformation of the Aβ(1-42) monomer suggesting that the REMD-predicted β-hairpins may act as nucleation sites for higher order Aβ(1-42) assembly, having the structural similarity to the higher order aggregate models for Aβ(1-42). NMR-guided simulations of Aβ(1-40) and Aβ(1-42) revealed very different conformational states, with the C-terminus of Aβ(1-42) being more structured and residues 31-34 and 38-41 forming a β-hairpin that reduces C-terminal flexibility, which may account for Aβ(1-42)'s greater proclivity to form amyloids than Aβ(1-40). Different approaches towards simulation with Aβ42 monomer have been taken place aside the all atom force-field/REMD simulations such as multiple-reservoir replica exchange (MRRE) simulations with AMBER99sb/TIP4P-Ew and analysing with ENSEMBLE package, REMD with the six-bead CG OPEPv3 model, Monte Carlo simulated annealing with the all-atom PROFASI force field, discrete MD (DMD) simulations coupled to a four-bead CG model where all of them mostly showed Aβ(1-42) as random coil structure and partially agreed with the β-turn model as observed with the all atom simulations [262, 292, 291, 166, 32, 340, 144, 28].

Most of the atomic-scale characterization of Aβ(1-42) using simulation studies remain highly divergent probably due to the differences in the simulation parameters, extent of sampling and trajectory analysis. A prior need to develop simulation parameter sets for a consistent atomic-scale characterization of Aβ(1-42) monomer aligning the observed experimental parameters with the development of experimental tools is required with the given circumstances.

Although, amyloid cascade hypothesis figures out the deposition of amyloid fibrils of dominant wild type Aβ peptides as the key event in the AD pathogenesis but several studies have also generated the controversy through figuring out other processes triggering the amyloid plaque formation in the AD brain which includes Aβ oligomer formation, disturbance in ion homeostasis, mitochondrial toxicity and oxidative stress, synapto-toxicity, disturbed signal cascades and metabolism, tau hyper-phosphorylation and NFT formation, inflammatory responses, neurotoxicity, and complex neuronal dysfunction; besides the events of capability of co-aggregation and cross seeding of various Aβ-variants generated either through the different cleavage process of AβPP or post-translational modifications along with their interactions with other proteins present in the human brains such as AβPP itself or Tau [104].

Understanding the insights of these several observed pathways of amyloid plaque formation is relevant towards identifying the key players in the Aβ aggregation pathway and establishment of an unequivocal cascadic sequence of AD pathogenesis. Of these, co-aggregation events between various Aβ-variants present in-vivo have gained attention since some of the Aβ-variants such as pE-Aβ(3-X) have been found to be highly aggregation-prone and toxic compared to that of wild-type Aβ(1-40/42) peptides whereas other variants remains inactive towards aggregation or show less propensity; so proper identification and separation of toxic Aβ-variants is thought to be crucial towards therapeutic approach in AD pathology. Also, atomic-scale investigation to understand the dominant conformations of these toxic Aβ-variants and figuring out the thermodynamic parameters behind the observed biophysiochemical properties of these Aβ-variants and their co-aggregation with other species of generated by their isoforms are crucial towards developing drug candidates aiming to combat AD pathology in near future.

1.2 Protein misfolding and amyloid fibril formation

Protein misfolding is the formation of an altered protein fold compared to the native structure of a protein, which can occur as the results of a spread of events, including: mutations within the gene sequence that lead to the assembly of a protein that's unable to adopt the native fold, errors in transcription or translation processes that lead to the assembly of modified proteins that are unable to properly fold, failure of the chaperone machinery, errors in post-translational modifications or intracellular protein trafficking, structural modifications caused by environmental changes, seeding and cross-seeding by pre-formed aggregates etc. Furthermore, protein misfolding generally results in protein aggregation with specific interactions occurring between intermediate molecular species that tend to form large ordered aggregates, which may evolve into amyloid fibrils that deposit as insoluble extracellular

plaques or intracellular inclusions. Proteins exist in a variety of states, including disordered, partly unfolded, and various aggregation assemblages; besides their natural structure, which is closely linked to it's functional aspect. [7, 72, 164, 259, 197, 64].

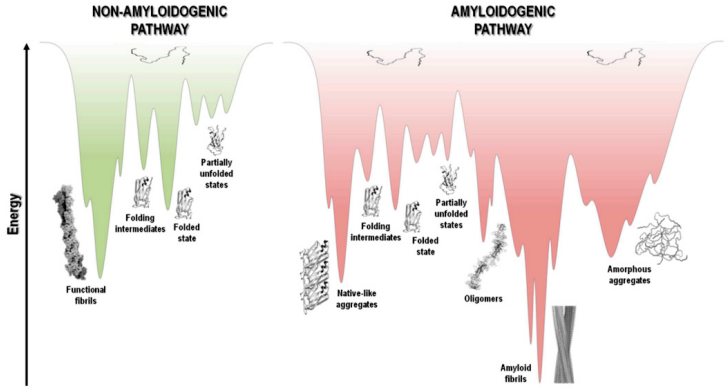

Figure **1-3**: The funnel-shaped energy landscapes for protein folding (nonamyloidogenic route, green) and aggregation are depicted in this diagram (amyloidogenic pathway, red). Protein energy landscape roughness is depicted on the surface, which shows the polypeptide chain's potential conformational states. Unfolded, partly unfolded, and folded species are all possible suspects. As long as they are prone to forming intermolecular contacts and aggregation landscape - amorphous aggregates, amyloid fibrils and native-like aggregates are formed as a result of this interaction. Adapted with permission from [24].

The folding energy landscape available to every polypeptide chain includes a various set of conformational states additionally as a plethora of pathways to the folded state; for the case of short polypeptide sequences, the energy landscape is often a smooth funnel-shaped surface where the polypeptide chain folds quickly towards one folded state. Larger proteins, on the opposite hand, have rougher energy landscapes with local minima and a population of intermediate states that inter-convert to the lower energy folded states [17, 194, 87]. Fig. **1-3** depicts the unfolded state of the polypeptide chain at the top of the funnel, which has a high Gibbs free energy and a high conformational entropy where the polypeptide chain folding reduces the number of conformational states and thus the conformational entropy. Concurrently, the hydrophobic collapse and increase in the number of intramolecular contacts cause a decrease in free energy toward the native state which occupies the global free energy minimum, yielding the folded state's required conformational stability. Changes in amino acid sequence and/or chemical or biological conditions such as pH, temperature, ionic strength, pressure, agitation, shear forces, surface contact, and a variety of other variables might shift the energetic balance towards a different free energy minimum. This is illustrated in Fig. **1-3**, where, in addition to the common folding funnel for a protein, an aggregation funnel is also depicted. In terms of protein aggregation, the funnel-shaped free energy surface is potentially rougher and more complex because the energy landscape encodes not only the relative stability of unfolded, partially unfolded and folded states but also the stability of amorphous aggregates, β-sheet-rich amyloid fibrils and native-like aggregates [316, 171, 342].

Folding, unfolding, partial folding/unfolding, conformational changes, the formation of intermolecular interactions and fibril nucleation, elongation and stationary phases are all involved in protein aggregation. Protein aggregation states can be formed not only by amyloidogenic intermediates but also by denatured and native states, with polypeptide chains establishing critical contacts with neighboring molecules via intermolecular interactions. Aggregated states are generally thermodynamically and kinetically advantageous and it is a delicate balance of forces that tip the processes toward a native soluble state or any type of aggregated state. Most polypeptide chains appear to form extended β-sheet structures and thus amyloid aggregates under the right "stress" conditions [297, 315, 296, 295, 169, 6, 79, 96]. Because of the heterogeneity of fibrillar morphology, the energy landscape of protein systems forming large aggregates as shown by numerous peaks corresponding to different conformational states. Under the similar experimental conditions, a large number of polymorphic fibrils with distinct morphologies can form at the same time, emphasizing the aggregation pathways' complexity and multiplicity. The mature fibril energy minimum is deeper and sharper than the natural state of a protein (Fig. **1-3**), as evidenced by the fibrillar state's high stability. The driving forces for both protein folding and aggregation are primarily hydrophobic in nature with contributions from electrostatic and polar interactions as well as hydrogen bonds. For amyloid fibrils, the cross-β motif conformation is primarily stabilized by polar interactions caused by intermolecular H-bonds, while intermediate aggregated species are formed by hydrophobic and electrostatic interactions. In the late 1990s, proteins completely unrelated to well-known amyloid diseases were discovered to form amyloid-like aggregates or fibrils in vitro under specific experimental conditions. As previously stated, many if not most, polypeptide chains can form amyloid under the right conditions. As a result, the term "amylome" was coined to describe all proteins capable of forming amyloid-like fibrils. Some authors believe that the fibrillar amyloid state is a standard state that every polypeptide chain can achieve under the right conditions and that this state is the thermodynamic ground state. The conformation of amyloid fibrils is the universal global free-energy minimum for polypeptide chains.

Structure of amyloid fibrils

Since the invention of the cross-β motif, numerous studies are conducted to characterize the structure of amyloid fibrils using various experimental techniques. All of those data have helped to reveal the structure of amyloid fibrils on a multi-scale basis, in addition as how individual protein sub-units can form cross-β structures. The cross-β motif may be a structural feature shared by all amyloid fibrils, it's characterized by extended β-sheets with individual β-strands arranged perpendicular to the fibril main axis. Amyloid fibrils are unbranched structures with diameters starting from 2 to 20 nm and lengths starting from some micrometers to many micrometers [14, 192, 249]. X-ray fiber diffraction studies first demonstrated the presence of a repeating cross-β structure within the late 1960s, and later synchrotron X-ray diffraction studies confirm that amyloid fibrils from different amyloid proteins display the identical cross-diffraction pattern. A meridional reflection at 4.7–4.8 Å similar to the H-bonding distances found between paired carbonyl and amide groups in adjacent β-strands and an equatorial reflection at 6–11 Å like the space observed between

stacked β-sheets are observed in characteristic amyloid fibril diffraction patterns. Amyloid fibrils of varied origins share a typical cross-spine formed by a pair of β-sheets with their facing side chains interdigitated in an exceedingly steric zipper. Steric zippers are thus short peptide segments that function the structural foundation for an amyloid fibril's hierarchical assembly. It is thus thought that stacks of steric zippers are required to make the cross-β spine of the amyloid protofilament which is the fundamental unit of the mature fibril, while the remainder of the polypeptide chain assumes either a native-like or random coil conformation during a peripheral position to the spine. Nonetheless, there is also significant differences within the structural arrangement of steric zippers. Sheet symmetry is produced

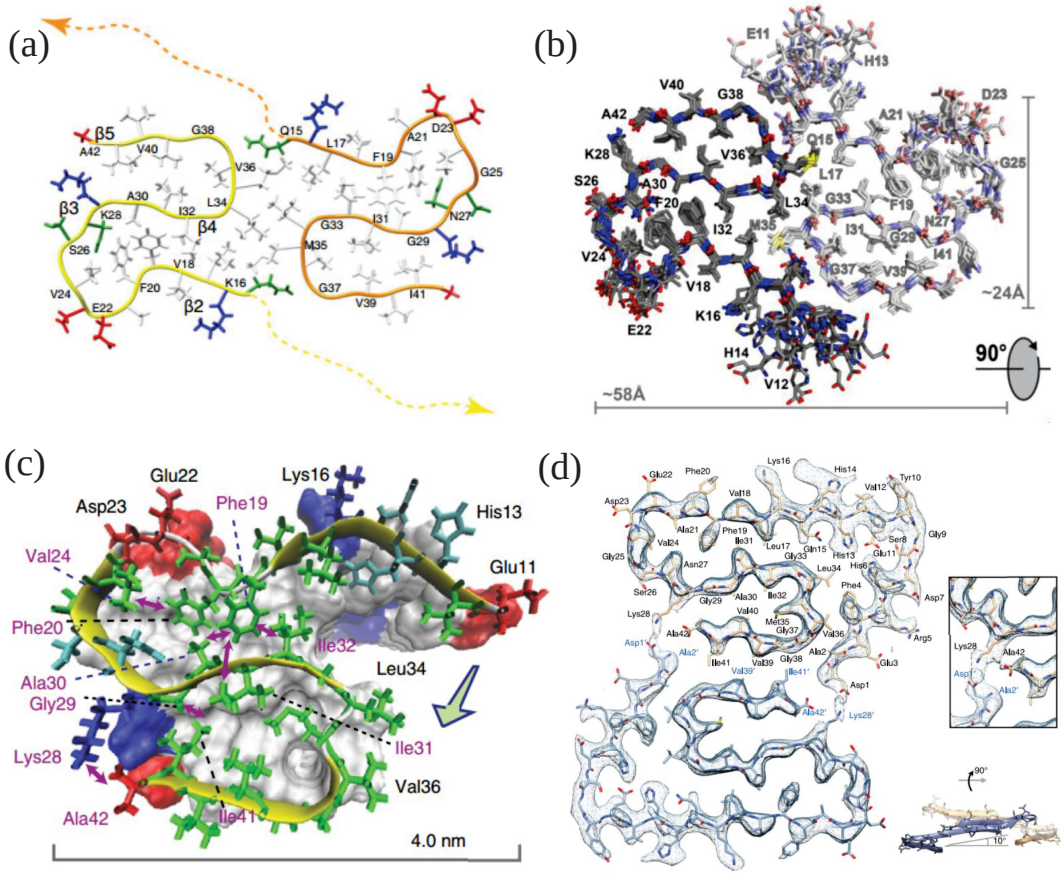

Figure **1-4**: Different alloforms of fibril structures as observed with *in-vitro* sample for Aβ(1-42) monomeric peptide: (a) Double-filament Aβ(1-42) fibril in physiological pH with synthetic peptide having S-shaped monomeric sub-units as observed by Marielle *et. al.* [336], (b) Double-filament Aβ(1-42) fibril in pH 8.0 environment with recombinant peptide having S-shaped monomeric sub-units as observed by Colvin *et. al.* [68], (c) Single-filament Aβ(1-42) fibril in pH physiological pH having triple β-strand monomeric sub-unit as observed by Xiao *et. al.* [338] and (d) Double-filament Aβ(1-42) fibril with LS-shaped monomeric sub-units in acidic pH environment with traces of organic solvent as observed by Gremer *et. al.* [121]. In all structures observed in physiological conditions, the Aβ(1-42) fibril is found to be having disordered N-terminus.

by the assembly of strands during a sheet (parallel versus antiparallel and antifacial versus equifacial); each of those four β-sheet patterns is capable of self-pairing to make cross-spines [92, 178, 193, 252, 209, 89].

Through the utilization of innovative research methodologies like cryo-electron microscopy (cryo-EM) and solid-state NMR (ss-NMR) within the field of structural biology, it's been found that the amyloid fibrils derived from the identical precursors are demonstrated to possess varied shapes in several disorders, further as varying seeding qualities, rates of dissemination, and neuropathological patterns. Polymorphism can come about in an exceedingly type of ways; firstly, it can entail several packing configurations of the identical protofibril. A second type of polymorphism can develop when one section of a protein sequence adopts a standard structure while other regions adopt distinct structures. And a third variety of polymorphism comprises both diverse protofilament packing and a partly shared fold. When both the protofilament structure and packing interactions differ, the fourth and most severe sort of polymorphism arises. It's unknown what drives the fibril's structural diversity; mostly it is perceived that it would be caused by the inherent features of the polypeptide sequence, the presence or lack of post-translational modifications, interactions with cofactors or cellular components, the character of the environment (pH, ionic strength, etc.) or the cell type within which the amyloid fibrils are generated [111].

For Aβ peptides, dominantly the second type of polypormorphism is generally found depending on the environmental conditions either *in-vitro* or *in-vivo* and the type of sample preparation methods. Several studies have identified multiple structural models for Aβ(1-40) amyloid fibrils. While these models have slight variances, they do share several characteristics. These include the existence of only a single turn and prolonged β-strands, which

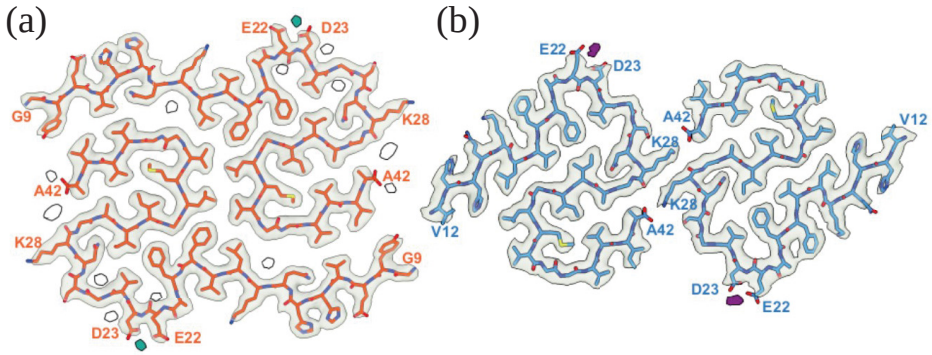

Figure **1-5**: Alloforms of fibril structures as observed for Aβ(1-42) monomeric peptide with *in-vivo* sample from dead-patients with AD: (a) sample from sporadic AD shows Double-filament Aβ(1-42) fibril with twisted-S shaped monomeric sub-units and (b) samples from familial AD shows Double-filament Aβ(1-42) fibril with S-shaped monomeric sub-units having interactions through opposite faces as observed by Yang *et. al.* [349]. These Aβ(1-42) fibril structures observed is very much different from that of the Aβ(1-42) fibril structures observed under *in-vitro* conditions.

comprise residues 10-40, with the first 10 residues invisible to the experimental methodologies used. Reif and colleagues, on the other hand, claimed that they seeded an Aβ(1-40) sample and obtained a single form with two sets of chemical shifts, leading them to infer that the fibril's basic sub-unit is an asymmetric dimer. From residues 12 to 40, this dimer has a single pair of resonances visible, whereas the other is visible from residues 21 to 38. The Osaka mutant, on the other hand, contains many twists and has 39 residues and all of the residues in this amyloid fibril were reported to be integrated into the fibril core, with the N-terminus creating interactions with the peptide's central region [235, 27].

For Aβ(1-42) peptide, under normal pH studies revealed the common occurrence of double filament protofibrils twisted together giving rise to an overall cross-β sheet domain, which consists of an unstructured N-terminus containing the S-shaped motif for each of the monomeric protofibrilar sub-units. Each monomeric subunit's hydrophobic side chains are buried inside the fibril core structure and the S-shaped sub-unit is stabilized by an intramolecular K28-A42 salt bridge pair, as opposed to the intramolecular K28-D23 salt bridge seen in the Aβ(1-40) fibril structure [336, 68]. Furthermore, Aβ(1-42) fibril has been shown to contain a single S-shaped monomeric sub-unit with triple β-strands, which is similar to one of the monomeric sub-units from the previously mentioned double filament models [339]; however, the discrepancy in results has been attributed to a lack of sufficient mass-per-length (MPL) measurements from STSM data [336]. The structure of the Aβ(1-42) fibril at lower pH revealed that the double filament protofibrilar helical pitch changes and each of the sub-units achieve an LS-shaped motif, resulting in a different polymorph with a structured N-terminus from each monomeric sub-unit participating in the formation of the fibril core and stabilization through two unique D1-K28 salt bridges [121]. However, a recent approach for evaluating the structure of Aβ(1-42) fibrils in the *in-vivo* environment, which was taken from the AD patients, indicated that Aβ(1-42) has a completely different structure from the two structures solved in-vitro at different pH environments. For sporadic AD samples, Aβ(1-42) was discovered to have a double protofibrillar filament model with twisted-S shape monomeric sub-units and an extended disordered N-terminal region; and for familial AD samples, Aβ(1-42) was discovered to have a double filament structure with S-shaped two monomeric sub-units, which are stabilized by interacting through the opposite side of the S-shaped fold, primarily through the intermolecular K28-A42 interaction [349]. Although the amyloid fibril generated from the Aβ(1-42) monomeric peptide has a wide range of polymorphisms depending on various factors, the C-terminus of the fibril from all fibril models is found to be structured, forming the S-shaped monomeric sub-units that are predominant in protofilament structures. Recently, the occurrence of polymorphism in the Aβ(1-42) fibril structure derived from *in-vivo* different from that of fibril poly-morphs derived from *in-vitro* environment have bolstered the scientific investigation and open challenges towards exploring the insights into the mixed-system of Aβ isoforms and their roles in the amyloid cascade hypothesis.

Mechanisms of amyloid fibril formation

Multiple aggregation mechanisms exist in amyloid systems, reckoning on the ensemble of

co-existing amyloidogenic conformations and environmental factors. Several aggregation mechanisms and pathways have thus been described in regard to protein sequence, conformational states adopted by the amyloidogenic monomer and experimental conditions (e.g. temperature, pH, protein concentration, and solvent effects).

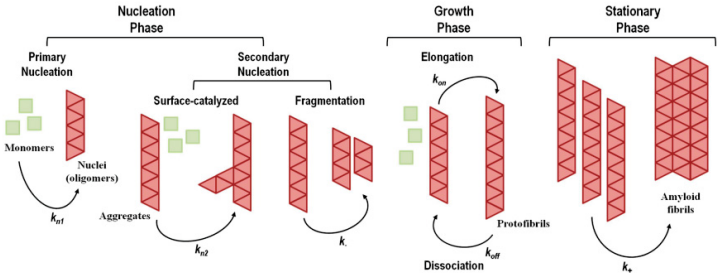

Figure **1-6**: Nucleation-dependent processes (including primary and secondary nucleation) and nucleation-independent mechanisms (including primary and secondary nucleation) are represented in a generic model for amyloid fibril production (absence of nucleation). Rate constants are represented by k_{n1}, k_{n2}, k, k_{on}, k_{off} and k_+. The development of protofibrils into mature amyloid fibrils with various morphological features and a high level of polymorphism occurs during the stationary phase. Adapted with permission from [24].

Aggregation processes occur over a good duration, spanning several orders of magnitude with conformational changes occurring in milliseconds and particle formation observable with the eye occurring in days, weeks or months. The understanding of the mechanisms of amyloid formation likewise because the characterization of the foremost relevant molecular species involved is critical for developing new rational therapeutic strategies for amyloid diseases. Kinetics of amyloidogenic protein aggregation process is highly dependent on the concentration of protein which may reflect a nucleation-dependent or a nucleation-independent process along with the secondary pathways of aggregation behavior.

Nucleation-independent mechanism

$$M + M \xrightarrow{k} M_2$$
$$M + M_2 \xrightarrow{k} M_3$$
$$M + M_3 \xrightarrow{k} M_4$$
$$\dots$$
$$M + M_n \xrightarrow{k} M_{n+1}$$

Figure **1-7**: The sequential monomer (M) addition method for protein aggregation via a nucleation-independent approach with similar equilibrium constants (k).

The isodesmic or linear polymerization mechanism of protein aggregation is exemplified by the best possible mathematical model for describing the formation of spherical oligomers or linear multimers. This model is distinguished by an infinite number of steps with identical rate constants (k) independent of aggregate size, leading to an exponential polymerization curve with no lag phase and once aggregation begins, the method descends into polymerization. During this case, aggregation proceeds through a series of multiple energetically favorable steps during which the sequential addition of amyloidogenic monomers to the growing aggregate is energetically favorable without the necessity for a multimeric nucleus. In general, seeding has no effect on the speed of aggregation in an exceedingly downhill polymerization process. This model, however, ignores other aggregation processes which will alter the amount, size and shape of the oligomeric species. As a results of these factors, this model occasionally predicts incorrect length distributions of amyloid fibrils at equilibrium. Nonetheless, this kinetic model has been wont to study the effect of mutations on the speed of amyloid fibril formation [334, 76, 341, 266]. This aggregation mechanism has been observed in transthyretin, among amyloid-peptide variants, four-repeat domain of tau (Tau4RD), β2-microglobulin, human and bovine serum albumins, HypF-N, FF domain, human muscle acylphosphatase, apolipoprotein C-II, and several other SH3 domains [354, 265, 227, 274].

Nucleation-dependent mechanism

The nucleation-dependent mechanism of amyloid formation, also called nucleation–elongation polymerization, encompasses a typical sigmoidal shape curve as a function of time and consists of three consecutive steps: (i) initial lag or nucleation phase, (ii) elongation, growth, polymerization or fibrillation phase and (iii) equilibrium, stationary or saturation phase.
The nucleation phase is characterized by the formation of transient, critical nuclei that may later act as seeding intermediates for extra monomeric subunits to latch onto, leading to the formation of oligomers with cross-β structure. Because the speed constants for monomer addition and dissociation are similar at this stage, the process of nucleation is slow and therefore the rate-limiting step in fibril formation. The addition of pre-formed aggregates or fibrillar species, called seeding, can shorten or eliminate the nucleation phase. Monomers,

$$nM \xrightarrow{k_{nucleation}} A_n$$

$$M + A_n \xrightarrow{k_{growth}} 2A_n$$

Figure **1-8**: M is the monomer and A is the transient nucleus aggregate in the minimalistic Finke–Watzky method for protein aggregation through a nucleation-dependent process. The nucleation and growth rate constants are $k_{nucleation}$ and k_{growth}, respectively.

nuclei and oligomers still interact during the elongation phase forming prefibrillar structures that rapidly grow to make ordered fibrillar structures referred to as protofibrils which can be a faster and more thermodynamically favorable process because it produces more stable

protofibrils. Finally, within the saturation phase, where monomer concentration is low and comparatively constant, protofibrils are assembled into mature amyloid fibrils with varying morphological structures and levels of polymorphism [97, 26, 226, 152, 31]. The aggregation model of Finke–Watzky is the mostly proposed models for nucleation–elongation polymerization that has been applied to over 40 different aggregating proteins. The Finke–Watzky model, as illustrated, consists of two simple steps: (i) nucleation and (ii) growth; although this model has some limitations which include: (i) an outsized number of aggregation steps are reduced to two basic steps, (ii) the speed constants, $k_{nucleation}$ and k_{growth} are average rate constants that are unaffected by the scale of the aggregating species, (iii) a better kinetic order in [M] is also kinetically hidden, particularly within the nucleation step, (iv) Growing polydisperse aggregates are concealed by the descriptor A_n, (v) the descriptor A_n can Processes like fragmentation can even be hidden. However, the ease of use and high quality of the fits obtained in many practical examples indicate that the Finke–Watzky two-step mechanism captures the main kinetic properties and is a good general kinetic model for nucleation-growth aggregation [198, 25].

Primary nucleation mechanism

Primary nucleation could be a critical step in an exceedingly style of oligomerization mechanisms within the amyloidogenesis cascade and it includes the initial formation of amyloidogenic nuclei without contributions from pre-formed oligomers. There are two styles of primary nucleation mechanisms: homogeneous and heterogeneous. Homogeneous primary nucleation involves the aggregation of monomeric subunits in bulk solution, whereas heterogeneous primary nucleation involves the association of monomeric subunits on the surface of a special object, like the wall of a reaction container, other proteins, phospholipid bilayers or the air–water interface. The nucleated polymerization (NP) mechanism is the most elementary structural manifestation of a primary nucleation mechanism. In this case, amyloidogenic monomers aggregate to make the nucleus, which then grows into amyloid protofilaments and protofibrils via an elongation process that primarily involves monomer addition. At low protein concentrations, this can be the preferential mechanism that favors the presence of monomeric species in solution. However, multiple conformationally heterogeneous oligomers and transient intermediate species are observed in several instances during fibril formation, which NP mechanisms cannot explain. A nucleated conformational conversion (NCC) mechanism has been proposed in these cases; as intermediates, NCC consists of structurally organized oligomers capable of conformationally transitioning into cross-β dominated fibrillar species. At higher protein concentrations, the formation of these conformationally dynamic oligomers may be favored and they undergo a rate-limiting conformational change to form protofibrils and then amyloid fibrils [30, 153, 98, 95]. This type of nucleation was observed in the yeast prion protein (Sup35) as well as in amyloid-peptide variants, the SH3 domain, the Ure2p yeast prion, polyglutamine (polyGln) peptides and lysozyme.

Secondary nucleation mechanism

A simple homogeneous primary nucleation mechanism isn't always observed, despite being

conceptually appealing and observed in several instances. Several studies have shown that straightforward homogeneous nucleation cannot account the experimental aggregation kinetics data. Other nucleation mechanisms and events, like fibril-catalyzed secondary nucleation (a monomer-dependent process) and fibril fragmentation (a monomer-independent process), both contribute to the formation of latest aggregation nuclei, don't seem to be considered in simple homogeneous primary nucleation. Monomer-dependent secondary nucleation is described as a process in which the creation of nuclei from monomers is catalyzed by existing aggregates made up of the same sort of monomeric building components. Typically, this takes the form of monomers creating a nucleus on the surface of a previously formed aggregate where in the presence of a parent seed aggregate, secondary nucleation occurs.

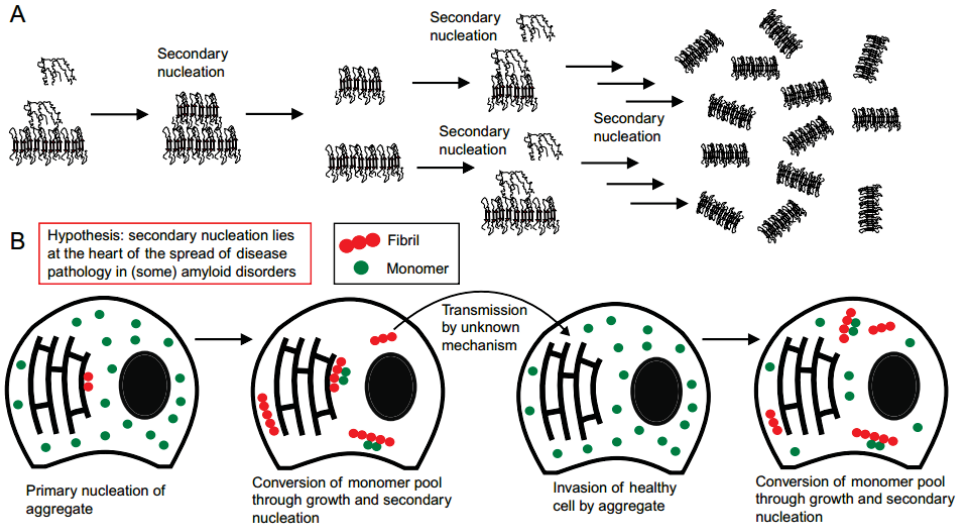

Figure **1-9**: Secondary nucleation's significance. a) Autocatalytic, exponential amplification of aggregate numbers can result from secondary nucleation. b) The spread of disease pathology in diseases like Parkinson's disease could be caused by the amplification of aggregates through secondary nucleation. Adapted with permission from [48].

Secondary nucleation differs from heterogeneous primary nucleation in that no foreign surface is involved and while the molecular mechanics of the two processes are similar, the resultant aggregation kinetics are substantially different. Since, filamentous structures grow only at their ends - a nucleation event on the filament's surface, followed by the separation of the newly created nucleus from the nucleation site, results in the rapid formation of a new filament. The auto-catalytic nature of this process is immediately apparent: the presence of filaments causes the formation of further filaments (see Fig. **1-9**).

The structural compatibility of the amyloid precursor protein appears to be critical for this nucleation mechanism. The presence of an autocatalytic secondary nucleation pathway is important because it allows for rapid amplification of small numbers of aggregates; indeed, a single seed filament introduced into a pool of metastable soluble protein can theoretically cause the entire pool to condense into filaments through repeated cycles of filament growth and secondary nucleation. This mechanism could be at the basis of disease pathology

(amyloid plaques, neurofibrillar tangles, and Lewy bodies) spreading across Alzheimer's and Parkinson's disease patients' brains, as well as other neurodegenerative diseases [234]. Several proteins, including amyloid-peptides, tau protein, α-synuclein, islet amyloid polypeptide (IAPP), insulin and bovine carbonic anhydrase are shown to possess secondary nucleation. The presence of pre-formed aggregates can also seed the formation of amyloid fibrils where the first nucleation event is negligible during this case, leading on to the expansion phase [294, 109, 280, 105].

Secondary nucleation is the dominant pathway of Aβ aggregation

Despite the fact that both mechanisms create aggregates from soluble peptides, monomer dependent secondary nucleation of Aβ(1-42) has a different thermodynamic signature. Specifically, although the rate constants for primary nucleation and fibril elongation both rise with increasing temperature, the rate constant for secondary nucleation has only a very weak temperature dependency and increases somewhat with decreasing temperature. While primary nucleation is a slow event with a high free energy barrier, secondary nucleation was found to be associated with a four-fold reduction in the free energy barrier relative to primary nucleation in the case of Aβ(1-42), demonstrating the remarkably effective way in which amyloid fibrils catalyze the nucleation of new aggregates from monomers in the case of AD [65].

The monomer-dependent secondary nucleation of the 42-residue amyloid-β peptide was identified as recently as this decade. Learning the fact that using master equations solved for the coupled differential equations describing primary nucleation and elongation or primary nucleation, elongation, and fragmentation, failed to reproduce experimental data on the concentration–dependent time course of amyloid fibril formation of Aβ(1-42) peptide was the first indication of the existence of such a process. While the findings might be recreated using a model that incorporates monomer nucleation on the surface of fibrils creation, this is simply a hint of the potential. Experimentally, one of the hypothesis that adding small amounts of prefabricated fibrils (seeds), so little that the sigmoidal-like shape of the development curve is preserved, would promote a shortening of the lag phase in a seed concentration-dependent way; was came out to be successful in the ThT-kinetics results. Finally, radio-isotope labeling was employed to track out the source of new tiny aggregates in the seeded process. Radioactive oligomers (3–20 mers) were found only when radioactive monomer was mixed with unlabelled seeds, but not in the case of unlabelled monomer mixed with radioactive seeds; indicating that the new aggregates are generated from monomer in a seed catalyzed reaction, rather than being breakdown products due to seed fragmentation. Secondary nucleation has been reported to saturate at high monomer concentrations in various circumstances. Aβ(1-40) was the first example of Aβ peptide in which the secondary nucleation saturation was detected and this phenomenon has subsequently been found for Aβ(1-42) in response to a shift in pH in human cerebrospinal fluid, for some disease-associated mutations and for designer mutants [207].

Furthermore, interactions between monomers and amyloid fibrils were discovered to not

only affect the rate constant that characterizes nucleation, but to fundamentally flip the thermodynamic signature of this process in comparison to primary nucleation. The energy barriers for both primary nucleation and fibril elongation were found to be enthalpic in character with a favorable activation entropy, indicating that the hydrophobic effect plays a prominent role in both processes. In contrast, for secondary nucleation, the enthalpic barrier is eliminated and the decreased free energy barrier has been demonstrated to be fully entropic in nature. These findings are analogous to surface catalyzed reactions involving an exothermic pre-binding step and they show that the catalytic efficiency of Aβ(1-42) fibril surfaces results from the enthalpic stabilisation of adsorbing peptides in nucleation-friendly conformations, resulting in a significant decrease in the activation energy barrier for nucleation.

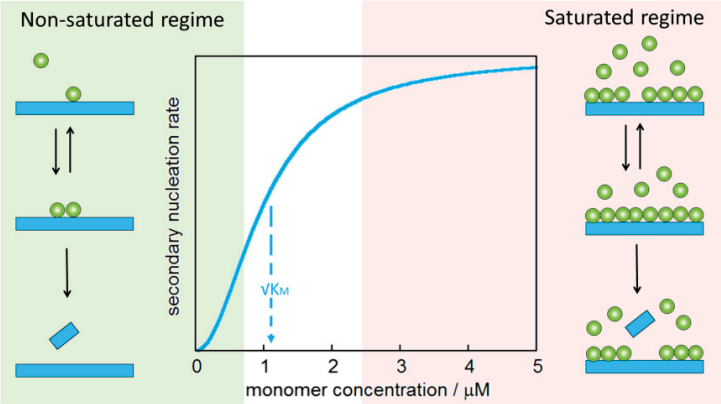

Figure **1-10**: Secondary nucleation is proved to be a multi-step process of which the dominant steps are: reversible monomer binding at the fibril surface and product (fibril) production. This is analogous to Michaelis–Menten kinetics in enzyme kinetics, which show an unsaturated regime with considerable rate dependency at lower monomer concentration (left) and a saturated regime with rate independence from monomer concentration at high monomer concentration (right) (right). The process is half-saturated at a monomer concentration of $\sqrt{K_M}$. Adapted with permission from [186].

The finding of saturation of the rate of secondary nucleation at high monomer concentration demonstrates the process's multi-step nature and Michaelis–Menten-like kinetics. Association of monomer with aggregates, nucleation on the surface and detachment are examples of composite stages. At high monomer concentrations, any of these stages may become rate-limiting depending on the ratio of monomer concentration to accessible surface area. The equivalent of a Michaelis constant is included in the kinetic modeling of saturated secondary nucleation, the square root of this parameter denotes the monomer concentration where the process is half-saturated. The process is unsaturated at low monomer concentrations and the reported total aggregation patterns are substantially dependent on monomer concentration. The process is saturated at high monomer concentrations and the reported overall aggregation patterns exhibit no reliance on monomer concentration [318, 186].

1.3 Molecular dynamics simulations

By integrating Newton's equations of motion, an molecular dynamics (MD) simulation may provide a dynamical trajectory for an N-particle system. We'll need a set of beginning circumstances (each particle's position and velocity), a suitable model to describe the forces operating between the particles (either based on electronic structure calculations or using the empirical force-fields provided in the later section) and boundary conditions. After that, we must solve the traditional equation of motion, which is:

$$m_i \frac{\partial^2 r_i}{\partial t^2} = f_i = -\frac{\partial}{\partial r_i} U(r_1, r_2, ..., r_N) \tag{1-1}$$

where $U(r_1, r_2, ..., r_N)$ is the potential energy depending on the coordinates of the N particles. This is a system of N connected second order non linear differential equations that can't be solved precisely. Equation (1-1) must be solved numerically using an appropriate integration procedure step by step. These are the most primary factors on which the solving of equation (1-1) depends:-

1.3.1 Initial conditions

Each particle's initial position and velocity in the system must be known. The positions of a crystal are normally given in the form of a crystallographic file, and we may construct a supercell by combining many unit cells. In a disordered system, positions can be produced at random or we can create an ordered structure and then melt it. The velocity of each particle is chosen at random from a Maxwellian distribution centered on the proper temperature, and the angular momentum and center of mass velocity of the entire system are then set to zero.

1.3.2 Boundary conditions

We must impose certain boundary limits since we are normally interested in the bulk properties of a liquid or solid system. Periodic boundary conditions must be used (PBC). As a result, the simulation box is encircled by an infinite number of clones. Only the N atoms inside the main cell are inspected in detail, but when one of them leaves, an image particle from the other side enters to take its place. We also need a model that can represent the interatomic forces that occur between the atoms that make up the system. Ideally, this could be done from the ground up by computing the forces on each atom after solving the electronic structure for a certain nuclei configuration. Since Car and Parrinello's pioneering work, the development of ab initio MD (AIMD) simulations has been steadily increasing, and today, the use of density functional theory (DFT) allows to treat systems of reasonable size (several hundreds of atoms) and achieve time scales of the order of hundreds of ps, making it the preferred solution to many problems of interest. The geographical and/or temporal scales necessary for such ab initio techniques, on the other hand, might be prohibitively expensive. In such cases, we must use empirical force field (FF)-based techniques with a higher degree of approximation. They make it possible to simulate systems with hundreds of thousands of atoms at nanosecond or even microsecond time-frames [196].

1.3.3 Force-fields

A force-field (FF) is a mathematical statement describing the link between a system's energy and its particle coordinates. It consists of a collection of parameters that enter into an analytical form of the inter-atomic potential energy, $U(r_1, r_2, ..., r_N)$. The parameters are often calculated using ab-initio or semi-empirical quantum mechanical calculations, or through fitted experimental data like electron, neutron and X-ray diffraction, infrared, NMR, Raman, and neutron spectroscopy, among other methods. Molecules are simply described as a group of atoms held together by basic elastic (harmonic) forces, and the FF substitutes a simplified model valid in the simulation region for the genuine potential. It should ideally be basic enough to be assessed fast while yet being comprehensive enough to mimic the system's attributes of interest. In the literature, there exist a variety of force fields with varying degrees of complexity and geared to tackle various types of systems. A common FF expression, on the other hand, would look like this:

$$U = \sum_{\text{bonds}} \frac{1}{2} k_b (r - r_0)^2 + \sum_{\text{angles}} \frac{1}{2} k_a (\theta - \theta_0)^2 + \sum_{\text{torsions}} \frac{V_n}{2} [1 + \cos(n\phi - \delta)]$$
$$+ \sum_{\text{improper}} V_{imp} + \sum_{\text{LJ}} 4\epsilon_{ij} \left(\frac{\sigma_{ij}^{12}}{r_{ij}^{12}} - \frac{\sigma_{ij}^{6}}{r_{ij}^{6}} \right) + \sum_{\text{elec}} \frac{q_i q_j}{r_{ij}},$$

Bonded energy terms include interactions such as bond stretching, valence angle bending, and dihedral rotation that occur between covalently linked atoms. The stiffness of the harmonic oscillations is defined by the force constants (k_b and k_a for bonds and angles, respectively), which can be derived from quantum mechanical (QM) vibrational analysis, spectroscopic data, and/or fitting to the potential energy profile as a function of the target bond perturbation or an angle away from its equilibrium value. The geometry at which the energy associated with the bond or angle is zero is defined by the equilibrium values (r_0 and θ_0 and for bonds and angles, respectively).

Dihedral rotation is frequently written as a cosine series, which reflects the periodic nature of rotations around covalent bonds, so that one or more energy minimums will exist during a 360-degree rotation period. Generally, the non-covalent bonding between atoms separated by three bonds, referred to as "1–4 pairs" cause rotation around a covalent bond. However, based on the force-field different representations for the dihedral potential have been reported in the literature. In classical force fields, dihedral terms are commonly used to account for inadequacies in the handling of nonbonded terms. The force constant ($V_n/2$), multiplicity (n), and phase angle (δ) are all needed parameters for dihedral energy expressions. The heights of the barriers between energy minima are determined by force constants. The multiplicity is the number of energy minima that span 360 degrees, and the phase angle is the offset that specifies where the energy minima are located. An energy minimum at 0° corresponds to a phase angle of 180°, while an energy minimum at 180° corresponds to a phase angle of 0°. Depending on the complexity of the potential energy surface, each rotatable bond may have many dihedral terms.

An "improper" dihedral is another energy phrase that is frequently used in the force-field terms which is associated with the out-of-plane deformation atoms around a planar center, for-example a carbon atom within an aromatic ring or a peptide bond. As contrast to "proper" dihedrals, the "improper" dihedrals are usually regarded as harmonic interactions, with the functional form:

$$U\left(\vec{R}\right) = \sum_{Impropers} k_{\varphi}(\varphi - \varphi_0)^2$$

where k_{φ} is denoting the force constant and φ_0 denoting the equilibrium improper dihedral, mostly 0°, corresponding to planarity. The bonded energy terms, taken together, explain the internal energy between covalently bound atoms as a function of bond lengths (b), valence angles (θ), dihedral angles (ϕ), and, in some cases, improper dihedral angles (φ). There are more complicated potentials for representing bound interactions, such as the Morse potential, which may mimic bond breakage, however this energy function is rarely used in protein simulations [302].

Finally, the most significant modification to the classic force-field potential equation is the explicit inclusion of polarization effects. As previously stated, the development of dipoles is induced by local electric fields developing in condensed phases and the partial charges employed to characterize a molecule in the liquid state, for example, will be insufficient to represent the same molecule in the gas phase. Alternatively, due to the varied electrostatic environments, the same amino-acid should have distinct charge distributions in different proteins. Furthermore, polarizability has an impact on ion's solvation energy in a non-polar environment, the directionality and energetics of H-bonds, interactions between cations and aromatic molecules, and so on. As a result, most current potentials explicitly contain polarization effects as well [329, 128, 63]. The three most principal methods to perform this modification includes:-

1. Fluctuating Charge Model: Charges are permitted to vary in response to their surroundings, allowing charge to flow between atoms until their instantaneous electronegativities are equal [258].

2. Shell Model (Drude particle): The atom is represented as the sum of a charged core and a charged shell, which are linked by a harmonic spring whose force constant is inversely proportional to the atomic polarizability. The electrostatic field formed by the surroundings determines the relative displacement of both charges [211].

3. Induced point dipoles: Each polarizable atom is connected with an induced point dipole μ_i, which is given by

$$\mu_i = \alpha_i({E_i}^q + {E_i}^{ind})$$

where α_i is the atom's isotropic polarizability, ${E_i}^q$ is the electrostatic field formed on the atom I by the permanent charges, and ${E_i}^{ind}$ is the field created by the rest of the atoms in

the system's induced dipoles. The polarization energy is given by:

$$U_{\text{pol}} = -\frac{1}{2}\sum \mu_i E_i$$

It's a big step forward to include polarization effects in the potential that describes intermolecular interactions. However, because both the static charges and the remaining induced dipoles impact the induced dipoles, they must be estimated in a self-consistent way by solving the preceding equations recursively until all of the induced dipoles' values converge. However, because a force field is a global entity, constructing new polarizable force fields necessitates reoptimizing the Van der Waals and intramolecular parameters as well. Because this is such a large effort, existing polarizable force fields are still in their infancy which might account for the inconclusive findings found when comparing the capabilities of polarizable and nonpolarizable materials. Nonetheless, recently on biological systems, they show a higher agreement with experiment than non-additive force fields and a detailed physical description of intermolecular interactions; which may lead to increasing their transferability globally [13, 154, 298].

With the advent of the molecular mechanics (MM) approach in the 1960s, the first force fields developed, with the primary purpose of predicting molecular structures, vibrational spectra, and enthalpies of isolated molecules. The earliest of these force fields was developed to investigate hydrocarbons, but they were eventually expanded to include a wide range of organic and functionalized compounds (alcohols, ethers, sulphides, amides etc.). The MM potentials created by Allinger's group are the greatest example of such force-fields: MM2, MM3 and MM4 [113, 21, 23, 22]. More universally applicable force fields such as the Dreiding and Universal (UFF) force fields, which contain parameters for all atoms in the periodic table are good examples besides the most popular force-fields like CHARMM, AMBER, GROMOS, OPLS and COMPASS. Many of these force fields are constantly evolving through parameterization and validating towards experimental results and different versions are available nowadays (for example, CHARMM19, CHARMM22, CHARMM27, CHARMM36, CHARMM36m, GROMOS96, GROMOS45A3, GROMOS53A5, GROMOS53A6, AMBER91, AMBER94, AMBER96, AMBER99, AMBER02 etc.) [203, 255, 15, 18, 225, 199, 19, 1]. The first general polarizable force fields occurred in the 1990s. Such advances include the PIPF (polarizable intermolecular potential function), DRF90, and AMOEBA force fields. Polarization has been added to the CHARMM force-field using either fluctuating charges or the shell model, and polarization has also been added to AMBER, OPLS, and GROMOS force-fields [112, 306, 16, 231, 181, 328, 157, 114]. Water deserves special attention in this regard, as a significant number of water models have been presented since Barker and Watts offered the first MC simulation. Vega et al. recently compared the most prominent rigid non-polarizable water potentials (TIP3P, TIP4P, TIP5P, SPC, and SPC/E) and discovered that a modified version of the second, dubbed TIP4P/2005, offers the best representation of the experimental features evaluated [123, 34, 319]. Comparing the performance of current general force fields is considerably more challenging since the outcome is highly dependent on the system and features simulated. There are several comparisons in the literature, particularly on the accuracy of the CHARMM, AMBER, and OPLS force fields in biomolecular simulations but the results are not conclusive. As a result, Price and Brooks discovered

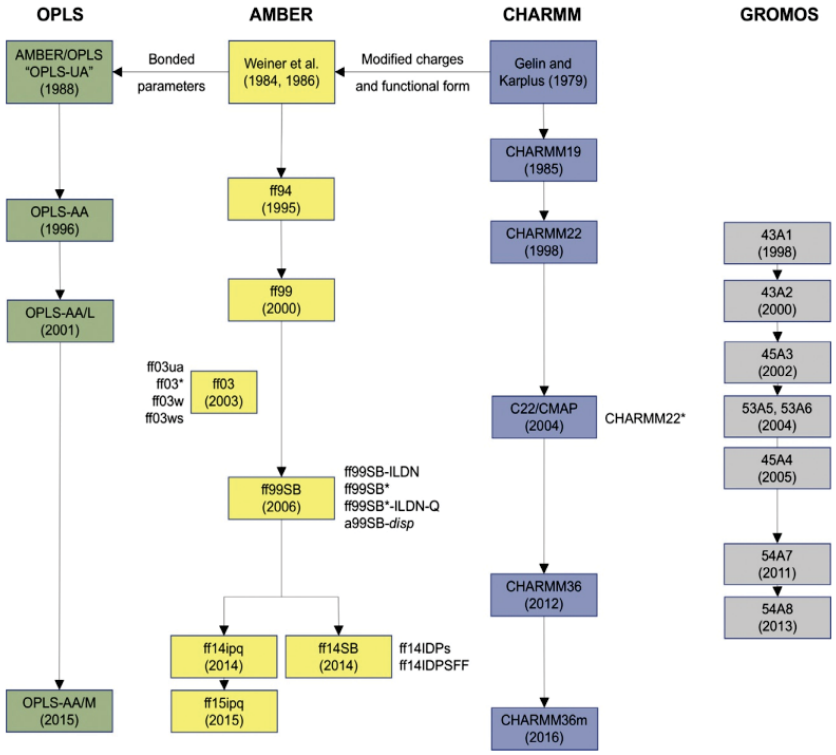

Figure **1-11**: The AMBER, CHARMM, OPLS, and GROMOS atomistic force fields have a long history of development. Major re-parametrization efforts are shown in the vertical progression, and important parameter sets are boxed. Along with the parameter set from which they were formed, additional force fields emerge. The parameters transfers or discrepancies between the CHARMM, AMBER, and OPLS force fields demonstrate their similar origins. Adapted with permission from [301]

that the three produced very identical outcomes in terms of protein structure and kinetics. Yeh and Hummer, on the other hand, discovered substantial changes in the structures of two peptides investigated using CHARMM and AMBER, as well as the end-to-end diffusion coefficient. Aliev and Courtier-Murias discovered that the structure of short open chain peptides is strongly influenced by the force field utilized. In simulations of insulin using CHARMM, AMBER, OPLS, and GROMOS, a similar effect was discovered, with various structural trends favoring different force fields. Paton and Goodman conducted one of the most thorough assessments of existing potentials. They used seven different force fields (MM2, MM3, AMBER, OPLS, OPLSAA, MMFF94, and MMFF94s) to evaluate the interaction energies of 22 molecular complexes of small and medium size, as well as 143 nuclear acid bases and amino acids, and compared them to the energies obtained from high-level ab initio calculations. Their findings demonstrate that all of the potentials studied, particularly OPLSAA and MMFF94s, properly characterize electrostatic and van der Waals interactions, but that hydrogen bonding interactions are drastically overestimated. The major conclusion is that each force field has unique strengths and weaknesses based on the data and process used in its parametrization, hence the ultimate decision is based on the specific situation at hand [240, 350, 20, 311, 232, 158].

1.3.4 Force-fields for IDPs

Many force fields have also been adjusted for simulation studies of IDPs, with two main reasons for doing so. The first step is to tweak force field settings, which may result in global optimization, which implies that the performance of both folded and non-folded protein (IDP) simulations may be enhanced. The second step is to modify secondary structure propensities such that unfolded secondary structures, which are common in IDPs, may be seen. In certain circumstances, these reparametrization operations just retrain an existing base force field. The majority of training data is taken from experimental and/or quantum mechanical data. Different training sets will almost probably result in force fields with varying applicability.

Adjusting dihedral parameters

Backbone dihedrals (ϕ and ψ) and side-chain dihedrals (χ_1 and χ_2) are the two types of dihedral angles, commonly taken into account in the force-field paramters for MD simulation methods. Refinement of the backbone dihedral parameters is becoming more typical in current IDPs specific force-fields. The most prevalent difficulty in simulations of IDPs for numerous protein force fields is overestimating populations of secondary structures, such as α-helix and β-sheet, which are frequently disordered in IDPs and many protein force fields indeed resulted in uniform overestimation. One solution to this problem is thought to be including the dihedral data from the coil fragments in the training sets used to develop force-fields. This method has been employed for IDPs specific force-fields in ff03* and ff99SB*, which are based on the ff0318 and ff99SB, respectively. The helix-coil parameters in both the force-fields are calculated using Lifson-Roig helix-coil theory. These two force fields are compatible with NMR investigations on folded proteins and short peptides. However, the helical contents of ff03* are exaggerated in comparison to ff03, whilst the helical contents of ff99SB* are underestimated in comparison to ff99SB. It should be noted that both ff03* and ff99SB* were created in the context of the TIP3P water [325, 78, 345, 273, 256, 9].

This method was also used to construct two new OPLS protein force fields (OPLS-AA/M and OPLS3), where both of them require reparameterization of the backbone dihedral and side-chain dihedral with regard to a training set of ab-initio torsional energy scanning data of blocked di-peptides. In protein-ligand binding simulations, the OPLS3 force field performed well. While in the CHARMM force-fields family, the CHARMM22* is also the outcome of refitting the original CHARMM22 force-field using a similar technique; which is primarily concerned with the folding and unfolding transitions of the peptide. CHARMM22* had the best agreement with both the kinetic and thermodynamic parameters of experimental data during a 100 μS simulation of the villin headpiece (PDB ID: 2F4K) [90, 270, 10].

In addition to direct refitting of universal dihedral parameters, residue-specific dihedral parameters can be used to increase agreement with experimental observables. Wu and colleagues used this method to create the RSFF1 and RSFF2 force-fields. As the training set, both efforts used rotamer distributions from a protein coil library. It should be noted that the RSFF1 is developed from OPLS/AA, whilst the RSFF2 is derived from ff99SB, yet

both followed similar procedures. Both RSFF1 and RSFF2 force-field were shown to be successfully towards analyzing the secondary structures adopted by Trp-cage, Homeodomain, Trpzip-2 and GB1 hairpin [99, 75, 110].

Adding CMAP parameters

CMAP stands for grid-based energy correction map, which is based on a two-dimensional distribution of backbone dihedrals. A sample bin size of 15° is used to split both backbone dihedrals equally which would result in a total of 576 bins per residue spanning the two-dimensional dihedral space. For each bin, the conformational free energy is represented as:

$$\Delta G_i = -RTln\frac{N_i}{N_{max}}$$

where N_i is the number of dihedral data in bin i and N_{max} denotes the total number of dihedral data in the sample. The conformational free energy of each residue may therefore be calculated using both a database ($\Delta {G_i}^{\mathrm{DB}}$) and a force field simulation ($\Delta {G_i}^{\mathrm{MM}}$) and the CMAP correction value can be expressed as:

$${E_i}^{\mathrm{CMAP}} = \Delta {G_i}^{\mathrm{DB}} - \Delta {G_i}^{\mathrm{MM}}$$

A bicubic interpolation approach is then used to produce a continuous and smooth energy correction surface from which the energy correction value for each conformation can be computed. Originally, the CMAP approach was employed in CHARMM22/CMAP force-field (also known as CHARMM27), which was built on CHARMM22. Although CHARMM27 force-field overestimates the helical conformation when modeling α-synuclein and can't construct a stable hairpin structure, but it was found to be balancing between the helix and coil conformations. Based on experimental NMR data, a later force-field CHARMM36 has been found to be increasing the CMAP potential. However, when modelling certain IDPs using CHARMM36, left-handed helices were found be overpopulated. This constraint was later overcome by the development of CHARMM36m force-field. C_α atoms in CHARMM36m force-field are separated into three groups based on the kind of residue: CT2 for glycine, CP1 for proline and CT1 for the remaining 18 amino acids, which is equivalent to using a minimum residue-specific CMAP method. Because of its training set comprises folded proteins as well as IDPs, CHARMM36m force-field proved to be a balanced force field for both IDPs and folded proteins. Another force field, a99SB-disp, is based on moderate refinement of the torsional and non-bond parameters using a similar technique to CHARMM36m and based on the ff99SBildn force-fields along with TIP4P-D water models. This force field also attempts to strike a balance between IDPs and folded protein; however, while modelling the aggregation of Aβ(16-22) and Aβ(1-40) peptides, issues arose due to inaccuracy in the population of the β-hairpin conformations [10, 185, 11, 267, 142, 137, 228, 189, 233].

The CMAP potential is only adjusted for eight disorder-promoting amino acids (G, A, S, P, R, Q, E, and K) in early residue-specific CMAP force fields for IDPs, namely, ff99IDPs (derived from ff99SBildn) and ff14IDPs (produced from ff14SB). The usage of CMAP potential is expanded to all 20 standard amino acids in future development of CMAP-based

force fields, ff14IDPSFF and CHARMM36IDPSFF. These were created by combining ff14SB with CHARMM36m. It was discovered that ff14IDPSFF works exceptionally well in long-time simulations (i.e., microsecond time scales) and accurately reproduces NMR observables. The CHARMM36IDPSFF force field also performs well in multiple-trajectory and replica-exchange simulations. A recent analysis of several IDP force fields shows that IDP-specific force fields increase the agreement of simulated observables with experiment in general. CHARMM22* performs better than CHARMM36m for many observables, while it still favors helicity in simulations of short peptides [326, 78, 124, 125, 323, 216].

A residue-specific OPLS force field, OPLSIDPSFF, using a similar CMAP method was also developed to correct backbone torsion terms for all 20 standard residues. The OPLSIDPSFF was created from OPLS-AA/L and was designed to mix with TIP4P-D water. When paired with the TIP4P-D water model, the OPLSIDPSFF force field can recreate the majority of experimental data for the tested proteins, particularly NMR chemical shifts and scalar couplings [345, 168].

Both folded and disordered conformations should be well recreated with a given force field when simulating biological molecules having folded and disordered regions, ff03CMAP force-field is one such model. This is due to the fact that it was created using a different training set that included not just IDPs but also folded proteins which highlights the importance of selecting training models. TIP4P-Ew62 and TIP4P-D63 water models might be utilized in combination with the ff03CMAP force field for investigating the conformations of both IDPs and folded proteins, where the ff03CMAP/TIP4P-Ew combination found to be particularly well suited for folded protein simulation, whereas the ff03CMAP/TIP4P-D combination found to be highly suited for IDPs simulation. Based on RSFF2 force-field, Wu and his colleagues developed RSFF2C force-field, a three-dimensional-CMAP force field with correction not only in the backbone dihedrals (ϕ and ψ), but also in the side-chain dihedral (χ_1). The RSFF2C force field was found to be enhancing the backbone dihedral sampling for both folded proteins and IDPs, as well as ab-initio folding of certain fast-folding proteins [140, 269, 324].

The ESFF1 force field was developed by extending the residue-specific CMAP correction to take into account each residue's sequence context. A residue's sequence environment was classed as polar if its neighbor is Gly, Ser, Tyr, Cys, Asn, Gln, Thr, His, Glu, Asp, Arg or Lys; while if its neighbors are Met, Trp, Phe, Val, Leu, Ile, Pro and Ala, then it's sequence environment is classed as non-polar. Following that, for each of the 20 residues, four (polar/non-polar-X-polar/non-polar) sequence contexts arose. Extensive simulation findings demonstrated that ESFF1 force-field can accurately duplicate the NMR measurements of 61 short peptides and IDPs. Through using 71 well-trained environmental CMAP parameters, the ESFF1 also established a suitable balance between folded and disordered proteins [346, 77].

Refining protein–water interactions

Because IDPs lack substantial hydrophobic cores with numerous buried nonpolar residues, the interaction between protein and water was is found to be critical in MD simulations. Non-bond interactions between proteins and water can be classified as either electrostatic or van der Waals, as indicated by atomic partial charges and L-J parameters. The protein-water van der Waals interaction was discovered to often alter the size of simulated IDPs as assessed by the radius of gyration, Rg. Many early IDPs force fields which were trained using NMR data are found to be incapable of producing IDPs that are long enough to be consistent in terms of Rg parameter, as demonstrated in experiments. This problem was effectively solved in several subsequent generations of IDP force fields through adjusting the L-J potential energy (also known as 12-6 potential) parameter, which is defined as:

$$V_{ij,\text{L-J}} = 4\varepsilon_{ij}\left[\left(\frac{\sigma_{ij}}{r_{ij}}\right)^{12} - \left(\frac{\sigma_{ij}}{r_{ij}}\right)^{6}\right]$$

The CHARMM36m and a99SB-disp force fields, are such examples of IDPs specific force-fields which besides the CMAP correction, also contain the adjustment of the protein-water L-J potential parameters. The TIP4P-D water model with a higher oxygen value was presented to be suitable for conformational analysis of IDPs while this water model does improve the Rg values of certain simulated IDPs, but it also lead some α-helix to unfold and overestimates the Rg of other longer IDPs. This water model was used in the creation of ff03ws force-field, based on ff03w force-field. In some ways, this force field eliminated another major issue that existed among earlier IDPs force fields: over-stability of the protein-protein interaction, which frequently effects IDPs aggregation behaviors. On the other hand, a force field known as a99SB-UCB68, which also modifies the non-bonded and backbone parameters, may be able to overcome this problem [143, 228, 269, 241].

The CHARMM36m modifies both the oxygen and hydrogen atoms in water to increase its performance in IDPs simulations, however, an alternative version of CHARMM36m force-field in combination with a increased L-J well depth parameter for the H-atoms only of the original TIP3P water model, while maintaining the oxygen L-J parameters and the water–water interactions intact; was proposed to be a more effective force-field towards an efficient sampling of short IDPs in terms of good agreement of Rg values for CspTm peptide with the observed experimental values. However, this alternative CHARMM36m force-field model is yet to be tested for conformational analysis of well-tested IDPs like full length Aβ peptide where the AMBER99SB*ILDN, ff99SB-disp, CHARMM22* and CHARMM36m (both original and with modified protein-water interaction - but only with Aβ40 and Aβ(16-22) fragment) force-field models in combination of either original TIP3P or TIP4P-D water mode already showed acceptable results comparing in terms of experimental parameters [257, 189, 233, 271].

The implicit solvent model, in addition to the explicit solvent model, is another method

proved efficient for IDPs modeling. In contrast to the explicit solvent models, the implicit solvent models depict the impact of solvent using extra potentials rather than real water molecules. The general free energy of solvation is commonly separated into three components:

$$\Delta G_{\mathrm{sol}} = \Delta G_{\mathrm{cav}} + \Delta G_{\mathrm{vdW}} + \Delta G_{\mathrm{ele}}$$

SASA approaches methods model either the non-polar terms $\Delta G_{\mathrm{cav}}+\Delta G_{\mathrm{vdW}}$ or the full ΔG_{sol} component, whereas Poisson-Boltzmann and Generalized-Born methods represent the ΔG_{ele} term. Implicit water models are employed in large-scale screening and large-system simulation because they need fewer computer resources, which is critical for IDPs investigations [85, 29].

1.3.5 Enhanced sampling methods in molecular dynamics simulations

In contrast to folded proteins, modelling equilibrium structures or investigating the mechanisms of interactions and aggregations of IDPs necessitates large-scale sampling. IDPs require improved sampling methods to reduce the cost of computing resources.There are three kinds of ideas. The first is to bypass the energy barrier by employing extra potential energy terms, such as metadynamics and umbrella sampling. The former adds potential energy based on the collective variables (CVs) selected, whereas the latter adds potential energy in an elastic form. The second concept is to swap copies from parallel paths, which may be accomplished by temperature replica exchange molecular dynamics (T-REMD), temperature cool walking (TCW) and bias exchange metadynamics (BEMD) [304, 264, 268]. The T-REMD is based on MD simulation, whereas the TCW and BEMD are based on Monte Carlo simulation and metadynamics, respectively. The T-REMD, sometimes known as the REMD, is the most widely used enhanced sampling method. The last concept is to use both principle component analysis (PCA) and a type of edge searching approach to locate "edge structures" on the energy surface and then run seed MDs depending on the structures found. By repeating this approach indefinitely, the sample locations will progressively escape from the original potential energy trap. This kind includes structural dissimilarity sampling (SDS), parallel cascade selection MD (PaCS-MD), self avoiding conformational sampling (SACS), complementary coordinates MD (CoCo-MD) and frontier expansion sampling (FES). The main difference between both approaches is the methodology utilized to determine the frontier structures, which in the FES method is the convex hull algorithm [246, 242, 243, 245, 244, 247, 8, 146].

Replica exchange molecular dynamics (REMD)

To improve conformational exploration, replica exchange molecular dynamics (REMD) which is also known as parallel tempering (PT) was created [304]. Several separate clones of the target system are created in REMD, which are referred to as replicas, are simulated in parallel at various temperatures. Exchanges of temperatures or configurations of neighbored replicas are attempted at regular time intervals. When the Metropolis criteria is met, an exchange between copies i and j is accepted as:

$$P(q_i \leftrightarrow q_j) = \min\left(1, \exp\left[\left(\frac{1}{k_B T_j} - \frac{1}{k_B T_i}\right)[H(q_j) - H(q_i)]\right]\right)$$

where $H(q_i)$ and $H(q_j)$ are the potential energies of replicas i and j, and T_i and T_j are the temperatures of replicas i and j respectively; and random walks of the temperature ladder replicas are produced with each replica experiencing both high and low temperatures.

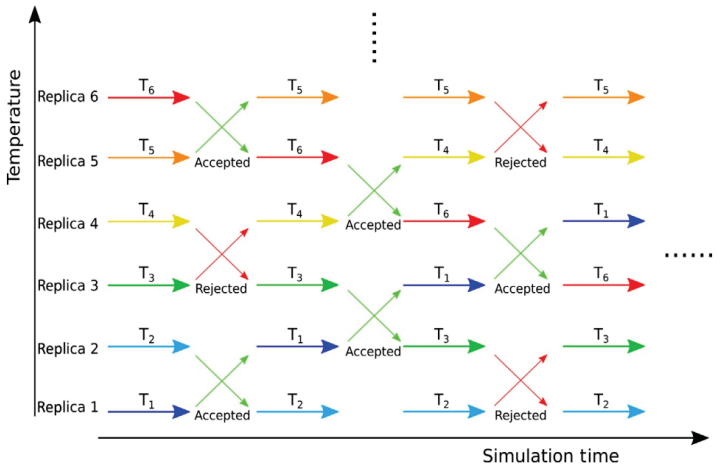

Figure **1-12**: The replica exchange molecular dynamics methodology is depicted in this diagram. REMD runs a series of MD simulations termed replicas (six of which are shown) in parallel at varying temperatures. Temperatures or coordinates at regular intervals a set of neighboring duplicates are swapped with a chance that meets the Metropolis criterion. Adapted with permission from [301].

The sampling of the conformational space is therefore improved by transferring configurations that are only accessible at high temperatures to replicas at lower temperatures, allowing precise thermodynamics information or free energy landscapes to be derived. The fundamental difficulty with temperature REMD (T-REMD) is that the number of replicas rises dramatically as the simulated systems grow in size, making it computationally expensive for complex biological systems. The replicas in T-REMD differ in the temperature at which the MD simulations are run. However, the discrepancies between the copies do not stop there. Any control parameter can be altered; for example, the Hamiltonian of the simulated system can be altered for each copy [343, 344]. In a broader sense, each replica is simulated at a different Hamiltonian and temperature (HT-REMD); the acceptance criterion is therefore given as:

$$P(q_i \leftrightarrow q_j) = \min\left[1, \exp\left(\frac{H_i(q_i) - H_i(q_j)}{k_B T_i} + \frac{H_j(q_j) - H_j(q_i)}{k_B T_j}\right)\right]$$

To solve T-REMD difficulties and improve sampling efficiency, many methods for altering the Hamiltonian in replica exchange simulations have been proposed. Among these, solute tempering for simulations of solvated systems was a brilliant innovation. Solute–solute and solute–solvent interactions are scaled by various scaling factors in different replicas in replica exchange with solute scaling (REST), but solvent–solvent interactions are left intact. Thus, a minimal number of copies are necessary to generate excellent exchange probabilities, which require significant overlap in the energy contributions of the replicas to be swapped. This approach was refined further in REST2, in which all replicas are simulated at the same temperature, and conformational sampling is boosted by scaling of the solute's intramolecular potential energy. REST2 demonstrated much reduced computational cost and sampling efficiency when compared to T-REMD. Later, Bussi created Hamiltonian replica exchange molecular dynamics (commonly known as REST2 or HREX), a new form of REST2 with better scaling and greater flexibility in terms of which elements of the system the scaling is applied to [56, 182, 327]. For exchange efforts between two copies i and j, the Metropolis criteria of HREX is:

$$P(q_i \leftrightarrow q_j) = \min\left[1, \exp\left(\frac{H_i(q_i) - H_i(q_j)}{k_B T} + \frac{H_j(q_j) - H_j(q_i)}{k_B T}\right)\right]$$

All replicas in HREX are simulated at the same temperature, and the Hamiltonian of the solute is scaled by different scaling factors at different replicas, but the solvent–solvent interactions are not altered. With HREX, one may restrict the scaling to a certain area of the simulated system that is thought to be interesting. Because REMD improves unconstrained sampling, this approach and its derivatives are commonly used to solve issues when defining a CV, particularly previous sampling, is difficult or perhaps impossible. Such issues include the sampling and aggregation of peptides, protein–protein recognition processes, and the identification of ligand binding sites and poses, which might be important for ligand identification in computational drug development [250, 251, 73, 165, 214, 163].

Umbrella sampling

Torrie and Valleau invented umbrella sampling (US) method of MD simulation in 1977 [118] which is one of the most often utilized methods for overcoming free energy obstacles in free energy calculations. As demonstrated, umbrella sampling models a conformational shift by using a succession of independent windows along a chosen CV. A simple harmonic potential $V_i(q)$ is added to the system's Hamiltonian for each of the windows, with its strength determined by the force constant k and selected based on the potential energy at each of the reference points s_i along the CV *s(q)*:

$$\Delta V_i(q) = \frac{k}{2} \times (s(q) - s_i)^2$$

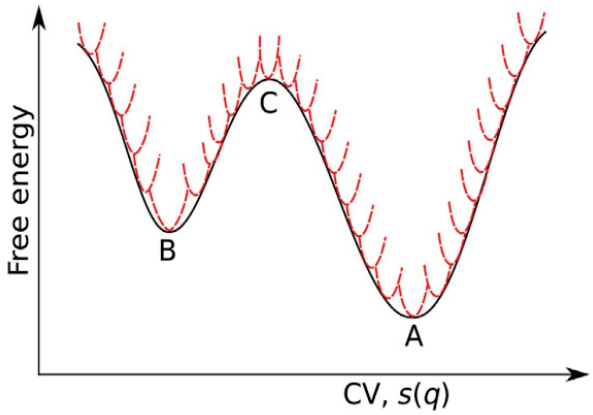

Figure **1-13**: The umbrella sampling method is depicted in this diagram. The harmonic bias potentials that are added to the system Hamiltonian at distinct CV positions (windows) along the CV space are represented by the red dashed lines. Adapted with permission from [301].

MD simulations are then run for all windows. When these simulations are completed, the most preferred approach for combining the statistics from all of the individual windows is WHAM analysis [177] and the corresponding equations are written as follows:

$$P_u(s) = \frac{\sum_{l=1}^{N} h_l(s)}{\sum_{k=1}^{N} n_k \exp\left([F_k - V(s)]/k_B T\right)}$$
$$F_k = -k_B T \ln \sum_{q} P_u(s) \exp\left(-V(s)/k_B T\right)$$

where $P_u(s)$ is the unbiased probability distribution along s, N is the number of umbrella windows, l and k are indexes of the umbrella windows, $h_l(s)$ is the counts at bin s, n_k is the number of data points from window k and F_k is the factor to be determined for window k. Because of its quick convergence and the fact that the MD simulations for the different windows can be run independently of each other, allowing for the addition of additional windows to the system to improve convergence, umbrella sampling has been demonstrated to be a great success by a large number of studies that used umbrella sampling in a wide range of biological systems including protein folding, conformational changes of large proteins, protein–protein interactions, protein–loop interactions and protein–loop interactions [126, 149, 215].

1.4 Surface-based bio-sensing techniques for investigating the aggregation process in amyloid-beta peptide

Surface-based bio-sensing experiments during which seed fibrils are attached to the surface of a biosensor allow only processes near the surface to be detected, are another important class of protein aggregation measurement techniques that are particularly well adapted for studying the expansion of pre-formed fibrils. The event of the surface-bound fibrils within the presence of protein solutions may then be tracked. Under optimal circumstances the sensor surface only has got to be incubated with protein monomer solutions for some minutes, a duration during which no appreciable nucleation of latest fibrils occurs in most situations. Applications of surface-based biosensing methods for the study of amyloid fibril growth was initially based totally on surface plasmon resonance (SPR, detection supported change in refractive index), but later, quartz microbalance (QCM, detection supported change in hydrodynamic mass) devices were demonstrated to permit for the convenient and detailed study of amyloid fibril growth. Surface-based biosensing approaches (SPR and QCM) are demonstrated to be capable bulk solution techniques like dynamic light scattering (DLS) and ThT fluorescence, a minimum of in terms of the relative impacts of changes in salt content on fibril elongation rate.

1.4.1 Quartz crystal microbalance (QCM)

The quartz crystal microbalance (QCM) is a surface-based nanogram sensitive technique that utilizes a piezoelectric, single crystal quartz plate to generate acoustic waves by oscillating for measuring surface-adsorbed mass [179]. The QCM principal is based on the inherent piezoelectric property of the quartz crystal, whereby the quartz is sandwiched between two gold electrodes where the application of a rapidly oscillating AC field, induce the alternating expansion and contraction of the quartz crystal lattice which stimulates it to vibrate at its resonant frequency. Resonance is occurred upon sufficient application of AC voltage matching the frequency close to the resonant frequency (f_0) of the particular crystal; specifically when the standing wave generated from the alternating expansion and contraction of the quartz crystal is an odd integer of the thickness of the quartz disc. Typically, the resonant frequencies of commercial QCMs attains the order of MHz and the trade-off between the frequency (related to sensitivity of the instrument) and the thickness (related to the usability) of QCMs is that thinner the quartz crystal, the higher the resonant frequency occurs. Commonly in commercialised QCMs have the resonant frequency (f_0) of 5 MHz, corresponding to the thickness ca. 330 μm of the quartz disc. QCM methods became widely used as mass-balances upon the demonstration of Sauerbrey equation in 1959 [279] relating to the surface-adsorbed mass (Δm) with the change in frequency (Δf) of the oscillating quartz crystal, mathematically the relationship is written as -

$$\Delta m = \frac{C}{n}\Delta f$$

where n is the harmonic number and

$$C = \frac{t_q \rho_q}{f_0}$$

where t_q being the thickness of quartz, and ρ_q being the density of quartz and equals ca. –17.7 Hz ng/cm^2 for a 5-MHz crystal. Although, we need to remember that the Sauerbrey equation was established upon three major assumptions -

i. the adsorbed mass must be small relative to the mass of the quartz crystal.
ii. the mass adsorbed is rigidly adsorbed.
iii. the mass adsorbed is evenly distributed over the active area of the crystal.

For theses assumption to remain valid, the QCM methods based on this equation was exclusively used for measurements in vacuum or gas-phase only, taking advantage of the sub-monolayer sensitivity of QCM.

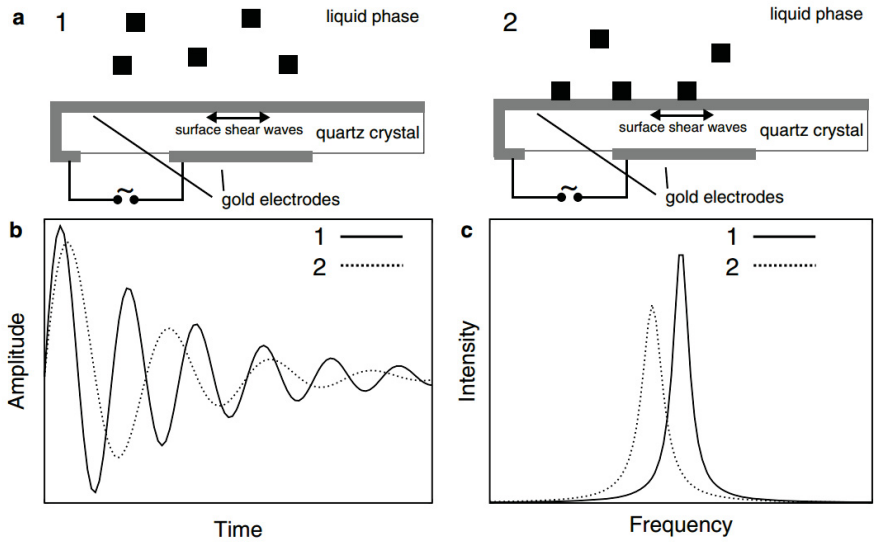

Figure **1-14**: The working principle of a liquid QCM. (a) Shear waves in the quartz crystal are excited by applying a fast oscillating AC voltage across a piezoelectric quartz disc. An rise in mass indicates the attachment of molecules from the solution phase. (b) The frequency and exponential decay constant of the vibration of a quartz crystal submerged in liquid are defined. The sensor surface and the liquid have a high connection, which causes the deterioration. Additional mass attachment reduces resonance frequency and accelerates exponential decay if the coupling of the surface to the liquid is increased. (c) Frequency spectra of the time domain record, shown schematically (b). The drop in resonant frequency and rise in full width at half maximum are both recorded and constitute data that may be used to assess the amount and structure of the connected material. Adapted with permission from [53].

The applications of QCM method in liquid-environments dramatically increased later in biotechnology applications, particularly in bio-sensors due to sensitivity and robustness of the method. But, applications of QCM technology in liquid medium violated one of the basic assumptions of Sauerbrey equation i.e. the mass adsorbed should bind rigidly, since in most of applications in liquid medium incorporated viscous and elastic contributions to the frequency change (Δf); which showed the requirements for characterizing the frictional

dissipative losses occurring with the adsorbed mass due to their visco-elastic character and the theory for interpreting this new data sets in liquid phase.

Main approaches towards monitoring dissipation (D) due to visco-elastic effect during the mass adsorption in liquid-phase have been either monitoring the decay of a crystal's oscillation after a rapid excitation close to the resonant frequency (since the decay rate is proportional to the energy dissipation of the oscillator) or impedance analysis; the former being the most commonly used approach in the commercialized QCM instrument since the QCM with dissipation monitoring (QCM-D) fits the voltage of oscillatory decay after a driving power is switched off in such a way as to ensure that the quartz decays close to the series resonant mode. The amplitude decays over time depending on the properties of the oscillator and the contact medium [191, 4, 190]. The decay voltage, i.e., the output voltage amplitude in terms of time function, along with the resonant frequency of the quartz crystal (f_0), is mixed with a reference frequency (f_R) and filtered with a low pass band filter. This gives an output frequency (f) equivalent to the difference between f_R and f_0. This output frequency is fitted to an exponentially damped sinusoidal, $A(t)$, according to:

$$A(t) = A_0 e^{t/\tau} sin(2\pi f t + \alpha)$$

where f = f_0 - f_R. The dimensionless dissipation parameter is given by:

$$D = \frac{1}{\pi f \tau} = \frac{1}{Q} = \frac{E_{Dissipated}}{2\pi E_{Stored}}$$

with Q being the quality factor, $E_{Dissipation}$ being the energy dissipated during one oscillatory cycle and E_{Stored} denotes the energy stored within the oscillating system.

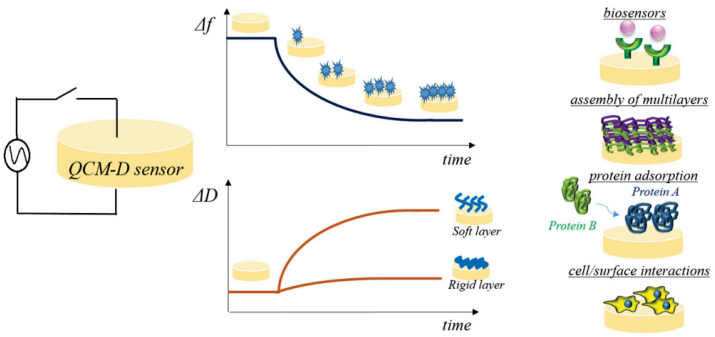

Figure **1-15**: Model Sensogram of QCM depicting Δf and ΔD with respect to time along with the possible application areas. Adapted with permission from [313].

The QCM-D approach allows for probing f and D values at multiple harmonics (n = 3, 5, . . .) of a resonant frequency in succession on the millisecond time scale. The multiple harmonic data allows for the extraction of significant characteristics like as mass, thickness, density, viscosity, and storage modulus by modeling the experimental data with theory. The visco-elastic data allows broader characterization of systems falling outside the scope of the linear Sauerbrey relationship between Δf and Δm and makes QCM-D more than a simple mass balance. Additionally, associated solvent or water content of adsorbed films can be

measured through comparing the measured mass using QCM-D with that of complementary techniques such as surface plasmon resonance or ellipsometry.

Amyloid formation consists of several sub-processes out of which three main processes are - the generation of seeds (nucleation), the growth of those seeds to form fibrils (elongation), and finally secondary nucleation processes (such as fibril fragmentation) which increase the number of fibrils depending on the number of existing fibrils [173]. The elongation step can be investigated separately using the bio-sensing approach of QCM although this technique can also be used to study the entire process of amyloid fibril formation [46, 135, 174]; we will particularly focus towards monitoring amyloid fibril elongation using this surface-based bio-sensing technique. The fact that the formation of a continuous ensemble of seed fibrils may be probed repeatedly is the distinctive strength of these surface-bound kinetic methods, of which QCM is a notable exemplar. As a result, the growth rates of the identical seeds incubated with different monomer solutions or under different circumstances may be compared directly.

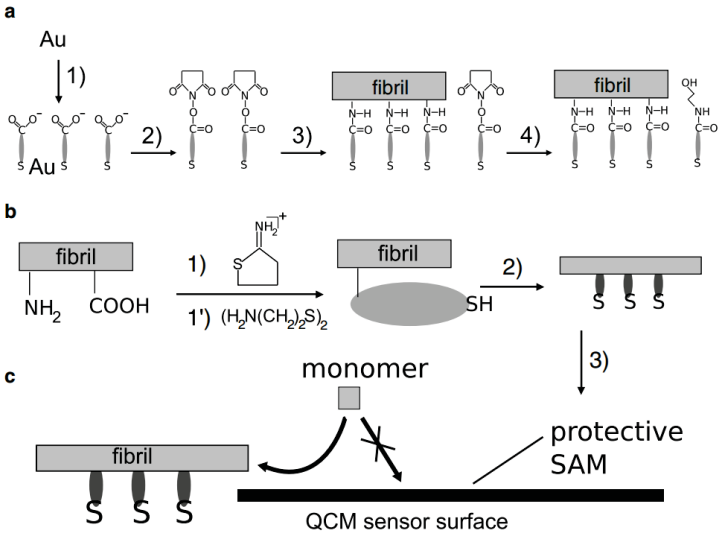

Figure **1-16**: Schematic illustration of the seed fibril attachment to a gold-coated QCM sensor. (a) Attachment of seed fibrils to a chemically activated SAM: (1) formation of SAM of mercaptoundecanoic acid (MUA), (2) activation of SAM with EDC and NHS to form reactive NHS esters, (3) coupling of the seed fibrils to the acti- vated SAM, (4) passivation of the remaining activated MUA with ethanolamine; (b) attachment of chemically modifi ed amyloid fi brils to a gold surface: cou- pling of Traut's reagent (1) or cystamine (1¢) to the seed fibrils, (2) attachment of modified seeds to the gold surface, (3) passivation of the remaining exposed gold surface with an SAM; (c) QCM measurement where the surface-bound seeds are exposed to a solution of soluble amyloidogenic protein. The non- specific attachment of protein onto the surface is prevented by the SAM, and the attachment primarily directed onto the seeds. Adapted with permission from [53].

Attachment of amyloid fibrils on the QCM sensor surface

As described in the Fig. **1-16**, two main protocols are followed to attach the amyloid fibrils on the QCM sensor surface coated with the gold layer i.e. Self-Assembled Monolayer (SAM) & Activation of Fibrils. In the SAM method, a layer of activated acid groups, in particular mercaptoundecanoic acid (MUA) is used to form a SAM over the gold coated surface of QCM sensor and then coupling between the SAM and side chain -NH2 groups of the fibril from the desired peptide is done using EDC/NHS chemistry; and subsequently the surface is passivated with ethanolamine to block the free acid sites - eventually the sensor is brought into contact with the monomer solution under desired condition to monitor the changes in the resonance frequency for amyloid fibril elongation. In the second method, the amyloid fibril is treated with Traut's reagent for a very short amount of time and directly injected over the sensor surface for attachment of the fibrils.

QCM technique is used to investigate two types of kinetic experiments for monitoring the elongation of amyloid fibril. Firstly, only the relative changes in rate of aggregation upon changing the surrounding conditions are investigated, e.g. a comparison the effect of presence and absence of an inhibitor on the fibril elongation rate. On the other hand, the absolute rate of fibril elongation is measured, i.e. the number of protein molecules adding on to a single fibril end per time unit. Upon establishment of the experimental conditions in which the decrease in resonant frequency is, within some range of the total frequency shift, remains proportional to the mass of added protein, and therefore to the total length increase of the surface-bound seed fibrils - the rates of change in the frequency under different conditions can be directly compared. Experiments for measuring the elongation rates are ideally carried out under conditions where no significant depletion of protein molecules in the liquid cell occurs during a measurement. The rate of change in frequency is well approximated as a linear function of time in this example, and may be simply fitted to one [53].

Determination of the seed fibril number density on the surface

This objective can be achieved by imaging of the QCM senor surface with an AFM before or after the experiment and manual counting; where the sensor surface can be dried and simply imaged in air. In the case of high surface densities, it can, however, be challenging to obtain an accurate estimate of the number of density of seed fibrils. It is, therefore, necessary to determine empirically the proportionality coefficient between fibril length increase and frequency shift [53].

Determination of the proportionality factor between attached mass and observed frequency shift

The first is based on the determination of the length increase of amyloid fibrils by AFM imaging. The average length of amyloid fibrils is measured before and after a QCM experiment and the increase in length is correlated with the observed decrease in resonant frequency of the QCM sensor during the experiment. The diameter can also be determined from AFM measurements, and the density can be assumed to be similar to that of a globular protein.

In the second approach, when low concentrations of soluble proteins are used in the case of highly aggregation prone peptides and proteins - the depletion effects can be observed provided that the volume of the liquid cell is sufficiently small. The total observed frequency shift due to the addition of this protein on to the seed fibrils can be measured and then the known amounts of protein (knowing the concentrations and volumes) contacting the seeds can be correlated with the observed frequency shift [53].

1.4.2 Surface plasmon resonance (SPR)

When a photon from incoming light strikes a metal surface, the surface plasmon resonance event occurs (usually a gold surface). A part of the light energy interacts via the metal coating with the free state electrons in the metal surface at a given angle of incidence, promoting electron mobility owing to photo excitation. The collective word for these moving electrons that propagate parallel to the metal surface layer is plasmon. The plasmonic oscillation, in turn, creates an electric field of roughly 300 nm from the metal surface to the sample solution border [141]. Incident light is used in a commercial SPR biosensor configuration by utilizing a high-reflective index glass prism following the Kretschmann geometry of the attenuated total reflection (ATR) technique, in which a prism couples P-polarized light into the sensor covered with a thin metal sheet (Fig. **1-17**). The specified SPR angle, known as the SPR dip angle, at which resonance occurs under the conditions of a constant light source wavelength and a metal thin surface, depends on the refractive index of the material near the metal surface layer [175]. As a result, plasmon cannot occur when the

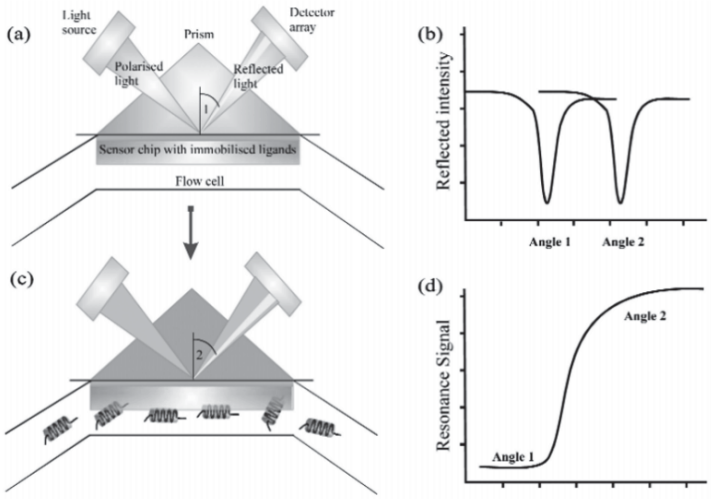

Figure **1-17**: The BIACORE system and the change in incidence angle during a binding process are depicted in this diagram. (a) When no analyte is bonded to the sensor surface, the reflected intensity plot exhibits a steep dip indicating the default incidence angle (b). (c) As the analyte binds to the sensor surface, the absorbed mass on the surface changes, causing the dip indicating the incidence angle to move to angle 2, as illustrated in (b). As indicated in the sensorgram, the change in angle is monitored (d). Adapted with permission from [47].

refractive index of the detecting medium changes slightly (e.g., due to biomolecule attach-

ment). Thus, detection is achieved by detecting changes in reflected light collected on a detector. Furthermore, the quantity of surface concentration may be determined by monitoring the intensity of reflected light or following the resonance angle variations. An SPR biosensor typically has a detection limit of 10 pg/mL. Probe molecules are initially adsorbed on the sensor surface in SPR biosensors. When a solution of target molecules comes into contact with the surface, an affinity interaction between the probe and the target occurs, causing a rise in the refractive index at the SPR sensor surface. In SPR investigations, resonance or response units (RU) are employed to characterize signal changes, with 1 RU equaling a critical angle shift of 104 degrees.

The initial RU value corresponds to the starting critical angle at the start of the experiment, when no probe target interactions have occurred. The change in refractive index Δn_d arisen within a layer of thickness h can be calculated as:

$$\Delta n_d = (dn/dc)_{vol} \Delta\Gamma / h$$

where $(dn/dc)_{vol}$ is the increase of refractive index n with the volume concentration of analyte c and $\Delta\Gamma$ is the concentration of the bound target on the surface [147].

The coupling of incoming light into a propagating surface plasmon (PSP) on a gold surface in real time tracks the change in refractive index. The thickness of the gold surface, the wavelength of the light, and the extent to which the adsorbed mass on the sensor surface are responsible for the change in optical characteristics. As a result, SPR evaluation of binding kinetics can determine the rate of association (k_{on}) during the association phase, the rate of disassociation (k_{off}) when target molecules are removed from the continuous flow by buffer washing, and the association rate constant (k_a) and dissociation rate constant (k_d). The

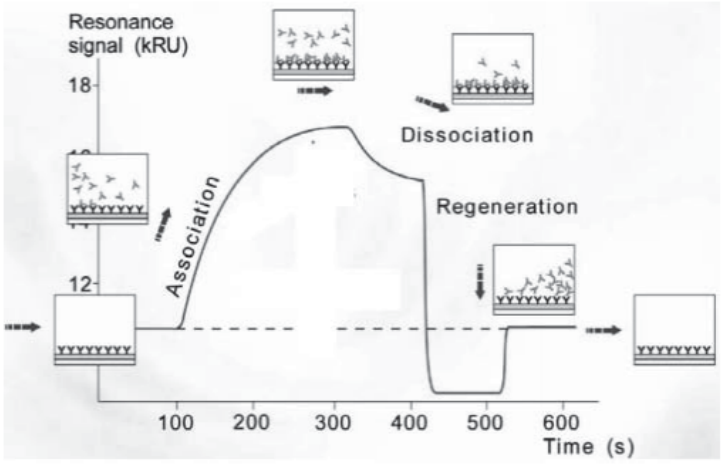

Figure **1-18**: A schematic illustration of a binding event's real-time sensorgram. The analyte is present in the buffer flow during the association phase and binds to the sensor surface. After the analyte is removed from the buffer flow, the dissociation phase begins. The rate and affinity of binding are determined by analyzing these parts of the curves. RU stands for reaction units. Adapted with permission from [47].

refractive index parameter can also be utilized to identify and quantify target molecules attached to a known probe fixed on the sensor surface. The limit of detection (LOD) in an SPR experiment is determined by several parameters, including the molecular weight, optical property, and binding affinity of target-probe molecules, as well as the probe molecule's surface coverage.

A typical SPR sensogram from which information can be obtained after relevant analysis depicting an alternative highly sensitive label-free bio-molecular interactions through ligand-analyte binding scheme, consists of the following steps:-

i. Baseline phase: Initially, baseline buffer is in contact with the sensor surface to establish the baseline. For sensor calibration, this phase (not illustrated) can include the injection of a calibration liquid (e.g., a tuned glycerol percentage injected in baseline buffer) to correct for the analyte buffer's RI bulk shift.

ii. Association phase: The target compound is injected into the sample; the capturing components on the sensor surface bind the chemical, forming a complex.

iii. Dissociation phase: Upon injection of baseline/system buffer, target compounds (and also non-specifically bound molecules) dissociate from the surface.

iv. Regeneration phase: The regeneration solution (e.g. low-pH buffer) is injected to remove the remaining bound target compounds. After this phase, the cycle is completed and a new experiment can start by establishing the baseline again.

Commercially accessible devices (e.g., BIACORE) aid in the fully automation of the SPR method, allowing for the speedy and convenient analysis of huge quantities of samples. In the BIACORE system, ligands are typically immobilised on the surface of a sensor chip made of a thin gold layer, and the analyte is injected over the surface in a continuous flow, which adsorbs onto the immobilised ligand and changes the incidence angle through modification of the refractive index at the sensor chip's surface. Finally, the sensorgram is acquired as a plot of the change in SPR incidence angle vs. time, providing real-time visualization of the binding event between the analyte and the ligand, which may be utilized to understand insights into the binding kinetics of the interaction.

Use of SPR for studying Aβ fibrillation Circular dichroism and fluorescence spectroscopy, electron microscopy, and dynamic light scattering have all been used to analyze amyloid fibril production, a process that leads to numerous neurodegenerative disorders, most notably Alzheimer's Disease (AD). Recently, the SPR method has also contributed to a better understanding of Aβ fibril production by investigations on both the process of Aβ aggregation and the arrest of fibril development by aggregation inhibitors. Early research focused on identifying the critical area of Aβ that is required for binding during polymerisation, which was then utilized to create short peptides that can bind and block polymerisation of full length Aβ into amyloid fibrils.

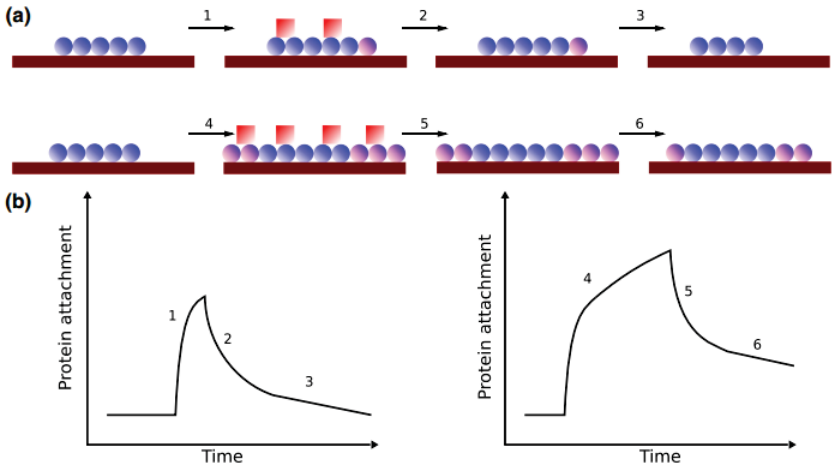

Figure **1-19**: Experiments using surface-based bio-sensing to differentiate fibril development from protein attachment to the fibril surface. (a) Illustration of an amyloid fibril growth experiment on a surface. (1) monomer solution incubation, (2) short buffer wash, (3) long buffer wash (4) a lengthy monomer incubation, (5) a short buffer wash, and (6) a long buffer wash (b) For the example of an SPR experiment, an illustration of the predicted results from the trials in (a) is shown. Long monomer incubation results in biphasic behavior (surface attachment followed by growth), and long buffer washing results in biphasic behavior (surface detachment followed by fibril dissociation). Adapted with permission from [47].

The first application of the SPR technique in measuring the specific interactions of Aβ peptide providing knowledge about the regions of Aβ, most importantly for fibril formation, involved measuring the binding interactions between the KLVFF (shortest peptide capable of binding Aβ) and full-length Aβ peptide. These results were subsequently utilized to confirm and expand the "dock–lock" model of fibril production, which was seen from the two phase kinetics of the SPR signal from surface-bound fibrils following exposure to monomeric protein and subsequent washing with a buffer. The monomer connects to the fibril end weakly and reversibly at first ("dock"), followed by a structural rearrangement and adoption of the fibrilar shape ("lock") [86, 162, 213, 333]. Although this model agrees well with the experimental finding of elongation rate saturation at high monomer concentrations, the bi-phasic behavior observed in these SPR experiments (shown in Fig. **1-19**) cannot be explained in this way.

The biphasic behavior of the SPR signal has been studied in order to unravel and quantify the rate of secondary nucleation during Aβ amyloidosis - a critical phase in the formation of oligomers, the most deadly species produced during AD. Because amyloid fibrils linked to the surface of the SPR sensor are aggregates of hundreds of monomers, "docking" a single monomer to either end should provide a reversible amplitude significantly smaller than the entire mass surface-bound to the sensor. The dissociation signal, on the other hand, has a significantly greater reversible amplitude, which can be readily explained by assuming that the monomer weakly absorbs to the entire fibril surface but not preferentially towards the

fibril ends. Re-evaluation of previously published data within the context of SPR research reveals that a quick pseudo-equilibrium is created between free monomer and monomer weakly linked with binding sites on the fibril surface, which is consistent with recent QCM experiments. The shorter the incubation time period with monomer solution, the larger the bias towards (weak, easily reversible) surface attachment, and the longer the incubation time, the greater the bias towards (less reversible) elongation. This behavior has been studied in depth for the Aβ peptide, and it has been discovered that the monomer's affinity for the fibril surface is 100 times weaker than that for the fibril end and careful analysis of the dissociation signal can be used to calculate the rate of secondary nucleation fitting with a proper surface-adsorption model [355].

1.5 Aim of the thesis

The human brain contains various N- and C-terminally modified Aβ variants generating dominantly from the different enzymatic cleavage pathways of the AβPP and Aβ(1-42) fibril derived from the *in-vivo* condition exhibits different polymorphism compared to the fibrils derived from different *in-vitro* conditions. These observations have bolstered the urgent need to investigate the mechanistic insights into the cross-secondary nucleation possibly occurring *in-vivo* due to binding interactions between different monomeric Aβ isoforms and the Aβ(1-42) fibrils inside the mixed-peptide systems. pE-Aβ(3-42) is found to be present as a dominant N-terminal truncated Aβ isoform, besides the full-length Aβ(1-42) peptide in the amyloid plaque analysis. So, pE-Aβ(3-42) and Aβ(1-42) peptides were chosen for the current study for the thermodynamic and conformational analysis of their binding with the Aβ(1-42) fibril to understand the mechanistic insights of cross-secondary nucleation at atomic-scale, which might open up the route to develop potential molecular candidates for a therapeutic approach in AD pathology.

To achieve our aim, we employed a dual research direction through computational enhanced sampling molecular dynamics simulation method and surface-based bio-sensing experimental methods, which earlier proved to be quite important tools for understanding the insights of the sub-microscopic process of amyloidogenesis. We hypothesized towards a deep understanding of the thermodynamic insights into the monomers binding the fibril surface to unravel the cross-secondary nucleation pathway taken by both Aβ isoforms on the Aβ(1-42) fibril surface in terms of atomic-scale analysis of the conformations adopted by them, both in the presence and absence of the fibril surface.

Towards these goals, Chapter 2 aims at finding a good choice of initial parameters and computational method for studying conformational analysis of Aβ(1-42) peptide at the atomic scale and compare it with the previous studies, so that these sets of methodologies can be taken as standard in later studies. Then, Chapter 3 aims to investigate the monomeric conformations adopted by pE-Aβ(3-42) peptide at the atomic scale (using the computational methodologies as obtained from Chapter 1) and how it differs structurally from that of Aβ(1-42) monomer towards explaining the observed biophysical properties of pE-Aβ(3-42). In the final step, Chapter 4 first aims at understanding the thermodynamic insights of sec-

ondary nucleation interactions occurring between the monomeric Aβ isoforms and Aβ(1-42) fibril surface through investigating the interactions in bulk solution using QCM-D & SPR methodologies. Later, it aims towards understanding the observed outcomes at the atomic scale through the implication of advanced computational methodologies for investigating the binding interactions, structural insights and thermodynamic parameters of both the monomers of Aβ isoforms binding with the Aβ(1-42) fibril surface. Particularly, this whole work aims toward understanding the thermodynamics of binding between the two dominant Aβ isoforms along with the conformational analysis of their monomers, which targets to lay down the basics of understanding the insights into the dynamics of possible cross-secondary nucleation occurring in a mixed peptide system similar to *in-vivo* conditions and it's implications towards AD pathology.

2 Amyloid β-peptide (1-42) monomer forms compact fibril-like structure

Article information
Title: Compact fibril-like structure of amyloid β-peptide (1–42) monomers
Authors: Bogdan Barz[1,2], Alexander K. Buell[3] and Soumav Nath[1,2]
1) Institut fur Physikalische Biologie, Heinrich-Heine-Universitat Dusseldorf, Dusseldorf, Germany
2) Institute of Biological Information Processing – Structural Biochemistry (IBI-7), Research Centre Julich, Julich, Germany.
3) Department of Biotechnology and Biomedicine, Technical University of Denmark, Lyngby, Denmark
Journal: Chemical Communication
Year: 2021
Volume: 57
Pages: 947-950
DOI: 10.1039/d0cc06607a

2.1 Abstract

Amyloid β (Aβ) monomers are the smallest assembly units, and play an important role in most of the individual processes involved in amyloid fibril formation. An important question is whether the monomer can adopt transient fibril-like conformations in solution. Here we use enhanced sampling simulations to study the Aβ(1-42) monomer structural flexibility. We show that the monomer frequently adopts conformations with the N-terminus region structured very similarly to the conformation it adopts inside the fibril. This intrinsic propensity of monomeric Aβ to adopt fibril-like conformations could explain the low free energy barrier for Aβ(1-42) fibril elongation.

2.2 Introduction

The formation of Aβ amyloid fibrils is a complex process, including primary and secondary nucleation reactions, as well as fibril elongation [172], and Aβ monomers take part in most of these individual steps. While in typical in vitro experiments the monomer is depleted during the aggregation reaction, it is constantly being produced in vivo and therefore all monomerdependent steps are likely to be important during the entire duration of the disease. It is thus very important to characterize the monomer structure in order to understand

how its sequence encodes the tendency to form larger assemblies and how partly structured monomeric species might facilitate the formation of highly toxic intermediates. Thus far, experimental studies revealed diverse conformations of Aβ monomers either with high helical content [321, 260] or with a random coil type of structure [218]. Computationally, the Aβ(1-42) monomer structure has been studied with various simulating techniques and force fields [276]. The general picture that emerges from the numerous molecular dynamics (MD) simulation studies on the Aβ monomer is that the observed structural characteristics are very diverse and highly dependent on the simulation conditions [276]. This variability possibly reflects the finding that the disordered structural ensemble manifests itself differently under different solution conditions, when probed with different types of experimental techniques [170] or at different stages of the aggregation process [353]. Despite the emergence of coarsegrained or atomistic force fields tailored for intrinsically disordered proteins which produce conformational ensembles more and more similar to those observed in experimental studies [208, 184, 61], monomeric structures of Aβ(1-42) that resemble peptides from the recent fibril models have not been observed thus far [106, 49]. Such a conformation would have strong implications for the aggregation process, but especially for the fibril elongation by monomer addition observed in experimental studies [103], because it may provide mechanistic insight into the misfolding process. In this study we report the occurrence of a significantly populated set of conformations observed during Hamiltonian replica exchange simulations with many structural features in common with the so-called S-shape fibril models. Computational details are provided in the Appendix. We first describe the structural features that contribute to the stability of this conformation, followed by a comparison with recent fibril models and a discussion regarding the implications for the fibril elongation.

2.3 Results and Discussions

The overall structural ensemble sampled in the unbiased simulation trajectory has characteristics similar to those observed in experimental NMR studies [218], i.e. the $^3J_{HNH\alpha}$ NMR couplings shown in Fig. **2-4** with a $\chi^2 = 2.5$. Further comparison with computational and experimental quantities are provided in Appendix. The fibril-like structure has been identified as the cluster with the largest population. An overview of the top five clusters is displayed in Fig. **2-5** where intramolecular contact maps are shown for each cluster together with the representative structures and populations. Cluster one has a population (14.4%) considerably larger than the rest and constant for different RMSD cutoffs (see Appendix). We have identified structural elements that make the conformation in cluster one unique and discuss them here, while details regarding other clusters are discussed in Appendix. The first defining characteristics of this structure, as seen in Fig. **2-1** (a), are its compact shape and two short parallel β-sheets. The backbone atoms of the peptide form a spiral-like structure, Fig. **2-1** (b), where the N-terminus shown in blue forms a first loop until the middle part of the peptide, residue N27, comes in contact with the N-terminus. We label this region as the N-terminus loop. The rest of the peptide, K28–A42, forms a second loop labeled as the C-terminus loop. The two loops appear as two different flat surfaces stacked on top of each other, see Fig. **2-1** (c) and (d). Another important characteristic is the location of many hydrophobic amino acids in the interior of the two loops and shielded from the solvent to

some degree. Within the N-terminus loop one can identify in Fig. **2-1** (c) the following hydrophobic amino acids pointing towards the interior of the loop: A2, F4, H6, V18, and F20. Within the C-terminus loop, Fig. **2-1** (d), the following hydrophobic amino acids are oriented inwards: I31, M35, V36, V39, and I41. As will be discussed below, the orientation of the amino acids within the C-terminus loop resembles to a large degree that from the fibrilar states of the peptide. Two crucial factors that contribute to the stability of this conformation are salt bridges and parallel β-sheets.

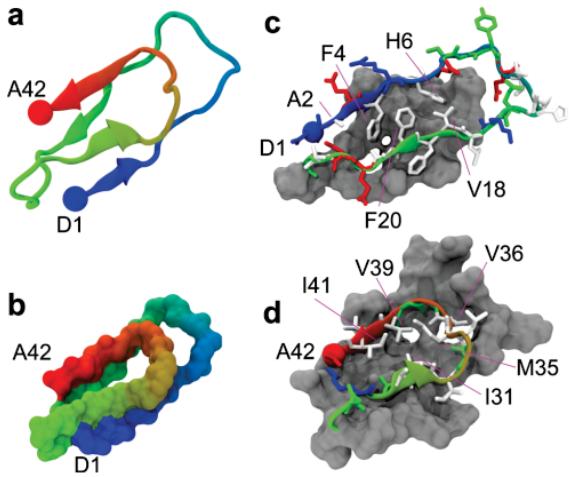

Figure **2-1**: Structure of the fibril-like monomer. (a) Cartoon representation highlighting the secondary structure, the N-terminus shown in blue and the C-terminus shown in red. (b) Surface representation of the backbone which emphasizes the coiled geometry. (c) N-terminus loop with all amino acids shown in licorice representation and colored by the type of amino acid (white – hydrophobic, red – negatively charged, blue – positively charged and green – polar). The C-terminus loop is shown as gray surface. (d) C-terminus loop is displayed similarly to (c) and the N-terminus loop is shown as gray surface. Adapted with permission from [35].

The two loops are both closed by salt-bridges. The N-terminus loop is stabilized by a salt-bridge between D1 and D23, Fig. **2-6** (a) and the C-terminus loop is stabilized by two salt bridges formed by K28 with D23 or with A42, Fig. **2-6** (b). A detailed analysis is provided in the appendix together with Fig. **2-7** - Fig. **2-9**. Based on the salt-bridge analysis we have estimated that, for this cluster, salt-bridge D23–D1 was present in 93.16% of the fibril-like conformation, while salt-bridges E22–K28 and A42–K28 in 60.20% and 46.12% of the conformations, respectively. Previous computational studies have identified the E22/D23–K28 salt-bridge [309, 70, 38], but not the other two observed in the fibril-like structure from this study. In addition to the salt-bridges, two parallel β-sheets located at opposite positions give further stability to this structure. The two β-sheets are shown in Fig. **2-6** (c) and (d), and are formed between E3–F4 and A30–I31 in the first β-sheet and between V18–F20 and V39–I41 in the second β-sheet. They can also be identified in the contact map of cluster one from the Fig. **2-5** as some of the strongest contacts.

We have thus identified three main features of this compact structure that make it unusually stable compared to structures reported by other studies [184, 61, 176]. The salt-bridges

together with the parallel β-sheets preserve the two big loops in contact while allowing the hydrophobic amino acids to interact with each other shielded from the solvent inside the convoluted conformation. In order to estimate the lifetime of the fibril-like conformation we performed five classical MD simulations starting from the center of cluster one. By considering as RMSD cutoff a value of 0.4 nm, we identified an average lifetime of the conformation of 249.6 $\pm$ 41.1 ns. This is in agreement with a recent computational study which identifies meta-stable states of the Aβ(1-42) monomer with sub-microsecond lifetimes [188]. Another computational study [36] has shown that compact conformational states, including those of monomers, are less engaged in the early Aβ(1-42) assembly process and might be able to explain the oligomer size distributions observed experimentally [44, 42]. The monomer conformation described above fits very well in this category of compact intermediates and could also contribute to the formation of compact meta-stable dimers or higher oligomers. The compact Aβ(1-42) conformation discussed above, and the special role the N-terminus plays in its stability, might be very relevant for mutations A2T and A2V. A2T has been reported to be protective against AD [155], while A2V was shown to protect heterozygous carriers but to cause dementia in homozygous carriers [101]. If the compact monomer promotes fibril formation, then it is possible that a mutation to a very hydrophobic residue V at position A2 could increase its stability, while a mutation to the polar residue T could destabilize it and lead to reduced aggregation compared to wild type or the A2V mutation [200].

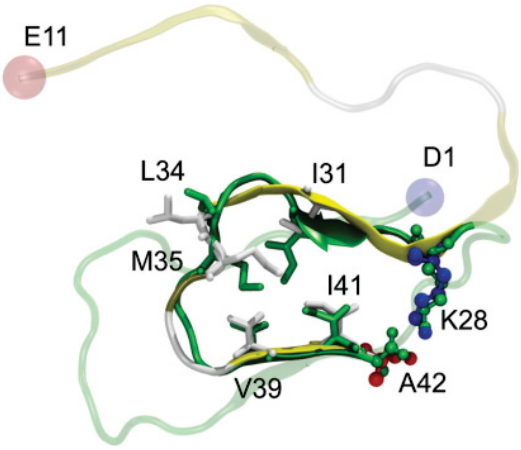

Figure **2-2**: Comparison of the compact monomer with the S-shape fibril model with PDB ID: 2MXU by Xiao et al.[338] Only the backbone atoms were used for the structural alignment. Both peptides are shown in cartoon representation and selected amino acids as licorice or balls and sticks. The fibril-like monomer state is colored in green while the fibrilar peptide is colored based on its secondary structure, its hydrophobic amino acids in white, and the charged residues K28 in blue and A42 in red. Adapted with permission from [35].

One of the main features of the compact Aβ(1-42) monomer discussed above is the structure of the middle and C-terminus region which forms a closed loop via two salt-bridges. This peptide sequence, K28–A42, has a structure very similar to peptides found in recent experimental fibril models, referred to as the S-shape fibrils. To clarify this we have aligned the structure containing the sequence K28–A42 from the compact monomer and that of

fibrilar peptides from three different models as shown in Fig. **2-2** and Fig. **2-10**: (a) a single filament fibril obtained at pH of 7.4 by Xiao et al. [338] (b) a double filament fibril obtained at pH of 8 by Colvin et al.[68], and (c) a double filament obtained at pH of 2 by Gremer et al.[121] Note that the simulations performed in our study correspond to a pH of 7.4. The smallest backbone RMSD for residues K28–A42 is obtained for the single filament fibril model of Xiao et al.[338] Fig. **2-2**, with a value of 0.15 nm. One important aspect of the structural comparison, visualized in Fig. **2-2**, is the orientation of the side chains of hydrophobic amino acids from the simulated structure, which point all in the same direction as the ones from the fibrilar peptide. The same applies to K28 and A42, involved in a salt-bridge. Additional RMSD values for the N-terminus loop and the full-length peptide are discussed in the Appendix.

As shown above, the C-terminus loop of the folded conformation is in very good agreement with all three fibril models. This means that the observed Aβ(1-42) monomer is able to sample, besides a multitude of disordered states, partly structured conformations that mimic the Aβ(1-42) fibril core without interfering with the overall random-coil behavior of the conformational ensemble. While the C-terminus loop resembles the fibril structure the most, the N-terminal loop does so to a lesser degree but provides a scaffold for the C-terminal loop to fold and an increased stability to the compact structure. The folded monomer conformation observed in our simulations and discussed above has many characteristics similar to the fibril core. In addition, the N-terminus loop covers completely one side of the C-terminus loop, see Fig. **2-1** (c) and (d). We have investigated how such a conformation could fit at the end of a fibril assuming an in-register interaction between the C-terminus loop of the folded monomer and the C-terminus region of a peptide at the fibril end. To identify which end of the fibril is optimal for this type of docking, we have aligned the folded monomer with a peptide from the fibril end using only the residues K28–A42, and making sure that the N-terminus loop is located towards the solvent and not towards the fibril. It is important to

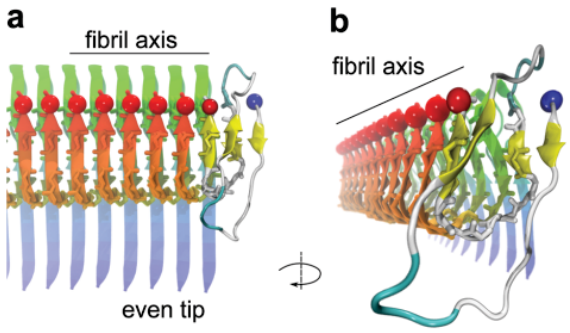

Figure **2-3**: Structural fit of the compact fibril-like monomer at the fibril end. (a) The fibril-like monomer is shown at the even fibril end (C-terminus less exposed to the solvent). The monomer is colored by the secondary structure elements and the fibrilar peptides with color gradient from blue at N-terminus to red at C-terminus. The N- and C-termini are shown as blue and red spheres, respectively. (b) The same structure from (a) is slightly rotated for a better view along the fibril axis. Adapted with permission from [35].

note here the assumption that the conformation of the fibril end is identical to the overall fibrilar conformation. The result of these docking experiments can be seen in Fig. **2-3** from two different angles. From Fig. **2-3** (a) it is clear that the folded monomer has a near-optimal alignment with the even tip of the fibril which has the C-terminus less exposed to the solvent. These results are interesting in the context of the discussion of two proposed mechanisms for fibril elongation: "fast deposition" and "dock-lock". During the "fast-deposition", a so-called activated monomer is efficiently deposited onto a fibril end and thus becomes incorporated into the fibril [201, 300]. The compact monomer from our study would most likely fulfill the structural requirements for an activated conformation involved in the "fast deposition" process. In "dock-lock", during the "dock" phase a monomer attaches somewhat non-specifically and therefore rather weakly to the fibril end in a fully reversible manner [103], while during the "lock" phase, which takes place on a much slower time scale [50], the monomer undergoes a structural rearrangement until it either dissociates off again or it achieves the most stable, correctly incorporate state, which often for practical purposes appears to be irreversible. The "dock-lock" mechanism has been proposed from experiments [94] and was also observed in several computational studies [300, 60], with a clear prevalence over the "fast deposition". For Aβ(1-40), the binding of monomers to fibrils has been shown experimentally to involve region F19–N27 and to a lesser degree K16–A21 [45]. It would be interesting to investigate whether a similar mechanism is present for Aβ(1-42) and what role the compact monomer conformation identified in our study plays in the binding process. Regardless of whether or not the fibril-like conformation of the monomer actually is on the pathway to an incorporated monomer, the identification of such a class of fibril-like structures allows us to rationalise certain features of the aggregation behaviour of the Aβ peptide. It has been consistently found that the Aβ(1-42) peptide has one of the smallest known free energy barriers for fibril elongation by monomer addition of all amyloid polypeptides [103, 52, 65]. This finding could be explained by the innate tendency of the Aβ sequence to adopt conformations similar to those inside the fibril. The importance of the fibril-like state that the monomer adopts in isolation for the elongation reaction depends on whether the templating fibril end should be regarded as a strong or weak perturbation of the mono-molecular free energy landscape explored in the present work. Some experimental evidence for an important role of the fibril end comes from the observation that the two ends of a fibril often grow with different rates [351], in agreement with the different efficiency in docking to the two ends, as demonstrated in this work. However, answering this question will ultimately require more extensive simulations of monomer-monomer and monomer-fibril interactions.

2.4 Conclusion

In conclusion, using enhanced sampling MD simulations, we have identified a transient monomer structure of Aβ(1-42) that accounts for a significant population of the total observed conformations. This structure has many characteristics similar to fibrillar forms of the Aβ(1-42) peptide. To the best of our knowledge this is the first Aβ(1-42) monomeric structural ensemble to feature a state with such a high degree of similarity with the S-shape fibril core. This suggests that the Aβ(1-42) peptide in monomeric form already has a tendency

to sample structural features specific to fibrils and could explain why Aβ(1-42) has a very low free energy barrier for fibril elongation. This monomer model could guide experiments in identifying new aggregation intermediates with specific structural characteristics.

2.5 Acknowledgement

We gratefully acknowledge financial support from the Deutsche Forschungsgemeinschaft (DFG, German Research Foundation) grant BA 5956/2-1. A. K. B. thanks the Novo Nordisk Foundation for support through a Novo Nordisk Foundation Professorship (NNFSA170028392). The authors also gratefully acknowledge the computing time granted by the John von Neumann Institute for Computing (NIC) and provided on the supercomputer JURECA at Julich Supercomputing Centre (JSC).

2.6 Methods

MD simulations details. We have studied the conformational flexibility of the Aβ(1-42) monomer in water by performing HREMD [56] simulations using the Charmm36m force field [137] and the Charmm TIP3P water model designed for folded proteins and IDPs. The TIP3P water model was modified such that it leads to an increased protein - water interaction [137]. In Charmm36mW, the Lennard Jones well depth parameter of the hydrogen atoms have been modified from -0.046 kcal/mol to -0.10 kcal/mol as suggested by Huang et al.[137] The Charmm36m force field together with the modified TIP3P water model are labeled as Charmm36mW. The simulations were performed with the Gromacs 2016.04 parallel software package[132]. Short range electrostatics and van der Waals interactions were cut at 0.1 nm, while long range electrostatic interactions were treated with the Particle Mesh Ewald method. The temperature was kept at 300 K via velocity re-scaling with a stochastic term algorithm [55] and a time constant for coupling of 0.1 ps. The pressure coupling was controlled with the Parrinello-Rahman barostat [230, 219] with a time constant of 1 ps. The hydrogen atoms were treated as virtual interaction sites, allowing an integration time step of 4 fs while maintaining energy conservation [102]. To simulate physiological conditions we also included 150 mM NaCl concentration. The solution structure of Aβ(1-42) protein monomer with PDB ID 1IYT was used as starting conformation [71]. The conformation was placed in a dodecahedral box with 1.6 nm between the protein and the box, solvated with water molecules, 43 Na and 40 Cl ions. The final systems had 47,054 atoms. This simulation box was large enough to allow free translation and rotation of the Aβ(1-42) monomer without interacting with its periodic images that would otherwise result in simulation artifacts. After energy minimization, position restrained equilibration (with the Berendsen barostat) and a short free equilibration (with the Parrinello-Rahman barostat), the Hamiltonian replica exchange1 simulation was performed, consisting of 12 simulations run in parallel, each simulation having a different interaction Hamiltonian where non-bonded interactions and dihedral angles are scaled with a factor λ or $\sqrt{\lambda}$. The biasing coefficients can be expressed as an inverse temperature (1/temperature) correspond to temperatures between 300 and 500 K and assigned to the replicas according to a geometric distribution. The average replica exchange probability was 24%. We thus performed one H-REMD simulations

of 3.4 μs/replica, with 12 replicas in total, amounting to a total simulation time of 40.8 μs on the the supercomputer JURECA [160] at the Jülich Supercomputing Centre (JSC).

Data analysis

Since all simulations started from the Aβ(1-42) structure with the PDB code ID: 1IYT [71], the initial state has large number of amino acids in helical conformation, see Fig. **2-12**. The highly helical conformation drops to small values below 10 residues within 1,500 ns as can be seen in Fig. **2-12**. The drop in helical conformation is accompanied by an increase in the β-sheet content. Given the random coil character of the Aβ(1-42) monomer observed in experiments [261], we have decided to analyze only the equilibrated part the simulation, where fluctuations in the secondary structure are similar to those of random coil, i.e. without many amino acids in helical conformation. Thus, the time interval used for the analysis consist of the last 1,000 ns of the unbiased trajectory, highlighted in Fig. **2-12**.

$^3J_{HNH\alpha}$ NMR scalar couplings.

$^3J_{HNH\alpha}$ NMR scalar couplings were calculated with the Karplus equation for each amino acid:

$$\langle 3J_{HNH\alpha} \rangle = \langle A\cos^2\phi + B\cos\phi + C \rangle \tag{2-1}$$

with coefficients $A = 7.97$ Hz, $B =$ - 1.26 Hz and $C = 0.63$ Hz [322]. The comparison with experimental data was done using the reduced χ^2:

$$\chi^2 = \frac{1}{N}\sum_{i=1}^{N}\frac{J_{i,exp} - \langle J_i \rangle_{sum}}{(\Delta J_i)^2} \tag{2-2}$$

where $(\Delta J_i)^2 = (\Delta_{\text{block}})^2 + (\Delta_{\text{Karplus}})^2$, Δ_{block} being the simulation error calculated with block averaging and $\Delta_{\text{Karplus}} = 0.42$ Hz, the experimental error.

Secondary structure, contact maps and clustering. For snapshots of the protein structure we used the program Visual Molecular Dynamics (VMD) [139] where the secondary structure is calculated with STRIDE [108]. Contact maps were calculated using the Contact Map Explorer module implemented in Python and considering a contact between two amino acids when any two atoms from the two residues were found at a distance below a cutoff of 0.5 nm. Clustering of structures was performed with the Daura algorithm [84] implemented in Gromacs using the backbone atoms and an RMSD cutoff of 0.4 nm. In order to assess the sensitivity of the most populated cluster to the cutoff used for the RMSD, we have recalculated the cluster distributions using additional cutoff values. Thus, we have performed in total three clustering calculations with cutoffs of 0.35 nm, 0.4 nm and 0.45 nm. The total number of clusters increases with increasing the cutoff as follows: 2435 clusters for a cutoff of 0.35 nm; 3205 clusters for a cutoff of 0.4 nm; and 4198 clusters for a cutoff of 0.45 nm. Despite the changes in the number of clusters, the population of the first cluster remained consistently at 14 of the total number of structures for each cutoff value. In addition to cluster one, discussed in the main text, of particular interest are the clusters two and three,

which contain rather extended conformations with many similarities. As can be seen from the contact maps in Fig. **2-5**, these two clusters have strong contacts with patterns that correspond to anti-parallel β-sheets between amino acids Y10-D23 and A42-S26. In the representative structures can also be identified two anti-parallel β-sheets of different lengths in agreement with the contact map. This type of structure might be relevant for the formation of the U-shape fibrils [187], where anti-parallel contacts are present between amino acids L17-G25 and V40-I32 for the side-chains.

β-sheet content, radius of gyration and hydrodynamic radius. The random coil behaviour of the Aβ(1-42) monomer observed in NMR experiments was also confirmed by circular dichroism (CD) spectroscopy experiments where the Aβ monomers adopt between 12–25% β-sheet and much lower helical content [183, 223]. Using the DSSP [167] software together with the Gromacs tool "do–dssp" we calculated an average β-sheet propensity of 19.6% $\pm$ 2.9, in good agreement with experimental values. In order to characterize the conformational diversity of the monomeric Aβ, we have calculated the radius of gyration of all conformations in the simulation. The average radius of gyration has a value of 1.4 $\pm$ 0.3 nm, slightly smaller than values reported by other computational studies, i.e. 1.6 nm [208] and 1.59 nm [184], but within error. Using an empirically parametrized equation which relates the radius of gyration to the hydrodynamic radius for intrinsically disordered proteins [222], we have determined an averaged hydrodynamic radius of $\sim$1.7 $\pm$ 0.1 nm, in good agreement with experimental values of both Aβ(1-40), i.e. 1.6 nm [120], and the upper range of values for Aβ(1-42), i.e. 0.9–1.8 nm [217, 212, 286, 331, 220].

RMSD of compact monomer with peptides from fibril models. Here we continue the discussion from the main text regarding the comparison of the C-terminal loop from the compact monomer with other fibril models. In the case of the double filament structure published by Colvin et al. [68], the smallest RMSD has a value of 0.19 nm. Fig. **2-10** (b) shows all hydrophobic amino acids pointing in the same direction, except for M35. When compared with fibrils obtained at pH of 2 and in the presence of an organic co-solvent by Gremer et al.[121], Fig. **2-10** (c), the RMSD has a value of 0.17 nm. Despite the very small backbone RMSD, only L34 and M35 from the monomer point in the same direction as the residues in the fibrilar peptide. The mismatches are not surprising, given the effect of the low pH on the protonation state of charged amino acids and eventually on the overall structure of the fibril, possibly exacerbated by the organic co-solvent. For completeness, we also compared the full length and the N-terminus loop of the monomer with the peptides from fibril models and we report the values in Table **2-1** from Appendix. The RMSD for the full length peptide have values between 0.82 and 1.14 nm indicating a poor structural fit. When considering only the N-terminus loop, the RMSD varies between 0.27 and 1.12 nm, with the lowest value for the fibril model with PDB ID: 2MXU. This case is also displayed in Fig. **2-11** where one can identify an extended peptide chain for both the monomer and the peptide from the fibril model.

Salt-bridge analysis. In addition to the salt-bridge discussion from the main text we include the following results regarding the salt-bridges formed by K28. From Fig. **2-6** (b) it is clear

that E22 and A42 are close to each other and form alternating or simultaneous salt-bridges with K28. We have identified the conformations where K28 forms salt-bridges with both E22 and A41 and calculated a propensity of 29.85%. This means that within cluster one, K28 was engaged in salt-bridges with either E22 or A42 in 76.47 % of the conformations.

Salt-bridge analysis details. To quantify the occurrence of the salt-bridges that stabilize the compact monomer we have calculated distances between the two oxygen atoms of the negatively charged amino acids (E22 and D23, A42) and the three hydrogen atoms of the positively charged ones (D1 and K28) involved in the salt bridge.The results for the three salt bridges obtained from all the conformations in cluster one of the simulation with Charmm36mW and NaCl are shown in Figs. **2-7** (D23-D1), **2-8** (E22-K28) and **2-9** (A42-K28). In the case of salt-bridge D23–D1, most of the conformations have either the distance between oxygen O1 or oxygen O2 of residue D23 and the three hydrogens of residue D1 below 0.4 nm which is the threshold distance to qualify as a salt-bridge. This is also shown in the normalized distributions from Fig. **2-7** Bottom where the largest peaks below 0.4 nm belong to distances between O2 and H1 or H2. The dynamics of this salt bridge is clear from the plots in Fig. **2-7** Middle for both a) and b), where the three hydrogens alternate as the closest atom to the oxygen O1 or O2, with oxygen O2 being preferred for shorter distances. A similar analysis is shown in Figure for salt-bridge E22–K28 and in Fig. **2-9** for salt-bridge A42–K28. Salt-bridge E22–K28 appears in a large number of structures from cluster one, but is not as stable as D23–D1.

2.7 Appendix - Chapter 2

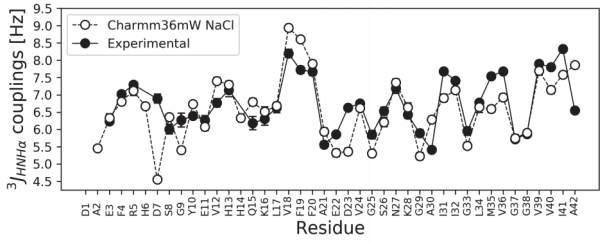

Figure **2-4**: $^3J_{HNH\alpha}$ NMR scalar couplings calculated for each amino acid for Charmm36mW force field with 150 mM NaCl. Experimental values are shown as black circles and those obtained from the simulations as white circles. The error bars were calculated using block averaging. Adapted with permission from [35].

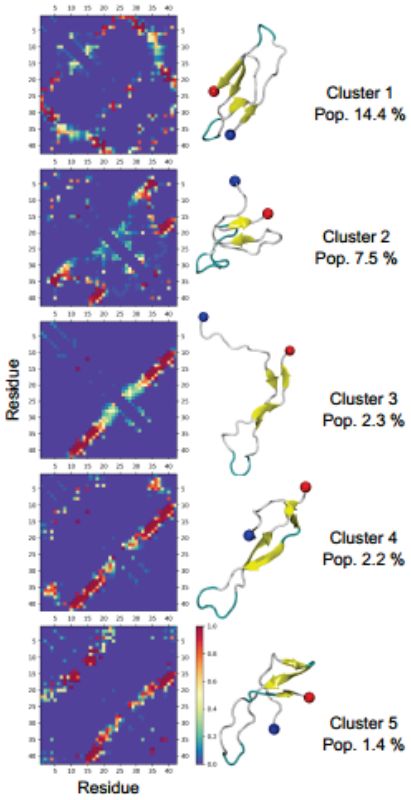

Figure **2-5**: Contact maps and structures for top five clusters with the highest population. Adapted with permission from [35].

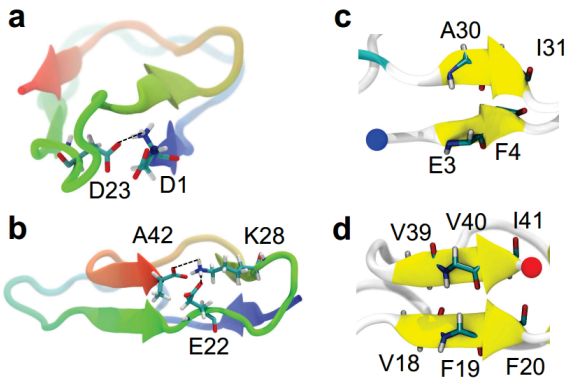

Figure **2-6**: Salt-bridges and β-sheets of the compact monomer. a) and b) show salt-bridges D1-D23 and K28-E22/A42, respectively. c) and d) show the two parallel β-sheets located at E3-F4 with A30-I31 and V18-F20 with V39-I41, respectively. Adapted with permission from [35].

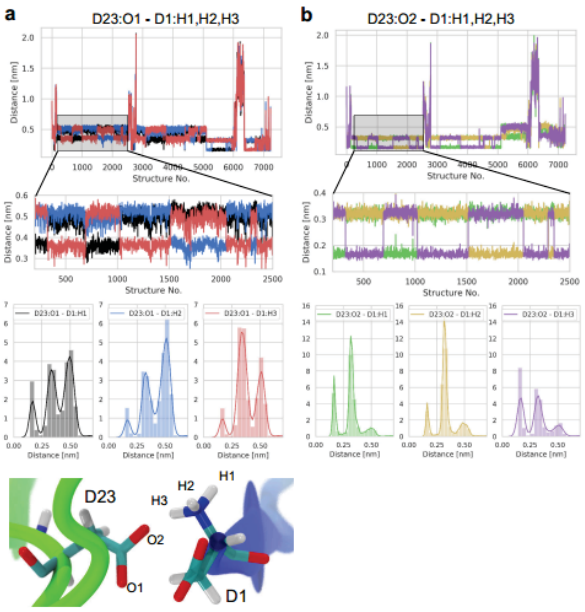

Figure **2-7**: Salt-bridge distances for D23–D1. a) Top - Distance between the oxygen atom O1, see Bottom snapshot, of group COO- of residue D23 and the hydrogen atoms of group NH3+ of residue D1 for all the conformations in cluster one of the simulation with Charmm36mW and NaCl. Middle - Short interval from the plot in a) which highlights the swaping of hydrogens for the shortest distance with the oxygen atom. Bottom - Normalized distributions for distances between the oxygen atom O1 and the three hydrogens. Bottom snapshot - Licorice representation of the amino acids D23 and D1 and the atoms forming the salt-bridge. b) Same as a) but for distances between oxygen O2 of group COO- of residue D23 and the hydrogen atoms of group NH3+ of residue D1. Adapted with permission from [35].

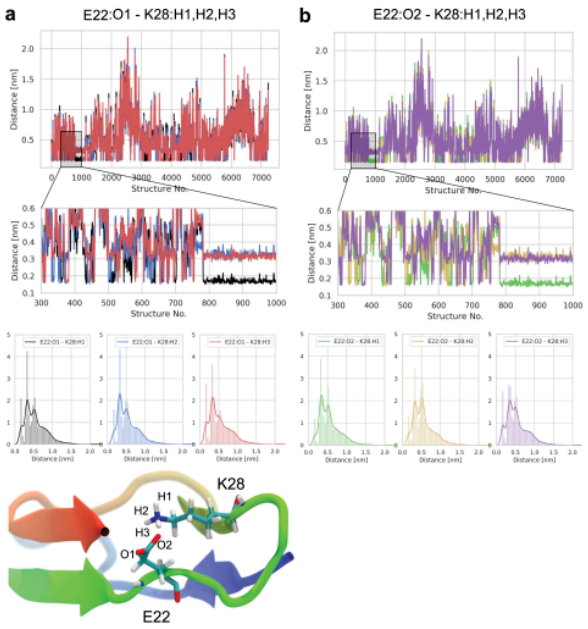

Figure **2-8**: Salt-bridge distances for E22–K28. a) Top - Distance between the oxygen atom O1, see Bottom snapshot, of group COO- of residue E22 and the hydrogen atoms of group NH3+ of residue K28 for all the conformations in cluster one of the simulation with Charmm36mW and NaCl. Middle - Short interval from the plot in a) which highlights the swaping of hydrogens for the shortest distance with the oxygen atom. Bottom - Normalized distributions for distances between the oxygen atom O1 and the three hydrogens. Bottom snapshot - Licorice representation of the amino acids E22 and K28 and the atoms forming the salt-bridge. b) Same as a) but for distances between oxygen O2 of group COO- of residue E22 and the hydrogen atoms of group NH3+ of residue K28. Adapted with permission from [35].

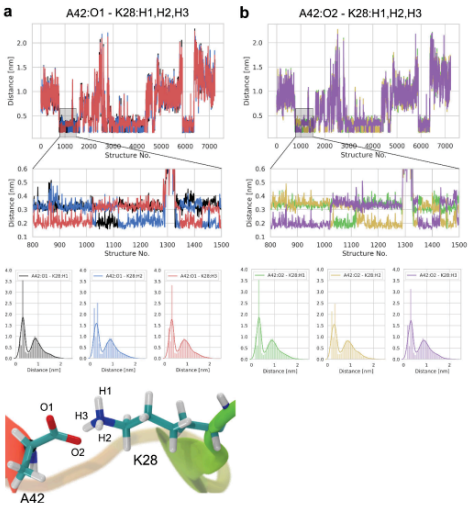

Figure **2-9**: Salt-bridge distances for A42–K28. a) Top - Distance between the oxygen atom O1, see Bottom snapshot, of group COO- of residue A42 and the hydrogen atoms of group NH3+ of residue K28 for all the conformations in cluster one of the simulation with Charmm36mW and NaCl. Middle - Short interval from the plot in a) which highlights the swaping of hydrogens for the shortest distance with the oxygen atom. Bottom - Normalized distributions for distances between the oxygen atom O1 and the three hydrogens. Bottom snapshot - Licorice representation of the amino acids A42 and K28 and the atoms forming the salt-bridge. b) Same as a) but for distances between oxygen O2 of group COO- of residue A42 and the hydrogen atoms of group NH3+ of residue K28. Adapted with permission from [35].

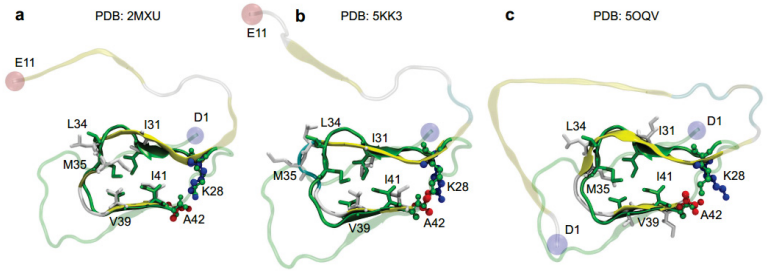

Figure **2-10**: Comparison of the compact monomer with S-shape fibril models. Only the C-terminus loop was used for the structural alignment. All peptides are shown in cartoon representation and selected amino acids as licorice or balls and sticks. The fibril-like monomer state is colored in green while the fibrillar peptide is colored based on its secondary structure, its hydrophobic amino acids in white, and the charged residues K28 in blue and A42 in red. Three fibril models were considered with PDB IDs: a) 2MXU [338], b) 5KK3 [68], and c) 5OQV [121]. Adapted with permission from [35].

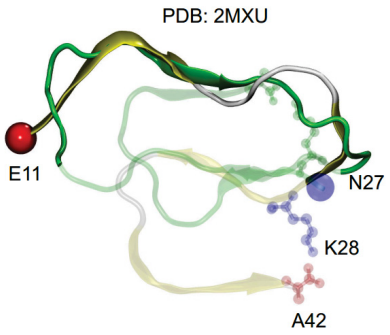

Figure **2-11**: Structural alignment between the N-terminus loop of the compact Aβ(1-42) monomer and the fibril model with PDB ID 2MXU. Both proteins are shown in cartoon representation with the monomer colored in green and the fibril peptide based on the secondary structure. Region E11-N27 is highlighted, while the rest of the proteins is transparent. The backbone RMSD associated with this region is 0.27 nm. Adapted with permission from [35].

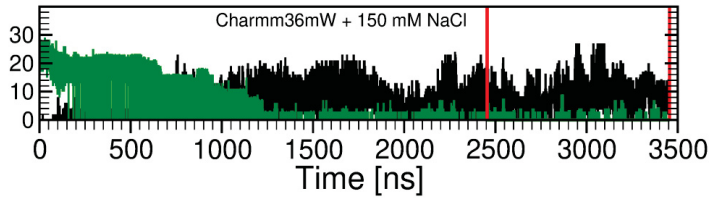

Figure **2-12**: Evolution of the number of residues adopting sheet (black) or helix (green) conformations during the H-REMD simulation. The vertical red lines indicate the interval considered for detailed analysis. Adapted with permission from [35].

Table **2-1**: Backbone RMSD values between the compact monomer and three Aβ(1-42) fibril models. We considered three cases where the RMSD was calculated for the full length peptide, the N-terminus loop and the C-terminus loop. Two of the fibril models (2MXU and 5KK3) lack structural information for the first 10 amino acids, therefore the full length and the N-terminus loops are truncated accordingly when calculating the RMSD. Adapted with permission from [35].

Sequence	RMSD [nm]	RMSD [nm]	RMSD [nm]
	2MXU	5KK3	5OQV
D1(E11)-A42	0.82	0.92	1.14
D1(E11)-N27	0.27	0.42	1.12
K28-A42	0.16	0.21	0.18

3 Pyroglutamate-modified amyloid β(3-42) monomer is more disordered than amyloid β(1-42) monomer

3.1 Abstract

The aggregation of the amyloid β (Aβ) peptide is a major hallmark of Alzheimer's disease. This peptide can aggregate into oligomers, proto-fibrils, and mature fibrils, which eventually assemble into amyloid plaques. Several post-translational modifications lead to the presence of different isomers of Aβ peptide in the amyloid plaques with different biophysical and biochemical properties. While Aβ-40/42 have been found to be the major components of amyloid plaques, the pyroglutamate-modified variants, specifically pE-Aβ(3-42), amount to around 25-50% of the total Aβ plaque content of AD brains. With increased stability and hydrophobicity, these variants display a more aggressive behaviour during AD and their contribution to the disease is considered critical. The peptide monomers are the smallest assembly units, and play an important role in most of the individual processes involved in amyloid fibril formation, such as primary and secondary nucleation and elongation. Understanding the monomer structure of the isomers is essential in unraveling observed differences in their bio-physio-chemical properties. Here we use enhanced and extensive molecular dynamics simulations to study the structural flexibility of the N-terminally truncated Pyroglutamate modified isomer of Aβ, pE-Aβ(3-42) monomer, and compared it with the Aβ(1-42) peptide monomer under the same conditions. We find significant differences, especially in the secondary structure and hydrophobic exposure, which might be responsible for their different behaviour in experiments.

3.2 Introduction

Extracellular deposits of insoluble fibrils in the human brain are the major hallmark of the neurodegenerative disorder Alzheimer's Disease (AD) leading to cognitive and memory impairment due to neuronal and synaptic losses. These extracellular plaques are mainly composed of deposits from amyloid-β (Aβ) peptides [136, 229, 12]. The two main Aβ variants found in the brain differ only by two C-terminal amino acids, with Aβ(1-40) being more abundant than Aβ(1-42) ($\sim$5-10%). In AD patients, however, the extracellular concentration of Aβ(1-42) has been shown to be considerably increased [282, 305]. Although long C-terminal fragments of Aβ, i.e. Aβ-40/42, have been found to be the major component of amyloid plaques, several N-terminally truncated Aβ variants have been found to be present in a significant amount as well [303, 352, 129]. Pyroglutamate-modified Aβ (pEAβ) peptides

result from the side reaction by the enzyme glutaminyl cyclase (QC) beside APP cleavage. In particular, pE-Aβ(3-42) is the major isoform among these species - representing around 25-50% of the total Aβ content in senile plaques of AD brains [352, 129, 150, 283]. pE-Aβ(3-42) is found to be stable to degradation inside the body from amino peptidases due to the the lack of free amino acid at the N-terminus [39]. As a result of the the N-terminus truncation with the loss of two negatively and one positively charged amino acids and the pyroE modification with the formation a lactam ring at the third residue, significant alterations in the biophysical and biochemical properties of pE-modified Aβ arise. These include increased hydrophobicity, higher β-sheet content through accelerated fibrillation kinetics and faster oligomerization rate compared to the unmodified Aβ peptide resulting in the increase in toxicity of the pE-Aβ(3-42) peptides [285, 130, 284].

The presence of pE-Aβ(3-42) has been found to accelerate the aggregation propensity of Aβ(1-42) via catalytic increase in both the primary and secondary nucleation rates [80]. However, some studies have found similar aggregation propensities of the pE-Aβ(3-42) peptide compared to that of Aβ(1-42) [278], which might be due to the experimental conditions used in different studies. Despite pE-modified Aβ variants having higher β-sheet propensity, fibrils of pE-Aβ(3-40) and pE-Aβ(11-40) have been found to be similar in structure with the unmodified Aβ(1-40) fibrils. The N-terminally truncated pE-modified Aβ fibrils also show high rate of fragmentation [281, 335] not present in the unmodified peptide. pE-Aβ(3-42) also influences Aβ(1-42) during the early stage of aggregation by altering the secondary structure of Aβ(1-42) assemblies through a template-dependent prion-like mechanism thereby rapidly forming highly toxic hetero-oligomers structurally distinct from both pE-Aβ(3-42) and Aβ(1-42) [221, 202, 119]. Some studies have implemented solution-NMR methods to characterize the secondary structure of pE-Aβ(3-x) isoforms and indicated that both pE-Aβ(3-40) and pE-Aβ(3-42) have a higher β-sheet content than the unmodified peptides. Furthermore, the aggregation of pE-Aβ(3-42) into fibrils involves transient intermediates rich in α-helical secondary structure [81, 82].

Elucidating the molecular structure of the N-terminally truncated pE-Aβ peptides in relation with the unmodified alloforms is crucial to understanding the change in their biophysical and biochemical properties during aggregation. 3D structures published thus far indicate that Aβ(1-42) adopts a mostly helical conformation in apolar micro-environment [71] which starts to vanish as soon as polar solvent is added [312]. More recent NMR experiments of Aβ monomers in water reveal that both the Aβ(1-40) and (1-42) alloforms behave as random coil [261], with a transient β-sheet structure for Aβ(1-42). Computationally, the Aβ(1-42) monomer structure has been studied with various simulating techniques and force fields [218]. The general picture that emerges from the numerous molecular dynamics (MD) simulation studies on Aβ monomer is that the observed structural characteristics are very diverse and highly dependent on the simulation conditions [218]. Recently, modern force fields tailored for intrinsically disordered proteins start producing conformational ensembles more and more similar to those observed in experimental studies [208, 184].

Here, we report conformational ensembles of pE-Aβ(3-42) by using Hamiltonian replica

exchange MD simulations and provide a detailed comparison with the Aβ(1-42) monomer. Our structural comparison indicates considerable differences between the two peptides which might be responsible for their different aggregation behaviours observed in experimental studies.

3.3 Results and Discussions

The structural ensembles of pE-Aβ(3-42) and Aβ(1-42) sampled in the H-REMD simulations indicate many similarities as well as differences in the behavior of the monomeric peptides in water. Below we present a detailed comparison between the two Aβ variants.

pE-Aβ(3-42) and Aβ(1-42) monomers adopt a random coil structure in water. NMR couplings are often used for describing the local structure of intrinsically disordered proteins. Recently, Roche *et al.* [261] measured various NMR parameters of Aβ(1-40) and Aβ(1-42) in solution and concluded that both peptides lack a stable structure and behave very similarly to a random coil. We calculated the $^3J_{HNH\alpha}$ NMR couplings for pE-Aβ(3-42) and Aβ(1-42), Fig. **3-1**, as described in the Methods section, and compared these with experimental values reported for Aβ(1-42) peptide [261]. For a quantitative comparison we use the reduced χ^2 quantity. Overall we obtained a χ^2 value of 2.5 for Aβ(1-42) and 2.9 for the pE-Aβ(3-42) excluding the pE3 amino acid. The good agreement between the simulated and experimental

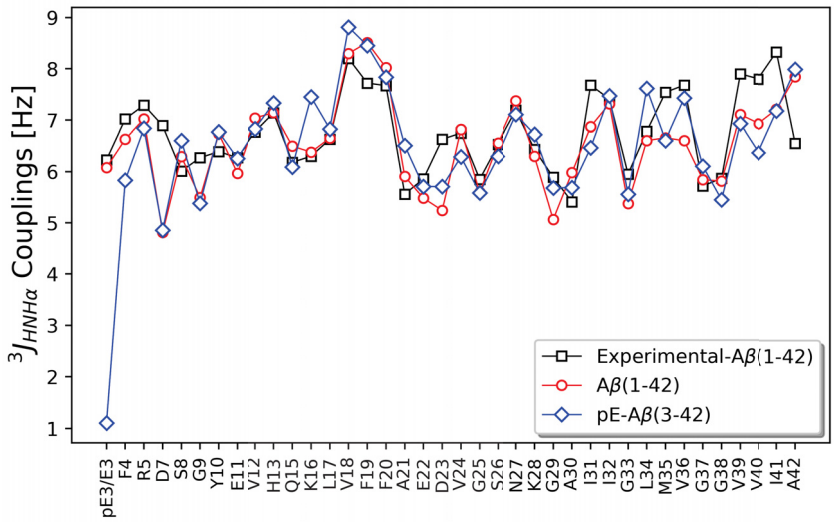

Figure **3-1**: NMR scalar couplings and secondary structure. Top - $^3J_{HNH\alpha}$ NMR scalar couplings calculated for each amino acid for Charmm36mW force field with 150 mM NaCl.

$^3J_{HNH\alpha}$ couplings for Aβ(1-42) is an improvement compared to reported χ^2 values from other computational studies [208, 184]. The largest deviations from experimental values for the Aβ(1-42) peptide are at D7, D23 and A42, while the pE-Aβ(3-42) peptide differs the most from the Aβ(1-42) experimental values at amino acids F4 (due to pE3), K16, I31, V40 and A42. Besides the considerable impact of the N-teminal truncation and its modification to more hydrophobic pyroglutamate residues on the J-couplings of the first two amino acids

of pE-Aβ(3-42), overall, the isoform behaves fairly similar to the Aβ(1-42) peptide. Some notable exceptions are differences at K16 and V40, where pE-Aβ(3-42) has larger and lower values, respectively, compared to both experimental and simulated values of Aβ(1-42). These differences may be linked to different types of dominant conformation observed in the cluster analysis as described later. In Fig. **3-1** Top, the central hydrophobic cluster amino acids V18–F20 and the C-terminal V39–I41, have values close or above 7.5 Hz for both variants indicating that these residues are good candidates for forming β-sheets. This behavior, also observed in previous experimental studies [218, 347, 262], is of crucial importance for the fibril-formation given the importance of the central hydrophobic during this process [41].

Conformations of pE-Aβ(3-42) have increased β-sheet and α-helix propensity. The secondary structure propensity per amino acid provides complementary structural information to the J-coupling analysis. We have thus calculated the β-sheet propensity per amino acid for each of the peptides. Both cases, shown in Fig. **3-2**, display a similar main pattern, which is the presence of meta-stable β-sheets for the central hydrophobic cluster (the amino acids L17-A21) and the hydrophobic C-terminus (A30-I41), with higher propensities for pE-Aβ(3-42), especially at L34-V36. High β-strand propensities of L17-A21 and I31-V36 for the Aβ(1-42) monomer have been observed previously in several computational studies [218]. The average β-sheet propensity for Aβ(1-42) and pE-Aβ(3-42) monomers are 19.45% $\pm$ 2.74 and 27.07% $\pm$ 3.29, respectively. The propensities, especially that of pE-Aβ(3-42), are in good agreement with the experimental value of 25.2% reported for Aβ(1-40) monomers [223]. The largest β-sheet propensity for both peptides is at the central hydrophobic cluster, reaching the highest values for V18 and F19. This is in agreement with the observation that in NMR experiments amino acids V18, F19 and F20 are the residues most likely to have extended conformations for Aβ(1-42) monomer [261].

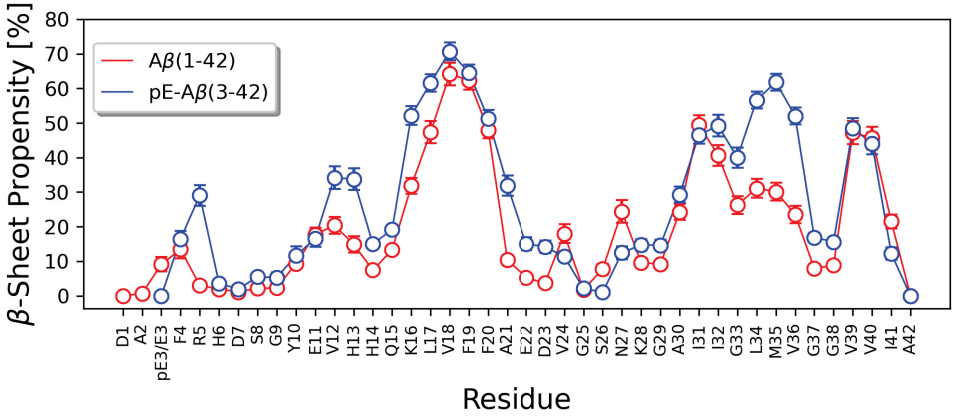

Figure **3-2**: β-Sheet propensity per residue for pE-Aβ(3-42) (in Blue) and Aβ(1-42) (in Red).

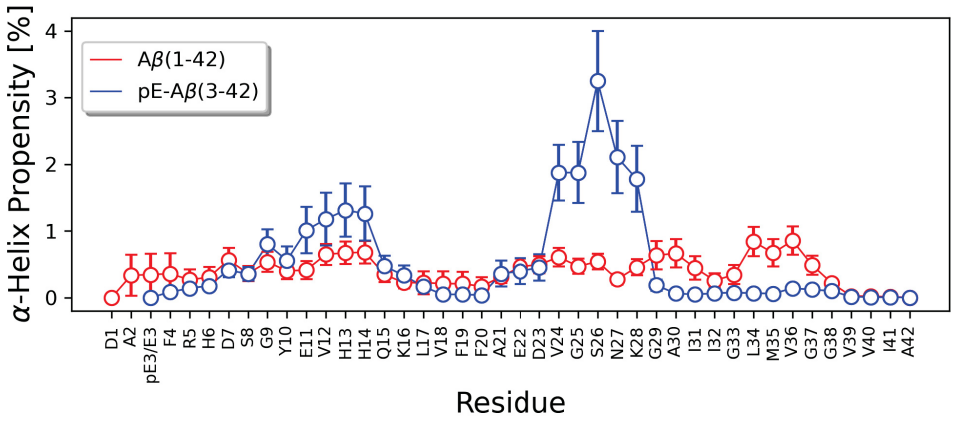

Figure **3-3**: α-Helix propensity per residue for pE-Aβ(3-42) (in Blue) and Aβ(1-42) (in Red).

In addition, we calculated the alpha-helix propensity for both peptides. For pE-Aβ(3-42), we observed a slightly larger helix propensity than for Aβ(1-42). The largest difference in alpha-helix propensity is for residues V24-K28 which in pE-Aβ(3-42) is about two times higher than in Aβ(1-42). This indicates that pE-Aβ(3-42) intermediate conformations are more prone to form helical structures which is in agreement with an experimental study showing that the aggregation of the pE-Aβ(3-42) into fibrils occurs via an α-helix rich intermediate monomer [81, 82].

These results suggest that pE-Aβ(3-42) is more aggregation-prone having larger β-sheet propensity as well as states with α-helical secondary elements. Roche *et al.* [261] showed that Aβ(1-42) monomers lack any long lasting secondary structure, as long as the propensity of these elements is below 50%. With few exceptions, the amino acids of Aβ(1-42) from this work do have β-sheet propensities below 50%, which suggests that the significant amount of β-sheet content is subject to constant fluctuations and the conformational ensemble is very diverse. This is also confirmed by the average percentage of β-sheet which is in agreement with experimental values that are compatible with a random coil. pE-Aβ(3-42) contains three additional amino acids with β-sheet propensities above 50%, L34, M35 and V36, which could have an impact on the aggregation pathway. Additional properties of the conformational ensemble which emphasize structural differences between the two peptides are discussed below.

The largest cluster of pE-Aβ(3-42) has hydrophobic residues exposed to solvent. One of the main differences between the two peptides can be observed in the clustering analysis where the structures are grouped into different clusters based on their structural similarity. The populations of the top ten clusters are shown in Table **3-2**. The largest cluster for pE-Aβ(3-42) has a population of 18.38%, while for Aβ(1-42) a population of 6.08%. This result indicates that pE-Aβ(3-42) prefers to adopt the conformation specific to this cluster in almost 20% of cases, or three times more than Aβ(1-42) monomer adopts the structure of its largest cluster. The rest of the top ten clusters have rather similar populations, below 4% and decreasing rapidly to 1% and below. Intra-molecular contact maps for the largest

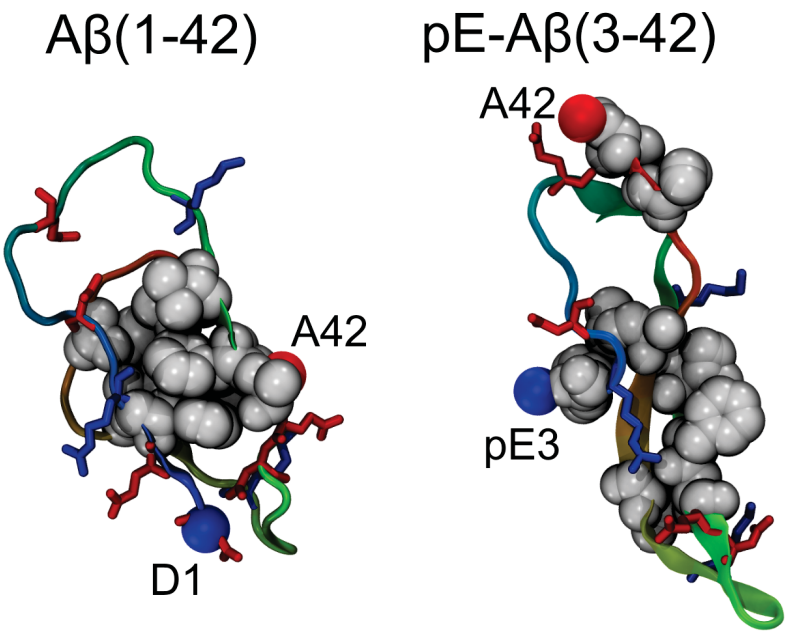

Figure **3-4**: Distribution of hydrophobic amino acids (in white) in the representative structure of the most populated cluster of Aβ(1-42) (left) and pE-Aβ(3-42) (right). Charged amino acids are also shown in blue and red for positive and negative net charge, respectively.

clusters of the two peptides, shown in Figure S2 and S3, indicate clear structural differences. In the case of Aβ(1-42), the conformation is compact, has features similar to peptides from fibrils and has been fully described in a recent study [35]. Some of the key features are short parallel β-sheets, salt bridges involving the two termini and partial shielding of hydrophobic amino acids. The representative conformation for pE-Aβ(3-42) , shown in Fig. **3-9** (A), has an elongated shape and anti-parallel β-sheets. It is particularly interesting the very long β-sheet structure involving 16 residues among which are also ones from the center hydrophobic cluster K16-E22. Another important difference between the two structures is the spatial distribution of hydrophobic amino acids. In the case of Aβ(1-42), residues F4, V18, F20, A21, I31, M35, V39 and I41 are all packed inside the folded monomer and partially shielded from solvent. The same amino acids are in the case of pE-Aβ(3-42) directly exposed to the solvent without much shielding as observed for Aβ(1-42) and with fewer hydrophobic contacts. This is illustrated in Fig. **3-4**.

pE-Aβ(3-42) shows strong signature of anti-parallel β-sheet patterns. The contact maps of the two studied cases calculated from the 2 μs long trajectories reveal intramolecular interactions that are highly related to the β-sheet content discussed above. Contact maps are excellent tools for describing precise intra-molecular interactions and were calculated for both peptides during the 2 μs trajectories. pE-Aβ(3-42), shown in Fig. **3-5** Top, has the strongest contacts as a clear linear pattern perpendicular to the main diagonal, which indicate contacts with anti-parallel symmetry. This pattern forms between residues E11-V24

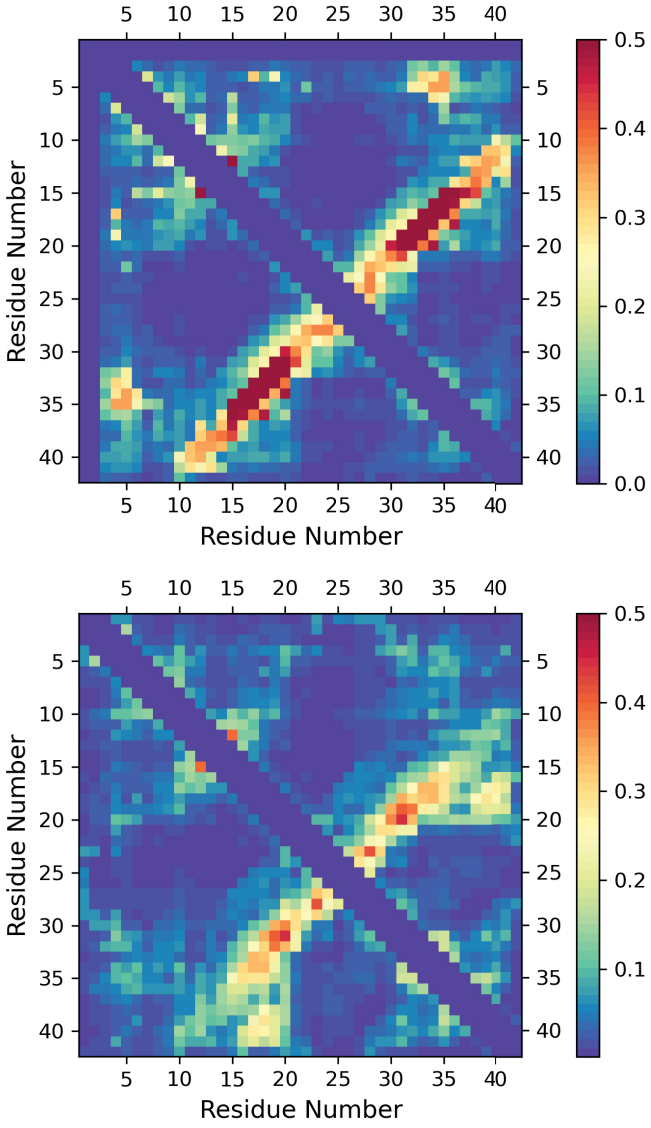

Figure **3-5**: Contact Maps of 2 μs trajectory for pE-Aβ(3-42) (Top) & Aβ(1-42) (Bottom)

and I41-N27 with a width of 2-4 residues and has the strongest contacts with probability above 50% for regions H14-F20 in contact with V36-I31. The main anti-parallel pattern is also present in the contact maps of clusters 1, 5,9 and 10 of pE-Aβ(3-42) from Fig. **3-10**. Another notable contact region is between amino acids F4-H6 and I32-M35, which is less present in the Aβ(1-42) monomer, and can be identified in the representative structure of the largest cluster as a short antiparallel β-sheet between the N-terminus and the part of the C-terminus hydrophobic region I32-L34. Both the above patterns are present in the representative conformation of cluster 1 from Fig. **3-9**.

Aβ(1-42) shows a similar anti-parallel β-sheet pattern as the pyroglutamate modified peptide, which extends between residues E11-V24 and I41-N27. Its probability, however, is considerably reduced, with few contacts reaching values above 40%. An additional patch of contacts is present between residues from the central hydrophobic cluster, K16-F19, and the C-terminus region G38-I41. This is not the case for pE-Aβ(3-42), in agreement with

the results from the main clusters where pE-Aβ(3-42) has many hydrophobic amino acids exposed to the solvent. The central hydrophobic cluster, K16-E22, plays a crucial role in the Aβ aggregation as it can form fibrils on its own. The fact that it is in contact with the C-terminus in the Aβ(1-42) monomer but not in the pE-Aβ(3-42), suggests that the pyroglutamate variant may be more prone to aggregating than the 42 amino acids alloform.

N-terminal differences lead to unique salt bridges in the two peptides. Salt bridge bonding between charged amino acids of a peptide plays an important role in determining the structural conformation of the particular peptide. In particular, intra-peptide salt bridges were shown to play an important role in stabilizing the Aβ(1-40) fibril structure [290]. Aβ(1-40) modified by a lactam bridge D23-K28 formed fibrils 1000-fold faster, suggesting that a rate limiting nucleation step was bypassed [290]. Here, we have calculated the propensity of intra-peptide salt bridge formation between charged amino acids within pE-Aβ(3-42) and Aβ(1-42).

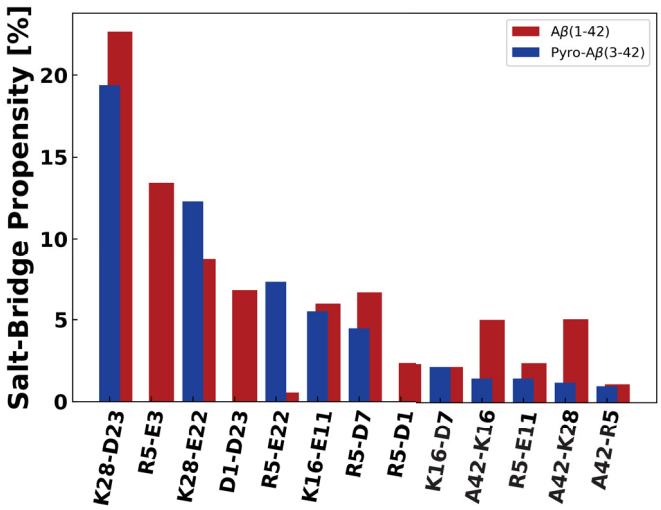

Figure **3-6**: Propensity of salt-bridge formation for pE-Aβ(3-42) (in maroon) and Aβ(1-42) (in blue).

In our simulations, both alloforms formed a large diversity of salt bridges with the highest propensity for D23-K28 which had propensities close to 20%. The pyroglutamate variant had significantly stronger salt bridges at E22-K28 and R5-E22, the later almost absent in Aβ(1-42). In return, Aβ(1-42) had unique salt bridges at R5-E3 and D1-D23. One should note that amino acids D1 and E3 are not present in pE-Aβ(3-42). In this analysis we observed that, while in Aβ(1-42) D23 forms salt bridge with D1, it is less engaged in salt bridge formation during the simulation of pE-Aβ(3-42) where D1 is missing. Thus, the availability of this negatively charged residue is likely to lead to an increased aggregation propensity when several pE-Aβ(3-42) peptides are engaged with each other, compared to Aβ(1-42).

Radius of gyration, end–to–end distance and solvent accessible surface area (SASA). In order to further characterize the conformational diversity of the monomeric pE-Aβ(3-42) and compare them with Aβ(1-42), we have calculated distributions for the radius of gyration and show them in Fig. **3-11**. The distributions have similar shapes, with a strong

peak between 1 and 1.5 nm, and a large shoulder that extends up to 2 nm. The average radius of

Table **3-1**: Average values and standard deviations for the radius of gyration, end to end distance, and SASA for the three cases.

	Radius of Gyration [nm]	Hydrodynamic Radius [nm]	EE Distance [nm]	SASA - All Residues [nm^2]	SASA - Hydrophobic Residues[nm^2]
pE-Aβ(3-42)	1.37 ± 0.2	1.66 ± 0.1	2.29 ± 0.9	41.6 ± 4.2	22.4 ± 3.1
Aβ(1-42)	1.47 ± 0.3	1.72 ± 0.1	2.73 ± 0.9	45.2 ± 4.9	22.0 ± 3.4

gyration values from Table **3-1** indicate less compact conformations for Aβ(1-42) with an average value of 1.47 nm and more compact conformations for the pE-Aβ(3-42) an average value of 1.37 nm. Using an empirically parametrized equation which relates the radius of gyration to the hydrodynamic radius for intrinsically disordered proteins [222], we have determined hydrodynamic radius distributions for the two peptides, shown in Fig. **3-12**. The average values obtained are 1.66 for pE-Aβ(3-42) and 1.72 for Aβ(1-42), which are in very good agreement with experimental values of both Aβ(1-40), i.e. 1.6 nm [120] which is also similar to pE-Aβ(3-42) peptide consisting of 40 amino acid residues, and the upper range of values for Aβ(1-42), i.e. 0.9–1.8 nm [217, 212, 286, 331, 220]. The average end–to–end distance, follows a similar trend as the radius of gyration, with a value of 2.3 nm for pE-Aβ(3-42) and 2.7 nm for Aβ(1-42) respectively. The wide distributions of the end–to–end distance, shown in Fig. **3-13**, and the standard deviations of ∼1 nm indicate similar types of structural fluctuations in these two peptides. This is also confirmed by the SASA distributions, Fig. **3-14**, with average values of ∼ 42 nm^2 for pE-Aβ(3-42) and ∼ 45 nm^2 for Aβ(1-42) (which are close to those reported by Krupa *et al.* [176]. Interestingly, the shape of the Aβ(1-42) SASA distribution for all amino acids has larger probability density values at large SASA values. This is not the case for the SASA of hydrophobic amino acids residues, Fig. **3-15**, where pE-Aβ(3-42) has increased probability at higher SASA values, indicating more hydrophobic amino acids exposed to the solvent, as also concluded in the sections above.

Overall, this analysis showed small variations in the mean values of several characteristics of the two peptides. However, the shape of the distributions and the general trend suggest key differences in the features of the pE-Aβ(3-42) conformational ensemble which may lead to strong effects during the self-assembly process. One of these effects could be the accelerated aggregation into fibrils of pE-Aβ(3-42), at concentrations ten times smaller than Aβ(1-42), as confirmed by ThT fluorescence experiments [83].

3.4 Conclusions

The pyroglutamate modified Aβ peptides have altered aggregation and stability properties [151]. They are resistant to degradation due to the presence of the pyroglutamate residue and the lack of several charged amino acids makes them more hydrophobic [277]. This also leads to increased β-sheet formation and accelerated aggregation [131] compared to the full-length variants. An essential question is whether the structure of the monomer has any influence on this behaviour.

Using extensive enhanced molecular dynamics simulations, we have shown that both the pE-Aβ(3-42) and Aβ(1-42) monomers adopt a random coil structure in water, however, with specific differences at structural level. The pyroglutamate variant has higher β-sheet propensities for N-terminal amino acids, increased helix propensity, more hydrophobic amino acids exposed to the solvent and the D23 residue more available for inter-molecular interactions than the Aβ(1-42) monomer. All these differences could have a contribution to the distinct aggregation pathways of the two peptides observed in experimental studies. A critical process in the amyloid aggregation is the secondary nucleation where the oligomer formation is catalysed by the presence of the fibril surface. Thus, studying the interaction of Aβ monomers with the fibrils should be a natural next step for further understanding the implications of the monomer structure in the complete self-assembly process.

3.5 Methods

MD simulations details

Aβ1-42 monomer simulation. To study the conformational flexibility of the pE-Aβ(3-42) and Aβ(1-42) monomers we performed H-REMD [56] simulations with the Charmm36m force field [137] and the Charmm TIP3P water model designed for folded proteins and IDPs. In addition, the Charmm TIP3P water model was modified with an increased protein - water interaction, and labeled as Charmm36mW [137]. In Charmm36mW, the Lennard Jones well depth parameter ϵ of the hydrogen atoms has been modified from -0.046 kcal/mol to -0.10 kcal/mol as suggested by Huang et al. [137]. Simulations with Charmm36mW were considered with 150 mM NaCl concentration in order to reproduce physiological conditions.

The solution structure of Aβ(1-42) protein monomer with PDB ID: 1IYT was used as starting conformation [71]. The conformation was placed in a dodecahedral box with 1.6 nm between the protein and the periodic boundaries, solvated with water molecules and 43 Na and 40 Cl ions were added to also account for 150 mM salt concentration. The final systems had 47,054 atoms. This simulation box was large enough to allow free translation and rotation of the Aβ(1-42) monomer without interacting with its periodic images that would otherwise result in simulation artifacts.

The starting conformation of pE-Aβ(3-42) monomer was built after deletion of first three amino acids from Aβ1-42 protein monomer with PDB ID: 1IYT and inserting Pyrogluta-

matic acid with PDB ID: PCA. After structural alignment, the equilibrium parameters for pyroglutamate molecule were generated using the GAUSSIAN [107] software package and then inserted into Charmm36mW force field. The conformation was solvated with modified TIP3P water molecules and 150 mM NaCl ions. This resulted in a system with a total of 46,875 atoms.

After energy minimization, position restrained equilibration (with the Berendsen barostat) and a short free equilibration (with the Parrinello-Rahman barostat), Hamiltonian replica exchange [56] simulations were was performed for each system. Each H-REMD simulation consisted of 10 (Amber99SB*-ILDN) or 12 (Charmm36m and Charmm36mW) simulations running in parallel, each simulation having a different interaction Hamiltonian where non-bonded interactions and dihedral angles are scaled with a factor λ. The biasing coefficients lambda can be expressed as an inverse temperature (1/temperature) correspond to temperatures between 300 and 500 K and assigned to the replicas according to a geometric distribution. In total we performed two H-REMD simulations, one for each system, of 4 μs/replica. All simulations were performed on the supercomputer JURECA [160] at the Jülich Supercomputing Centre (JSC). The average replica exchange probability for the four systems had values between 16% and 25%.

All simulations were performed with the Gromacs 2016.04 parallel software package [132]. Short range electrostatics and van der Waals interactions were cut at 0.1 nm, while long range electrostatic interactions were treated with the Particle Mesh Ewald method. The temperature was kept at 300 K via velocity rescaling with a stochastic term algorithm [55] and a time constant for coupling of 0.1 ps. The pressure coupling was controlled with the Parrinello-Rahman barostat [230, 219] with a time constant of 1 ps. The hydrogen atoms were treated as virtual interaction sites, allowing an integration time step of 4 fs while maintaining energy conservation [102].

Analysis. For both peptides therefore we have chosen to analyze the last 2,000 ns of the unbiased trajectory in order to sample the well equillibrated conformations.

$^3J_{HNH\alpha}$ **NMR scalar couplings** were calculated with the Karplus equation for each amino acid:

$$\langle 3J_{HNH\alpha}\rangle = \langle A\cos^2\phi + B\cos\phi + C\rangle \tag{3-1}$$

with coefficients A = 7.97 Hz, B = - 1.26 Hz and C = 0.63 Hz [322]. The comparison with experimental data was done using the reduced χ^2:

$$\chi^2 = \frac{1}{N}\sum_{i=1}^{N}\frac{J_{i,exp} - \langle J_i\rangle_{sum}}{(\Delta J_i)^2} \tag{3-2}$$

where $(\Delta J_i)^2 = (\Delta_{\text{block}})^2 + (\Delta_{\text{Karplus}})^2$, Δ_{block} being the simulation error calculated with block averaging and $\Delta_{\text{Karplus}} = 0.42$ Hz, the experimental error.

Secondary structure, contact maps and clustering. Secondary structure propensities per residues were calculated with the program DSSP [167] and the errors with block averaging.

For snapshots of the protein structure we used the program Visual Molecular Dynamics (VMD) [139] where the secondary structure is calculated with STRIDE [108]. Contact maps were calculated using the Contact Map Explorer module implemented in Python and considering a contact between two amino acids when any two atoms from the two residues were found at a distance below a cutoff of 0.5 nm. Clustering of structures was performed with the Daura algorithm [84] implemented in Gromacs using the backbone atoms and an RMSD cutoff of 0.4 nm.

Radius of gyration, hydrodynamic radius, end–to–end distance and SASA. The radius of gyration was calculated using the function compute-rg from the MDTraj library [205] implemented in Python. From the radius of gyration we calculated the hydrodynamic radius of each conformation using an empirically parametrized equation specifically derived for intrinsically disordered proteins [222]. The end to end distance was calculated between the C_α atoms of the first and last amino acids using the function compute-distances from MDTraj. To calculate the SASA we used the shrake-rupley algorithm [293] implemented in MDTraj.

3.6 Acknowledgement

The authors gratefully acknowledge the computing time granted by the John von Neumann Institute for Computing (NIC) and provided on the supercomputer JURECA at Jülich Supercomputing Centre (JSC). We also acknowledge DFG grant BA 5956/2-1 for funding the current research. AKB thanks the Novo Nordisk Foundation for support through a Novo Nordisk Foundation Professorship (NNFSA170028392).

3.7 Appendix - Chapter 3

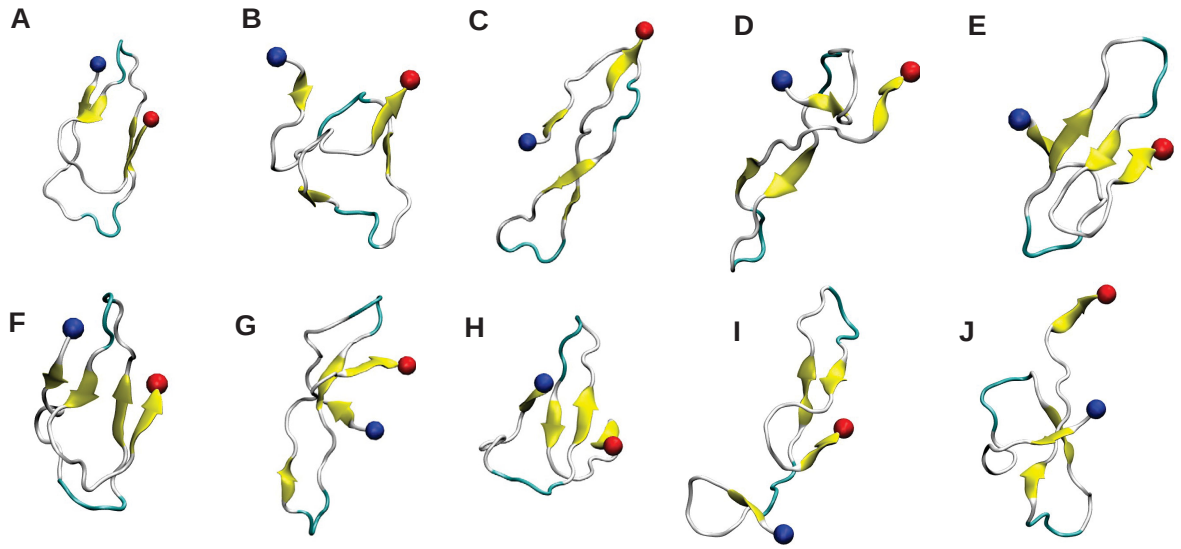

Figure **3-7**: Secondary Structures of Top-10 Clusters of Aβ(1-42) peptide with N-terminus and C-terminus colored as Blue and Red respectively..

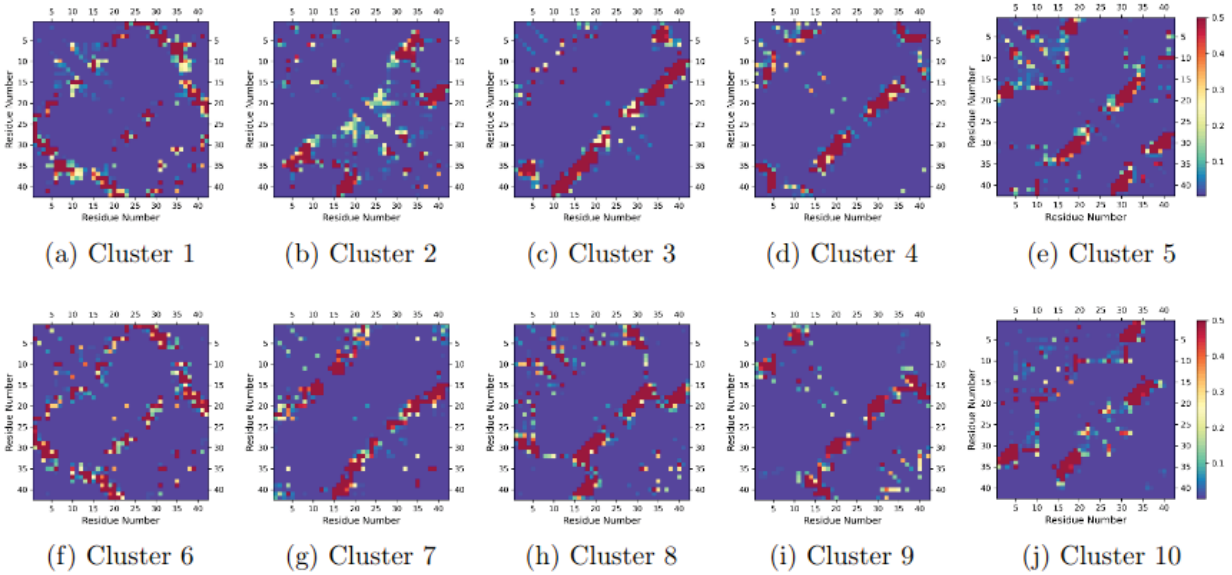

Figure **3-8**: Contact Maps for Top-10 Clusters of Aβ1-42 peptide.

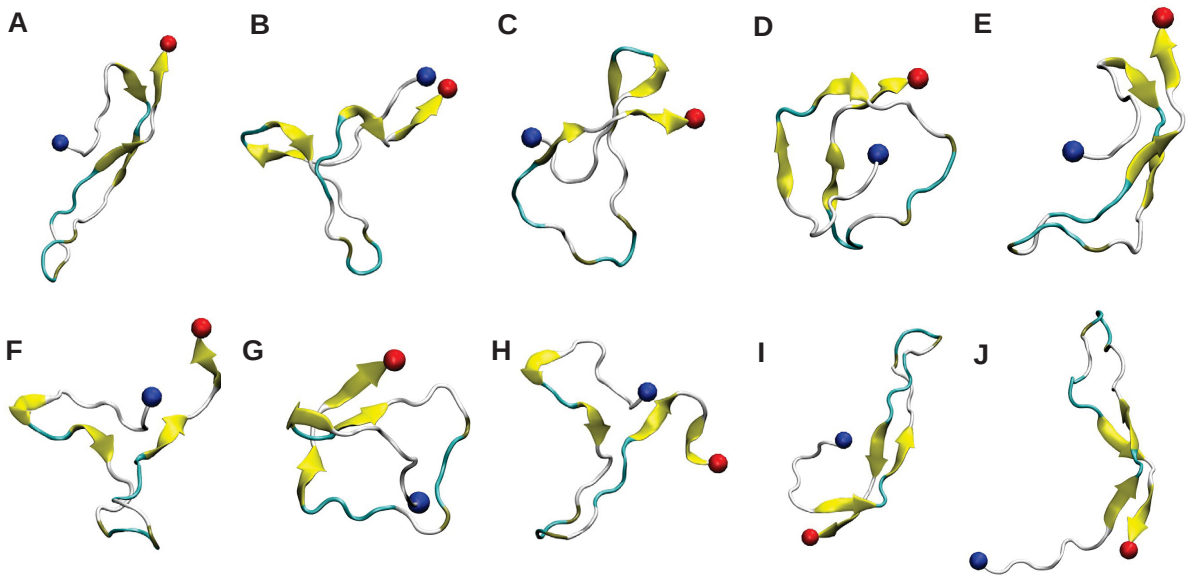

Figure **3-9**: Secondary Structures of Top-10 Clusters of pE-Aβ(3-42) peptide with N-terminus and C-terminus colored as Blue and Red respectively.

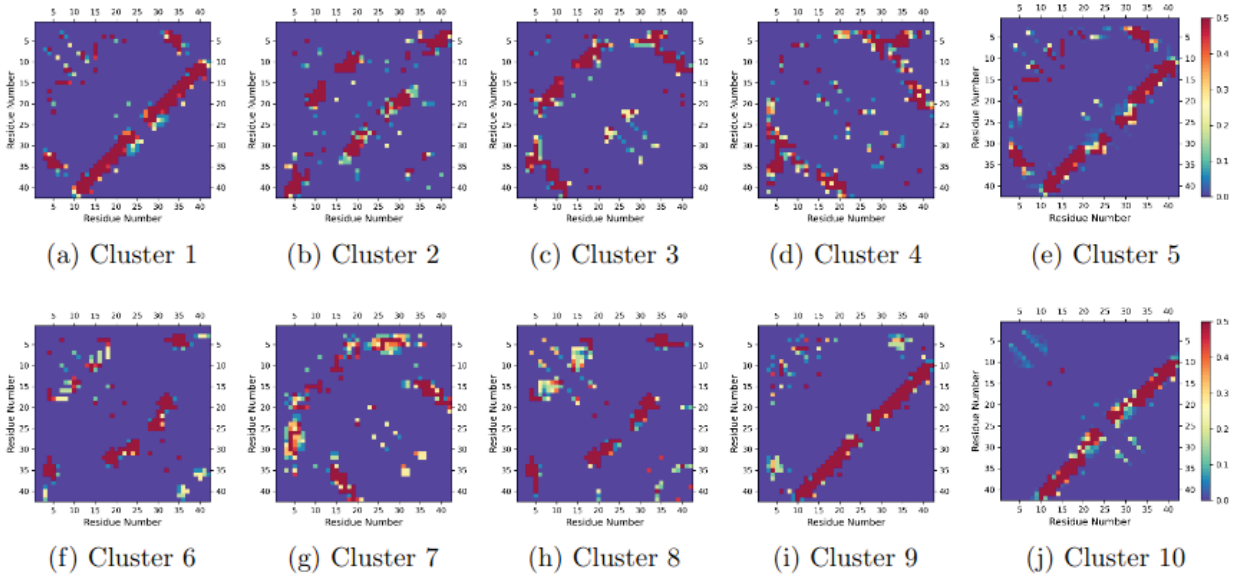

Figure **3-10**: Contact Maps for Top-10 Clusters of pE-Aβ(3-42) peptide.

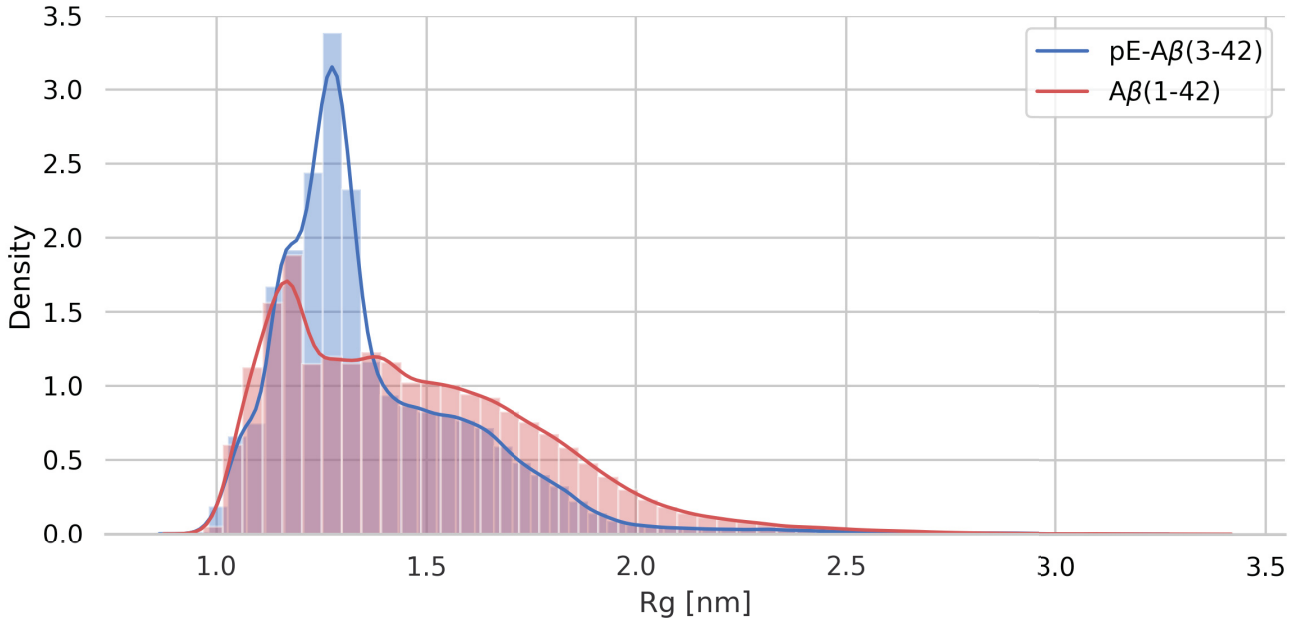

Figure **3-11**: Radius of Gyration (Rg) distribution for pE-Aβ(3-42) and Aβ(1-42).

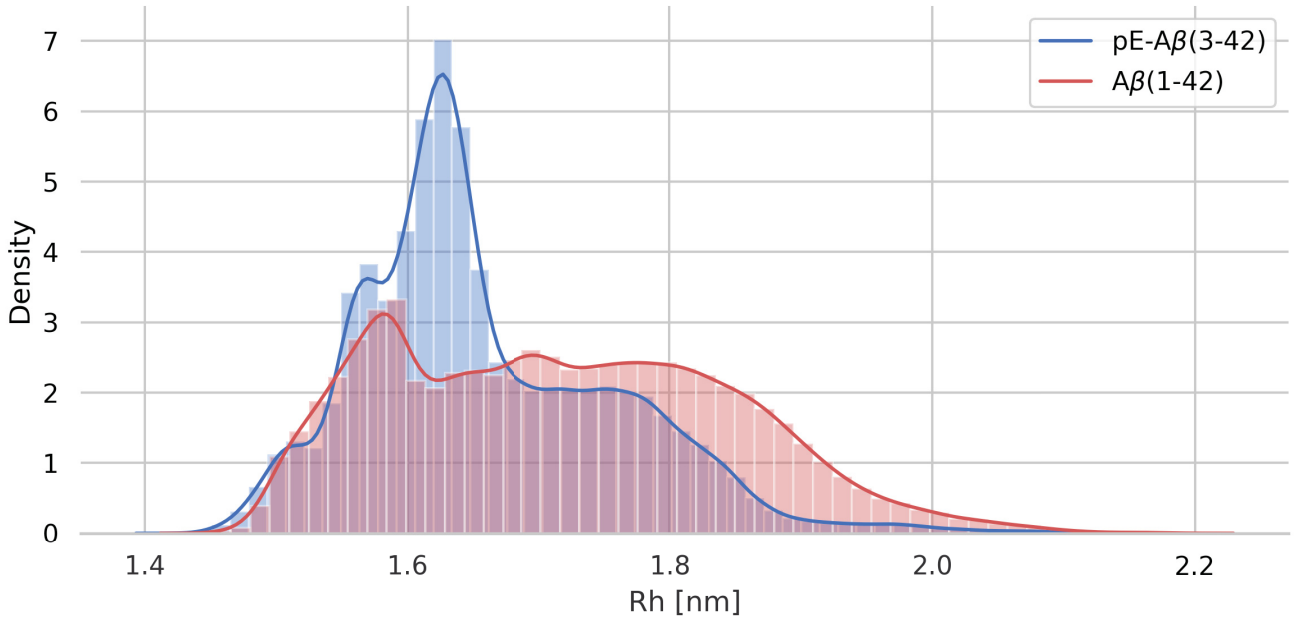

Figure **3-12**: Hydrodynamic Radius (Rh) distribution for Aβ(1-42) and pE-Aβ(3-42).

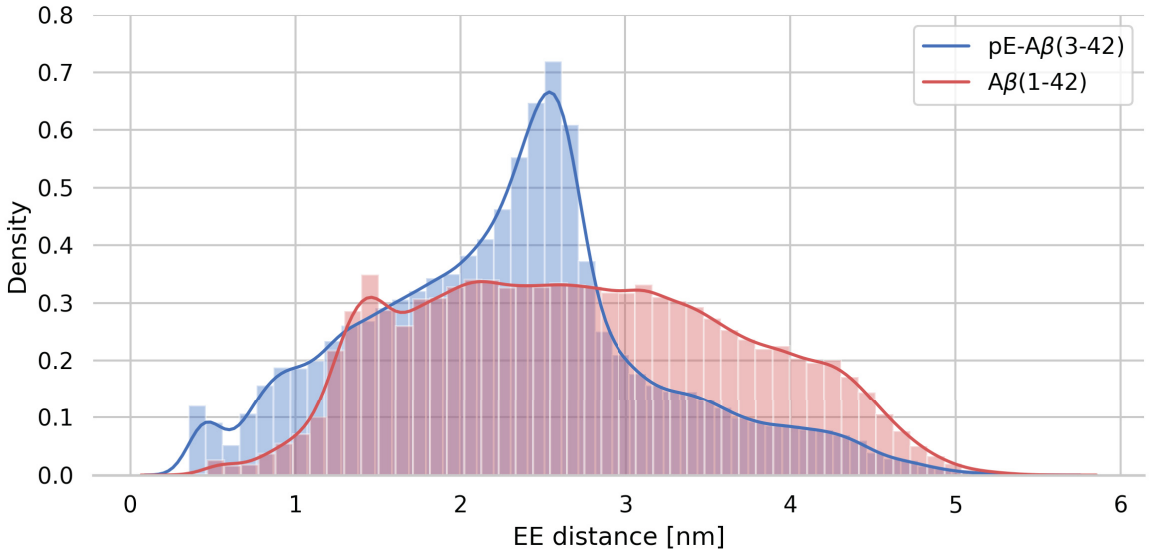

Figure **3-13**: End–to–End (EE) distribution for pE-Aβ(3-42) and Aβ(1-42).

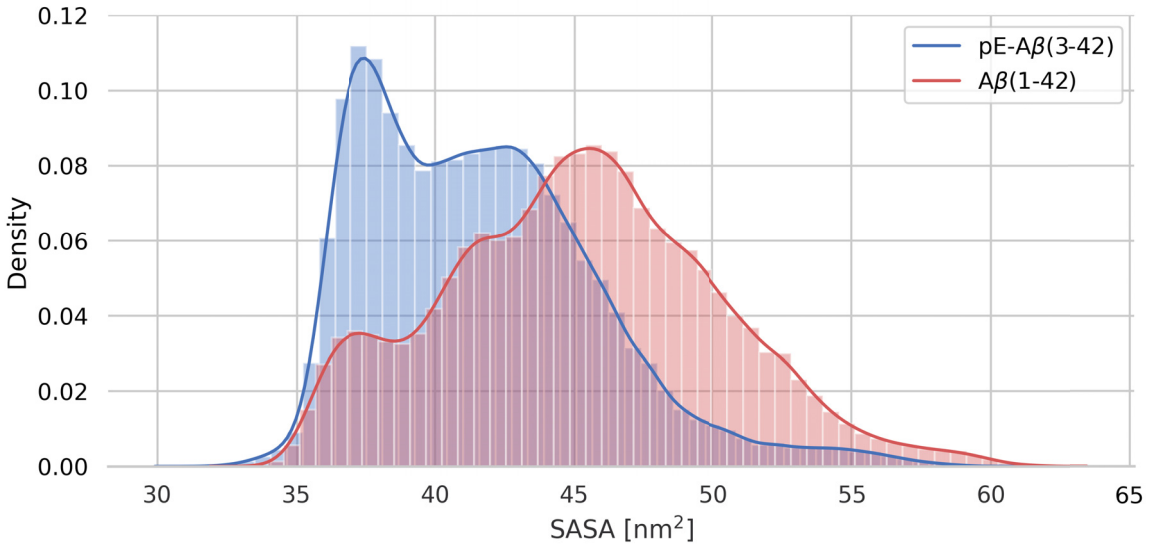

Figure **3-14**: Solvent Accesible Surface Area (SASA) distribution for pE-Aβ(3-42) and Aβ(1-42).

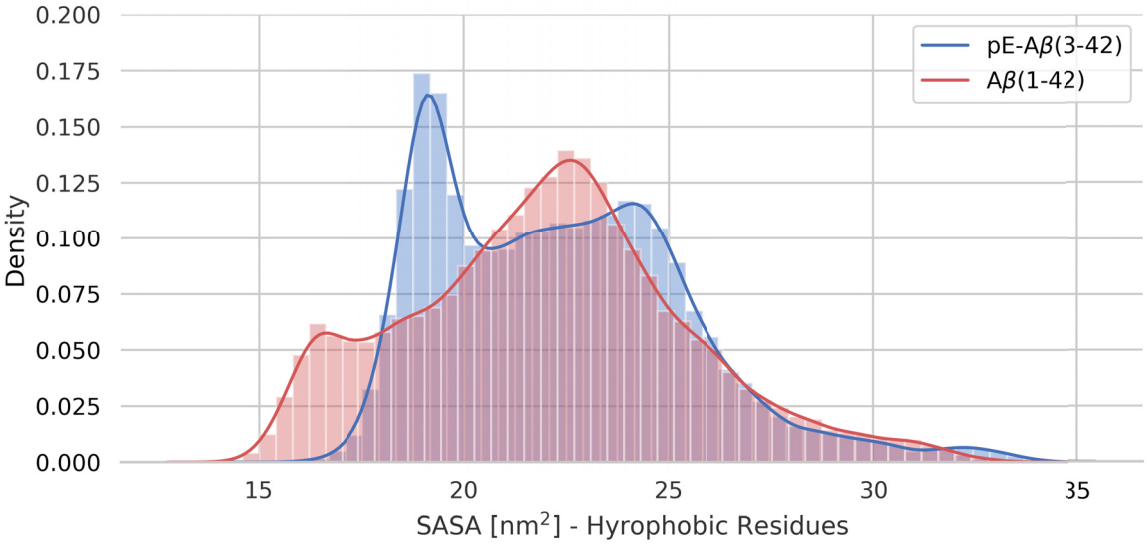

Figure **3-15**: Solvent Accesible Surface Area (SASA) distribution for hydrophobic residues of pE-Aβ(3-42) and Aβ(1-42).

Table **3-2**: Cluster Occurance Probability for Aβ(1-42) and pE-Aβ(3-42)

Cluster#	**Aβ(1-42)**	**pE-Aβ(3-42)**
Cluster 1	6.08 %	18.38 %
Cluster 2	3.38 %	3.86 %
Cluster 3	0.95 %	2.14 %
Cluster 4	0.92 %	1.79 %
Cluster 5	0.91 %	1.36 %
Cluster 6	0.87 %	1.22 %
Cluster 7	0.66 %	1.00 %
Cluster 8	0.56 %	0.96 %
Cluster 9	0.55 %	0.75 %
Cluster 10	0.52 %	0.62 %

4 Pyroglumate-modified Aβ(3-42) peptide monomers bind with higher affinity than Aβ(1-42) monomers to Aβ(1-42) fibrils

4.1 Abstract

Secondary nucleation has been demonstrated to be a dominant pathway for the proliferation of amyloid fibrils and oligomers of the Aβ peptide which represent a major hallmark of the Alzheimer's Disease. Besides the dominant forms of 40/42-residue Aβ peptide, various Aβ isoforms such as the N-terminal truncated pyroglutamate (pE) modified amyloid beta, pE-Aβ(3-42) are also found. Here we employed both surface-based experimental (QCM-D and SPR) and computational (all atom molecular dynamics simulations) biophysical tools to determine the thermodynamic parameters of binding between pE-Aβ(3-42) monomers and Aβ(1-42) fibril surfaces, and compare it with the binding of Aβ(1-42) monomers. Experimentally, we find that the binding of the pE-Aβ(3-42) monomer changes from reversible at pH 8 to irreversible at pH 7.4. pE-Aβ(3-42) monomer binds with higher affinity than Aβ(1-42) monomer to Aβ(1-42) fibril surfaces. Our simulations confirm, a higher affinity of pE-Aβ(3-42) for the Aβ(1-42) single filament fibril surface and show that the two monomeric peptides have different binding modes. Taken together our combined experimental and computational study rationalises the previous observations of Aβ(1-42) fibrils inhibiting pE-Aβ(3-42) aggregation and establish high affinity surface binding as the likely mechanism of inhibition.

4.2 Introduction

Extracellular deposits of insoluble fibrils in the human brain are the major hallmark of the neurodegenerative disorder Alzheimer's Disease (AD) leading to cognitive and memory impairment due to neuronal and synaptic losses. These extracellular plaques are mainly composed of deposits of amyloid-β (Aβ) peptides [136, 229, 12]. The two main Aβ variants found in the brain differ only at the C-terminal two amino acids, with Aβ(1-40) being more abundant than Aβ(1-42) ($\sim$5-10%). In AD patients, however, the extracellular concentration of Aβ(1-42) has been shown to be considerably increased. Although Aβ-40/42 have been found to be the major component of amyloid plaques, several N-terminally and C-terminally truncated or extended Aβ variants have also been found to be present at significant amounts [352, 129] due to different mechanisms of cleavage of the amyloid precursor

protein (AβPP) by α-, β- and γ-secretase enzymes along with post-translational modifications of the Aβ peptides by various enzymes [254, 159]. Even putative therapeutic approaches such as targeting BACE-1 inhibition in order to decrease the amount of Aβ-40/42 have been shown to increase the amount of N-terminally truncated Aβ variant in human brains [330]. Pyroglutamate-modified Aβ (pE-Aβ) peptides are prominent examples of Aβ-variants and result from the post-translational modification of Aβ by the enzyme glutaminyl cyclase (QC). In particular, pE-Aβ(3-42) is the major isoform among these species - representing around 25-50% of the total Aβ content in senile plaques of AD brains [352, 129, 150]. The mechanism of Aβ amyloid fibril formation *in vitro* has been found to consist of a set of microscopic processes, such as primary nucleation, elongation, secondary nucleation and fragmentation of fibrils [297], and there is increasing evidence that the same types of processes are also defining aggregate formation and proliferation *in vivo* [206]. In particular secondary nucleation, the formation of new fibrils on the surface of existing ones, has been found to be the dominant mechanism for rapid proliferation of fibrils besides generation of toxic oligomeric species [66, 317, 310, 59, 318]. The presence of different Aβ-variants have been found to affect each of the crucial microscopic steps involved in the mechanism of fibril formation. Possible scenarios of such interactions are cross-elongation, where monomers of one variant add onto the end of fibrils of another variant, and cross-nucleation where fibrils of one variant provide a surface for the nucleation of monomers of another variant. In order to understand the behaviour of complex mixtures of different Aβ variants, it is therefore important to study the individual variants, as well as their mutual interactions in various scenarios.

Several N-terminally and C-terminally truncated & extended Aβ42 variants have been found to be cross-elongating and cross-nucleating each other [330, 307, 263]. It has also been proposed that the presence of Aβ variants can initiate AD pathology *in vivo* through hampering the clearance mechanism of Aβ(1-42) peptides [204]. Although studies have found that the major Aβ variants which are found in the senile plaques i.e. Aβ(1-40) & Aβ(1-42) can not cross-elongate each other efficiently or form hetero-fibrils, the two peptide species are able to interact with each other at the level of primary nucleation [74]. Interestingly, pE-Aβ(3-42) monomers have been found to be unable to nucleate on the surface of Aβ(1-42) seeds; indeed, the latter have even been found to inhibit the aggregation of the former in a concentration-dependent manner [80]. pE-Aβ(3-42) is found to be stable towards degradation by amino peptidases due to the lack of free amino acid at the N-terminus [39]. As a result of the N-terminal truncation with the loss of two negatively and one positively charged amino acids and the pyroE modification with the formation of a lactam ring at the third residue, significant alterations in the biophysical and biochemical properties of pE-modified Aβ arise. These include increased hydrophobicity, higher β-sheet content through increased driving force for amyloid fibril formation and faster oligomerization rate compared to the unmodified Aβ peptide. These differences are possible explanations for the observed increased toxicity of the pE-Aβ(3-42) peptides [285, 130, 284].

A variety of experimental quantitative kinetic analyses have been performed, starting with the monomers of the major Aβ variants i.e. Aβ(1-40) & Aβ(1-42) in both pure and mixed systems[330, 307, 74]. However, quantitative analysis of one of the key thermodynamic pa-

rameters of amyloid formation, the affinity of monomeric peptide for the fibril surface, has so-far only been performed for the self-interaction of Aβ(1-40) and Aβ(1-42). These experiments were performed using surface plasmon resonance (SPR)[355, 67] and have clearly shed light on important microscopic features of fibril-dependent secondary nucleation. However, they also raise questions about the molecular details of protein absorption, nucleated conversion on the fibril surface, and nuclei detachment, as well as how the synergy of these processes results in accelerated nucleation during the monomer dependent secondary nucleation.

In this context, the use of computational methods will be able to provide insights into the molecular details of these processes, such as the fibril-binding region of the monomer, the monomer-binding site on the fibril, the key nature of interactions that drive the monomer-fibril binding and the conformational preference of the bound monomer. The monomer-fibril interactions have been found to be a critical parameter for the secondary nucleation process of Aβ aggregation; if the interaction is weak, secondary nucleation is inefficient, because not enough peptide is absorbed onto the fibril surface. Conversely, if the interaction is too strong, the peptide remains absorbed on the surface, and is unable to undergo the nucleation step, as predicted by coarse-grained simulations [355]. Recently, atomic level molecular dynamics (MD) simulations of this self-seeding interaction scenario have also been performed using HREMD method in which the Aβ(1-42) monomer-fibril interactions were found to be occurring mainly between the side chain columns of Q15 and K16 of the fibril and E22 and D23 of the monomer, indicating that electrostatic interactions play a major role here; also the free energy calculations suggested that the monomer-fibril binding process is mainly enthalpy driven [40]. Some of the other earlier studies towards mechanistic investigation of Aβ secondary nucleation (self-seeding) involved the interaction of Aβ(1-42) monomer with an Aβ(17-42) fibril segment using atomic simulation with implicit solvent, Aβ(1-40) monomer binding with Aβ(9-40) fibril segment using both umbrella sampling where both studies observed that the free monomer binds to the C-terminal region of the fibril surface and adopts a stretched conformation and the binding free energy was entropy driven [287, 37]. However, a contrasting result was observed when Aβ(1-40) monomer binding with a Aβ(9-40) fibril segment was studied combining a hybrid-resolution PACE model and the temperature-based REMD method, where free monomer was found to be binding with the 16KLVFFAE22 region of the fibril segment and the binding was enthalpy driven, matching the experimental observations [337]. Several cross-seeding aspects of the Aβ peptide have also been investigated using computational methods which include binding of the Aβ(16-22) fragment to Aβ(1-40) fibrils using the PRIME force field consisting of an intermediate-resolution model, REMD simulations of binding between tau fragment of 120-160 amino acid and Aβ(17-42) fibril segment where the conformations of free monomers were found to be following the "bind and reorganize" mechanism, largely consistent with the previous computational studies on self-seeding of Aβ monomer binding to the Aβ fibril surface [54, 253].

Although, to-date, no studies have been performed towards determining the thermodynamic parameters governing the cross-interaction between various other Aβ variants present in human brain and how these might affect the process of amyloid fibril formation overall dom-

inated by the major Aβ variants. In the present study, we aimed at quantifying the thermodynamic parameters of binding and mechanistic evaluation of the binding modes between pE-Aβ(3-42) monomers and Aβ(1-42) fibrils which were previously observed to lead to the inhibition of pE-Aβ(3-42) aggregation [80]. Our approach is a combination of computational methods, i.e. enhanced sampling H-REMD simulations & umbrella sampling methods, along with the experimental biosensing methods quartz crystal microbalance (QCM) and SPR. We compare our results with the thermodynamic parameters for binding for the self-interaction between monomers of Aβ(1-42) with Aβ(1-42) fibrils. We find that both in our computational as well as experimental studies, pE-Aβ(3-42) monomers have a higher affinity for Aβ(1-42) fibrils than monomeric Aβ(1-42) itself.

4.3 Methods

Purification of Aβ(1-42) and pE-Aβ(3-42) samples. Synthetic Aβ(1-42) and pE-Aβ(3-42) samples were bought from BACHEM. The peptides were dissolved in HFIP for ca. 2-3 hours and lyophilized after subsequent aliquoting. The lyophilized samples were directly dissolved in the required buffer.

Preparation of Aβ(1-42) fibrils. The Aβ(1-42) fibrils were prepared before the quartz crystal microbalance with dissipation (QCM-D) experiments in 20 mM phosphate buffer, either at pH 7.4 or pH 8.0, containing 100 μM EDTA and 10% NaN_3, without shaking for ca. 5 hours, a time after which the plateau phase of ThT kinetic curves had been reached. Chemically cleaned QCM-D sensors (with basic piranha solution) were placed in a plasma cleaner to remove any remaining traces of contaminants, then the sensors were incubated with fibril suspensions (of concentration 10 μM, sonicated for 30 seconds with alternative 2 second pulse and 50% amplitude) over night in an environment with humidity-saturated air, and the sensors were rinsed with distilled water and dried with nitrogen before inserting them into the QCM-D instrument.

Quartz crystal microbalance with dissipation (QCM-D) assays. Immediately after insertion into the instrument, the sensors were equilibrated using 20 mM phosphate buffer either pH 7.4 or pH 8.0. Once a stable baseline was reached, the instrument was ready for the measurements. Aβ(1-42) monomers were freshly dissolved in 20 mM phosphate buffer (either pH 7.4 or pH 8.0) at a high concentration (40 μM) and 10 μM of Aβ(1-42) monomer were injected over the sensors functionalized with the fibrils, in order to elongate those and to attain a higher degree of surface coverage of the QCM-D sensors. After a given decrease in resonant frequency of the crystal was reached, indicating the degree of coverage of the sensors with fibrils, the sensor surface was washed with buffer for ca. 1 hour, until a stable baseline of the QCM-D signal was reached. During this wash, monomer loosely attached to the surface of the fibrils was washed away.

Surface plasmon resonance (SPR) assays. Aβ(1-42) fibrils were prepared following the same method as mentioned above prior to the SPR experiments. CM3 SPR sensors containing free carboxylic acid groups on the sensor surface were used and all flow cells were

subsequently activated by EDC / NHS coupling chemistry. Then, sonicated (for 30 seconds with alternative 2 second pulse and 50% amplitude) Aβ(1-42) fibrils were injected over the selected flow cells, keeping a flow cell free of fibrils to be used for control experiments. Immediately, all the flow cells were passivated with 1 M ethanolamine to prevent the subsequent attachment of Aβ(1-42) monomers to the activated sites of the sensor surface. Subsequently the flow cells were kept under a buffer flow using 20 mM phosphate buffer either at pH 7.4 or pH 8.0 at 25°C at a flow rate of 10 μL/min for ca. 15 minutes to attain a stable baseline of the SPR signal. Following the protocols of QCM experiments, 10 μM Aβ(1-42) monomer was injected subsequently for ca. 20-30 minutes at a flow rate of 10 μL/min in 20 mM phosphate buffer at either pH 7.4 or pH 8.0 until a level of SPR signal was obtained that, based on previous studies [355, 67] suggested a high enough coverage of the SPR sensor surface with Aβ(1-42) fibrils. After this initial growth period, the SPR sensors were kept under the respective buffer flow for ca. 2 hours to attain a stable baseline of the SPR signal. Subsequently, Aβ(1-42) monomers were first injected in a concentration-dependent manner over the attached and elongated fibrils in 20 mM phosphate buffer, either at pH 7.4 or pH 8.0, followed by the injection of a pE-Aβ(3-42) monomer concentration series in the respective buffers at 25°C. Equivalent experiments were also performed at 35°C to allow estimation of the thermodynamic parameters of the system.

SPR data analysis. The analysis of the SPR data followed previously established protocols [355]. In brief, the dissociation part of the curve was taken to consist of a linear contribution (sequential dissociation from fibril ends) and an exponentially decreasing contribution (dissociation from independent binding sites on the fibril surfaces). Then, the reverse amplitudes for the exponential decay phase was calculated through linear fit of the linear component of the dissociation signal. Subsequently, the reverse amplitudes of the exponential decay term was plotted as a function of the injected peptide concentration (either Aβ(1-42) or pE-Aβ(3-42)) and the curve was fitted using the Langmuir binding isotherm in order to determine the K_D value for each case. However, this analysis can only be performed in a meaningful manner if the surface-bound monomer detaches to a large extent upon washing, such that it can be assumed that the majority of the binding sites on the fibril surfaces are available for binding in the subsequent monomer injection.

Classical MD simulation - fibril fragment. In order to model an "infinite" Aβ(1-42) fibril we have used the structural model derived by Xiao et al. [339] with PDB ID: 2MXU. Fifteen peptides were arranged in a fibril fragment which was oriented such that the fibril axis is parallel to the Z axis of the simulation box as shown in Fig. **4-5** (c). The periodic boundaries along the Z axis were chosen such that the fibril peptides at the end of the fibril fragment would bind with the next peptide from the periodic copy exactly as the peptides interact within the fragment itself. The N-terminal part of the fibrilar peptides, from D1 to Y10, which is missing in the published structure were added to each peptide as extended chains. After adding water, the system was minimized, pre-equilibrated and then equilibrated for 600 ns with the atoms of the fibril core (G15-A42) restrained in the XY plane but free to move in the Z direction and along the fibril axis. The final state of the fibril fragment at the end of the simulation was used to prepare the system for the next stage, where a free

monomer is allowed to interact with the fibril fragment.

Hamiltonian replica exchange molecular dynamics simulations. The equilibrated fibril fragment was placed in an orthorhombic cell of size (L_x,L_y,L_z) = (6.5,6.5,3.9) nm with similar periodic boundaries in the Z direction chosen to mimic an infinite fibril model. Inside the simulation box, we also added either the full-length pE-Aβ(3-42) or the Aβ(1-42) monomer. As initial conformations for the two monomers we chose the centers of the largest clusters from extensive simulations performed in a previous study (Nath et al. to be submitted, see Chapter 3). Each system was solvated with the modified Charmm36m TIP3P water model with an increased water-protein interaction for a more realistic modelling of intrinsically disordered proteins (IDPs). Thus, the Lennard Jones interaction strength of the hydrogen atoms has been modified from -0.046 kcal/mol to -0.10 kcal/mol as suggested by Huang et al. [137]. The modified force field is labeled Charmm36mW which was also used for performing all simulations. The two systems were neutralized with Na+ ions resulting in 125,040 for the system with the pE-Aβ(3-42) monomer and 137,478 atoms for the system with the Aβ(1-42) monomer.

After energy minimization, position restrained equilibration and a short free equilibration, Hamiltonian replica exchange [56] simulations were performed for each system. Each H-REMD simulation consisted of 20 simulations or replicas running in parallel, with each replica having a different interaction Hamiltonian where non-bonded interactions and dihedral angles are scaled with a factor λ. The biasing coefficients lambda can be expressed as an inverse temperature (1/temperature) correspond to a temperature range between 300 and 500 K and assigned to the replicas according to a geometric distribution. In total we performed two H-REMD simulations with of $\sim$ 1,500 ns/replica for pE-Aβ(1-42) and $\sim$950 ns/replica for Aβ(1-42) amounting to a total simulation time of $\sim$49 μs. All H-REMD simulations were performed on the supercomputer JURECA [160] at the Jülich Supercomputing Centre (JSC).

Umbrella sampling simulations and the potential of mean forces. In order to estimate the binding free energy of the monomers to the fibril surface we applied the umbrella sampling method [314]. For the US simulations, we first selected the last frames from the HREMD simulation trajectories representative for the pE-Aβ(3-42) monomer bound to the hydrophobic fibril side (HPO), i.e. amino acids L34-G38, and for the A*beta*(1-42) monomer bound to the hydrophobic, i.e. amino acids L34-A42, and the hydrophilic side (HPI), i.e. amino acids K16-K28, of the fibril core. From these three initial configurations we performed three steered molecular dynamics simulations where the bound monomers were gradually pulled away from the fibril surface using a harmonic guiding potential with an elastic constant of 1000 kJ mol^{-1} and a pulling speed of 0.01 nm/ps. Thus the distance between the center of mass of the pE-Aβ(3-42) monomer and a selection of atoms from the HPO fibril peptides in contact with the monomer was increased from 1.95 nm to 5.91 nm and 20 configurations within this simulation interval were saved for US. Similarly, the distance between the center of mass of the Aβ(1-42) monomer and a selection of atoms from the HPO and in contact with the monomer was increased from 1.02 nm to 5.9 nm. In the case of the Aβ(1-42)

monomer bound to the HPI fibril side, the distance between the centers of mass was increased from 1.60 nm to 6.46 nm. In both cases 20 configurations were saved for the US simulations. All US simulations were performed via the Centre for Information and Media Technology at Heinrich Heine University Düsseldorf. In total, we performed three sets of US simulations, one for the pE-Aβ(3-42) monomer bound to the fibril surface and two for the Aβ(1-42) monomer. Each window in any of the US simulations was equilibrated for 150 ns. The distance between the center of mass of the monomer and the center of mass of the specific atom selection was restrained to the initial value of each US window via a harmonic guiding potential with an elastic constant of 1000 kJ mol^{-1} throughout the simulations. In all simulations the fibril core (amino acids G15-A42) was restrained from moving in the XY plane but free to move in the Z direction along the fibril axis. The potential of mean forces (PMF) was calculated using the weighted histogram analysis method [177] and was based on the last 100 ns of each simulated window in order to avoid artifacts due to the initial state and to use only the equilibrated part of the trajectory. The ΔG value was calculated by taking the difference between the PMF values at the bound state, i.e. the lowest PMF value, and the unbound state, i.e. the PMF value at a separation distance of 4.5 nm between the monomer and fibril.

Secondary structure, contact maps and clustering from HREMD simulation. Secondary structure propensities per residues were calculated with the program DSSP [167] and the errors with block averaging. For snapshots of the protein structure we used the program Visual Molecular Dynamics (VMD) [139] where the secondary structure is calculated with STRIDE [108]. Contact maps were calculated using the Contact Map Explorer module implemented in Python and considering a contact between two amino acids when any two atoms from the two residues were found at a distance below a cutoff of 0.45 nm. Clustering of structures was performed with the Daura algorithm [84] implemented in Gromacs using the backbone atoms and an RMSD cutoff of 0.4 nm.

MD simulation details. All MD simulations were performed with the software GROMACS 2016.04 [132]. The temperature was kept at 300 K via velocity rescaling with a stochastic term algorithm [55] and a time constant for coupling of 0.1 ps. The pressure coupling was controlled with the Parrinello-Rahman barostat [230, 219] with a time constant of 1 ps. The hydrogen atoms were treated as virtual interaction sites, allowing an integration time step of 4 fs while maintaining energy conservation [102]. The cut-off distance for short range electrostatics and van der Waals interactions was set to 1 nm and the Particle-Mesh Ewald algorithm was used for long range electrostatic interactions.

4.4 Results

4.4.1 Experimental results

Quartz crystal microbalance (QCM-D) assays. The QCM is a powerful tool to study the elongation rates of surface-attached amyloid fibrils in a highly accurate and reproducible manner [52]. When the surface-bound fibrils grow, the associated increase in mass leads

to a measurable decrease in resonant frequency of the QCM sensor. We have shown that the sensitivity of the QCM for the growth of attached fibrils exceeds the sensitivity that is typical for the formation of a homogeneous thin layer [210]. This is due to the trapped water in the growing fibril layer, that adds to the detected dry mass of the fibrils. The ability to incubate a constant ensemble of fibrils repeatedly with different solutions of monomers allows to directly compare the observed rates and hence conclude in what way a given change in amino acid sequence or solution conditions affects the fibril growth rate [51]. After insertion of the QCM sensor with surface-attached fibrils into the instrument, the amyloid fibril elongation experiments were divided into the following steps: (1) buffer stabilization of the system, (2) injection of Aβ(1-42) monomers, (3) termination of fibril elongation by buffer injection, (4) injection of pE-Aβ-(3-42) monomers and lastly (5) renewed buffer injection, as depicted in Fig. **4-1**.

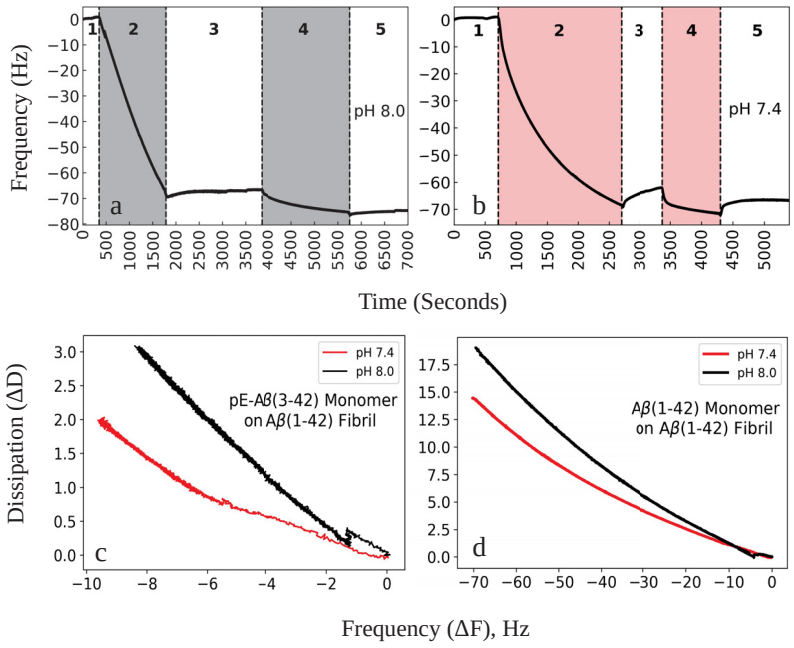

Figure **4-1**: QCM experiments of Aβ(1-42) fibrils incubated with soluble Aβ(1-42) and pE-Aβ(3-42). **(a)** Injection of 7.5 μM pE-Aβ(3-42) monomer over a fibril coated QCM sensor (4) at pH 7.4 after a previous incubation with 7.5 μM Aβ(1-42) monomer at pH 7.4 (2). **(b)** Injection of 7.5 μM pE-Aβ(3-42) monomer over fibril coated QCM sensor (4) at pH 8.0 after a previous incubation with 7.5 μM Aβ(1-42) monomer at pH 8.0 (2). **(c)** Dissipation against frequency plot for the injections of 7.5 μM pE-Aβ(3-42) monomer at pH 7.4 and pH 8.0, **(d)** Dissipation against frequency plot for the injections of 7.5 μM Aβ(1-42) monomer at pH 7.4 and pH 8.0

Overall the process can be summarised as follows. First the attached Aβ(1-42) fibrils on the QCM sensor surface were elongated with Aβ(1-42) monomer, either in pH 7.4 (steps 1-3 of Fig. **4-1** (a)) or in pH 8.0 (steps 1-3 of Fig. **4-1** (b)), where the decrease in resonant fre-

quency indicates significant growth of the fibrils. These two pH values were chosen because many of the groundbreaking mechanistic insights into the amyloid fibril formation of the Aβ peptide were obtained from experiments at pH 8 [66, 67], whereas pH 7.4 is probably more physiologically relevant. We decided to investigate whether such a small change in pH would influence the behaviour of the Aβ systems under study.

The pE-Aβ(3-42) monomers were injected over the fibrils either at pH 7.4 (steps 4-5 of figure **4-1** (a)) or pH 8.0 (steps 4-5 of Fig. **4-1** (b)) which shows different patterns of frequency shift in the QCM signal. At both pH values, the injection of Aβ(1-42) monomer (7.5 μM) leads to a much more significant frequency response compared to the injection of the same concentration of pE-Aβ(3-42) monomers, suggesting that the fibrils that consist of Aβ(1-42) monomers are more easily elongated by the same monomer types than by pE-Aβ(3-42) monomers. The main difference between pH 7.4 and pH 8 is that at pH 8, a constant linear decrease in frequency is observed upon Aβ(1-42) monomer injection, whereas at pH 7.4, the decrease in resonant frequency appears to level off. At pH 7.4, a larger fraction of the observed decrease in frequency upon monomer injection is reversible upon washing the flow cell with buffer, i.e. this pH condition leads to a larger fraction of reversible monomer attachment. Fibril growth is usually less reversible compared to attachment of monomer to the fibril surface [355]. The latter is also compatible with a decreasing rate of attachment, due to the progressive saturation of the binding sites on the fibril surface [355]. The QCM data therefore provides initial evidence that at the slightly lower pH of 7.4, the relative contribution of binding to fibril surfaces is higher than at pH 8.

This conclusion receives additional support when considering plots of dissipation against frequency shift (Fig. **4-1** (c) and (d)). For both types of peptide monomer, we observe less increase in dissipation for a given frequency shift at pH 7.4 compared to pH 8. When comparing the attachment of a monomer to a fibril end vs. attachment to the fibril surface, we can expect that these two types of monomer addition to the fibril lead to a different change in resonant frequency and dissipation. This is because the elongation of a fibril and the absorption of a monomer to a fibril surface contribute differently to the overall roughness of the surface, and hence to the trapping of water inside the surface-bound layer. We can therefore conclude from the QCM experiments that the mode of interaction of Aβ monomer with Aβ(1-42) fibrils depends both on the type of monomer (Aβ(1-42) vs. pE-Aβ(3-42)), as well as the pH of the solution. Initial evidence suggests that what changes is the relative amount of elongation and fibril surface binding. In order to investigate this difference in behaviour further, we performed surface plasmon resonance (SPR) experiments, which allow to quantify the amounts of attached monomer more accurately than QCM-D.

SPR experiments of monomer-fibril binding. It has been demonstrated that surface plasmon resonance (SPR) measurements allow to directly measure the interactions between monomers & amyloid fibril surfaces as a function of monomer concentration and temperature, thus providing insight into the initial events in the secondary nucleation step [355, 67]. Here we employed SPR measurements to study the interactions of pE-Aβ(3-42) monomers with the Aβ(1-42) fibril surface and compared it to the self-interaction of Aβ(1-42) monomers

to the surfaces of fibrils formed by the same peptide. The affinity of Aβ(1-42) monomers to its own fibril surfaces has previously been quantified at pH 8 and different temperatures [67]. In this study we performed similar experiments at 25°C and 35°C for both Aβ(1-42) and pE-Aβ(3-42). In agreement with previous observations [355, 67], a brief incubation of the surface-bound Aβ(1-42) fibrils with Aβ(1-42) monomers, followed by an extensive buffer wash leads to a bi-phasic dissociation signal (Fig. **4-2** (b)), a combination of a rapid exponential dissociation (peptide dissociating from the fibril surface) and a slow linear dissociation (peptide dissociating from the fibril ends) [47]. The amplitude of the exponential binding component as a function of peptide concentration yields a Langmuir binding isotherm [355].

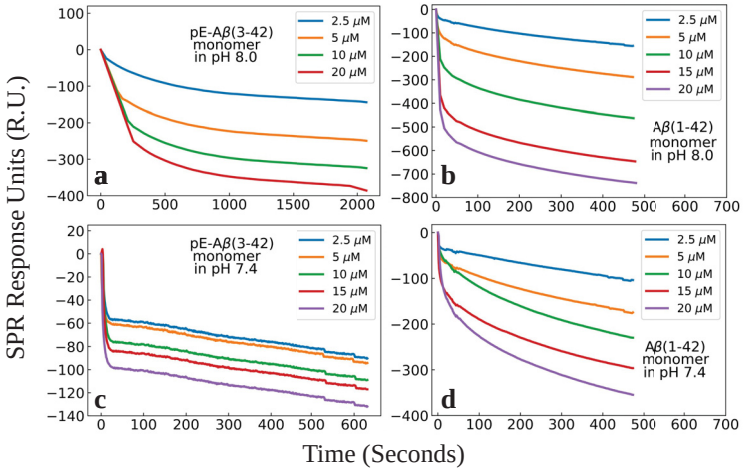

Figure **4-2**: SPR dissociation experiments suggest that pE-Aβ(3-42) monomer attaches irreversibly to Aβ(1-42) fibril surfaces unlikely to the Aβ(1-42) monomers thereby affecting the course of secondary nucleation of Aβ(1-42) fibrils; but at pH 8.0 it binds reversibly with the Aβ(1-42) fibril surface. The SPR dissociation signals are depicted for the following systems: **(a)** injection of Aβ(1-42) monomers over Aβ(1-42) fibril surface at pH 7.4, **(b)** injection of Aβ(1-42) monomers over Aβ(1-42) fibril surface at pH 8.0, **(c)** injection of pE-Aβ(3-42) monomers over Aβ(1-42) fibril surface at pH 7.4 and **(d)** injection of pE-Aβ(3-42) monomers over Aβ(1-42) fibril surface at pH 8.0; for direct comparison pE-Aβ(3-42) monomers binding with Aβ(1-42) fibrils surface with Aβ(1-42) monomers at different pH medium.

The behavior observed for pE-Aβ(3-42) at pH 8 is qualitatively similar to that of Aβ(1-42) (Fig. **4-2** (d)) and we therefore performed full concentration dependencies with both types of monomeric peptides at 25°C and 35°C, allowing us to determine the K_D values. For Aβ(1-42) monomer binding to the Aβ(1-42) fibril surface, we obtained K_D values of 13.8 μM at 25°C and 24.6 μM at 35°C. These values are in good agreement with those previously reported for the same peptide system [67]. Notably, the previously reported values were obtained with recombinantly produced Aβ(1-42) peptide and the experiments in the present study were obtained with synthetic peptide. The weakening of the binding with increasing temperature is a signature of the enthalpically favourable nature of the interaction between the peptide and the fibril surface [67]. In the case of pE-Aβ(3-42) monomers interacting

with the Aβ(1-42) fibril surface the K_D value was found to be 4.6 μM at 25°C and 12.6 μM at 35°C. This results suggests that the interaction of pE-Aβ(3-42) with the surface Aβ(1-42) is characterised by a higher affinity than the equivalent one of the Aβ(1-42) peptide, and is also enthalpically favourable.

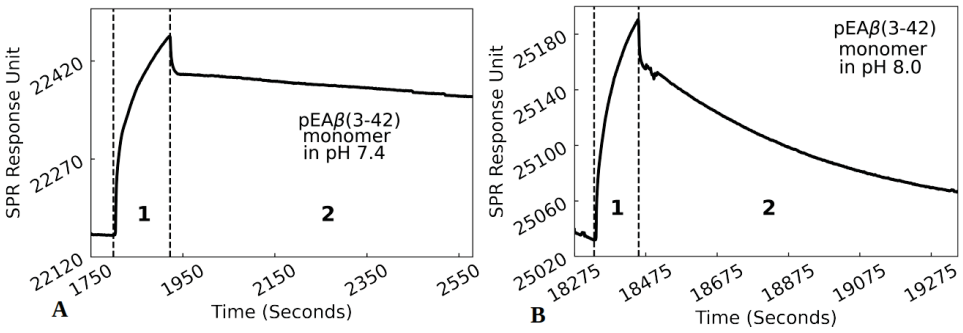

Figure **4-3**: Comparison of raw data from SPR experiments distinguishing the nature of dissociation signal of binding between pE-Aβ(3-42) monomers and Aβ(1-42) fibril surface at (A) pH 7.4 and (B) pH 8.0 conditions at 25°C

Next, we performed equivalent experiments at the physiologically relevant condition of pH 7.4. In the case of Aβ(1-42), we observed a much slower dissociation upon washing with buffer (Fig. **4-2** (a), compared to the equivalent experiment at pH 8, but overall the same bi-phasic behaviour as in the case of pH 8 was observed. This allowed a determination of the binding affinity (11.7 μM), similar to that at pH 8. If pE-Aβ(3-42) monomers are injected at pH 7.4, however, the observed behaviour is qualitatively different. After the injection, the peptide was found to be almost irreversibly attached, with very little of it removable upon washing with buffer. SPR data (blank corrected) of a full injection of pE-Aβ(3-42) at pH 8 and pH 7.4 is shown in Fig. **4-3**. A pre-requisite for the ability to determine a binding affinity

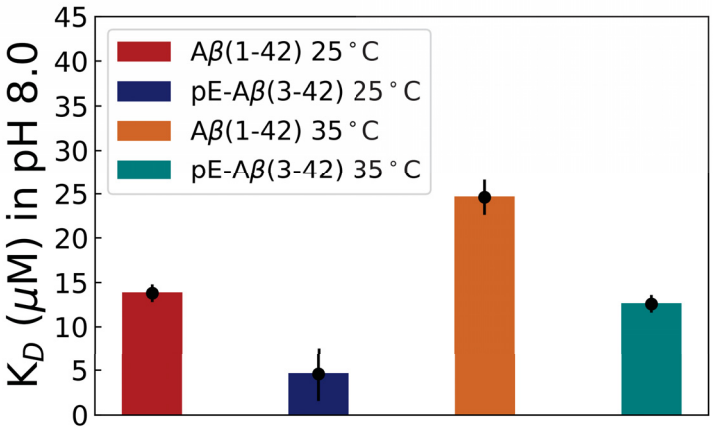

Figure **4-4**: Comparison of K_D values of binding between pE-Aβ(3-42) monomers and Aβ(1-42) monomers with Aβ(1-42) fibril surface at pH 8.0 condition at 25°C and 35°C.

from such experiments is that upon washing of the surface with buffer, the SPR signal returns to a similar level as before the peptide injections, indicating that all the fibril surface-bound

peptide is washed away, and that only the newly elongated fibril parts remain, which dissociate more slowly. This behaviour allows to directly compare the binding signal obtained from injection of different peptide concentrations. At pH 7.4, we found that even after prolonged washing, this was not the case for pE-Aβ(3-42), and therefore accurate K_D determination was not possible for this scenario. Qualitatively, the data suggests that the dissociation rate of pE-Aβ(3-42) from the fibril surface is slower by more than an order of magnitude, whereas no significant difference in binding kinetics can be noticed (Fig. **4-3**). This in turn suggests that the binding affinity of pE-Aβ(3-42) for Aβ(1-42) fibril surfaces an order of magnitude, or more, higher than the self-affinity of Aβ(1-42) monomer to Aβ(1-42) fibrils. The K_D values for the monomer-fibril interaction can be directly converted into the standard Gibbs free energy (ΔG^o), yielding -30.5 kJ mol^{-1} for pE-Aβ(3-42) and -27.5 kJ mol^{-1} for Aβ(1-42) at pH 8, with the latter matching closely with that reported previously [67].

4.4.2 Computational results

Choice of fibril structure. During the past years, experimental methods for identifying complex bio-molecular structures, especially Cryo-EM, have advanced significantly and led to multiple high resolution structures of amyloid fibrils [332]. For this study we have chosen the Aβ fibril model with PDB ID: 2MXU determined by solid-state nuclear magnetic resonance (NMR) [339]. This is a single filament structure with high resolution for amino acid E11 to A42 and a cross section is shown in Fig. **4-5** (a). The rest of the N-terminus is very flexible and was not resolved in the original NMR structure. Even though it is lacking a second

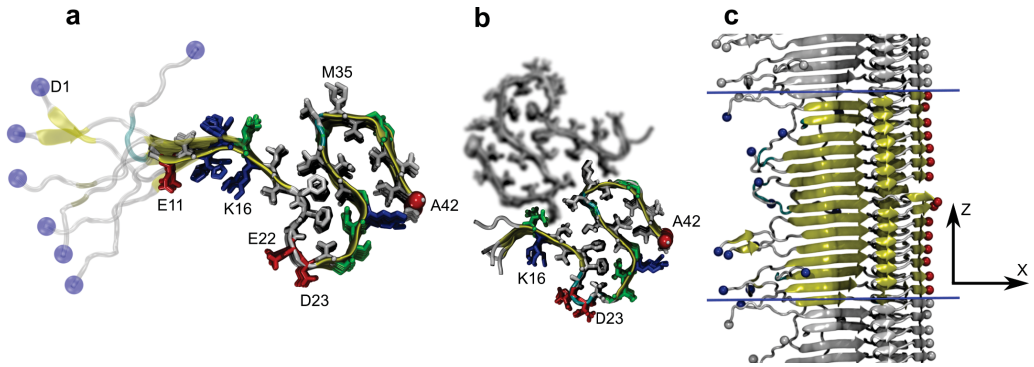

Figure **4-5**: Fibril models. a) S-shape fibril model identified by Xiao et al. and used in the current study [339]. b) Double filament fibril model identified by Colvin et al. [69]. c) Periodic unit cell which allows the infinit replication of the fibril fragment along the Z-axis.

interfacing filament, as in the fibril model published by Colvin et al. [69] and shown in Fig. **4-5** (b), it does have several advantages when studying monomer attachment to fibrils. First of all, it exposes to the solvent and to the incoming monomer both the hydrophobic fibril region, otherwise hidden in the double filament model, and the opposite fibril side which contains many hydrophilic amino acids. Thus, using this model, one may efficiently investigate mechanisms that may lead either to the growth of a second fibril filament on the existing one and enabled by the hydrophobic fibril surface, or to the generation of toxic oligomers and formation of new fibrils enabled by the hydrophilic surface. Furthermore,

while at the end of an Aβ fibril formation reaction, mostly mature, double filament fibrils are found, single strand (proto-)filaments are also observed at intermediate stages. Another advantage is that, in MD simulations, one can model the single filament as an infinite fibril by carefully choosing periodic boundary conditions as in the current study, see Fig. **4-5** (c). This is not straightforward when a second filament is present, due to different pitch angles of the two filaments with respect to the fibril axis, and other approaches must be used which could lead either to simulations not modeling a bulk system anymore or to the use of small fibrilar fragments which are more similar to oligomers than fibrils. The reduced size of the simulated system when using a single filament also allows for computationally intensive sampling methods, such as H-REMD and US, to be efficiently used. In our setup, the N-terminal amino acids missing in the original structure were added as elongated amino acid chains to the rest of the fibril peptides, shown in Fig. **4-5** (a),(c) and a fibril fragment composed of 15 peptides was equilibrated for several hundred ns before the actual H-REMD simulations.

pE-Aβ(3-42) monomer binds exclusively to the hydrophobic side of the Aβ(1-42) fibril surface. To investigate the interaction between the monomers of pE-Aβ(3-42) and Aβ(1-42) peptides with fibril models derived from experimental studies, we have performed two H-REMD simulations for the two peptides. In each simulation a monomer was allowed to freely move in a simulation box which has a 15 peptide long fibril structure located in the center of the XY and with the fibril axis extending along the Z direction to infinity, by a suitable choice of periodic boundaries. A qualitative overview of the simulations indicates that the two peptides have preferred specific locations for binding on the fibril. The trend during the simulation is that, in both cases, the peptides start moving throughout the entire simulation box and interacting weakly with the fibrils until they find a specific region on the fibril where they bind to and remain until the end of the simulations. This can be observed

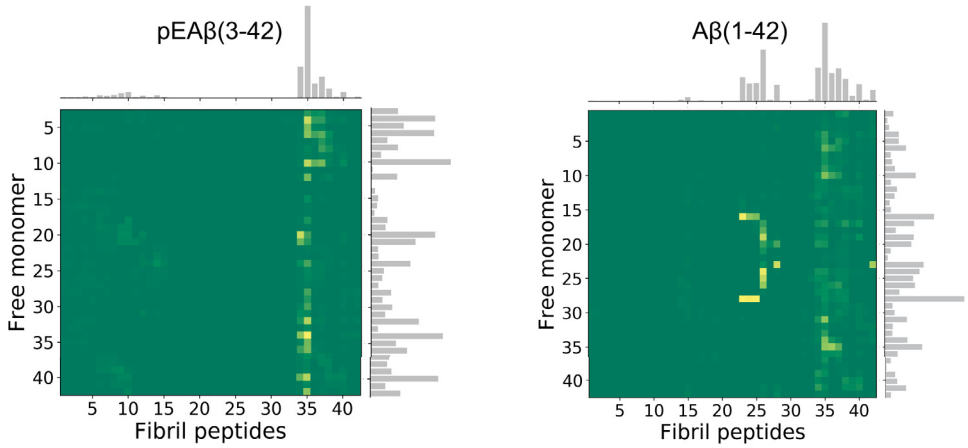

Figure **4-6**: Contact map plot indicating the probability of residue interacting between the free monomer and the Aβ(1-42) fibril surface for the case when (a) pE-Aβ(3-42) is the free monomer and (b) Aβ(1-42) is the free monomer.

in Fig. **4-18** where the projection of the free monomer atoms on the XY plane of the simulation box is displayed. From this figure it is evident that the pE-Aβ(3-42) monomer

prefers to bind to a particular side of the fibril core which contains a very hydrophobic section of the C-terminus of Aβ(1-42). In contrast, the Aβ(1-42) free monomer, displays a bimodal type of binding which includes the hydrophobic side of the fibril core, as in the case of the pE-Aβ(3-42) monomer, and the opposite side of the fibril core which contains several hydrophilic and charged amino acids. Once bound to these locations, both monomers experience mostly internal structural changes without considerable motion to other fibril regions. Thus, in the detailed analysis below we focus mainly on the section of the H-REMD trajectory where the monomers are already bound to the specific locations on the fibril. This amounts to approximately 530 ns for Aβ(1-42). For consistency we have chosen the same trajectory length for pE-Aβ(3-42) as well, despite spending more time at the same binding site. A detailed analysis of the molecular interactions between the monomers and the fibril is presented below by means of contact map analysis.

Binding to fibrils leads to increased β sheet propensity in pE-Aβ(3-42) but decreased in Aβ(1-42) monomers. Contact maps are excellent tools for investigating specific molecular interactions between two proteins. Fig. **4-6** shows the contact maps for the pE-Aβ(3-42) and Aβ(1-42) monomers bound to the Aβ(1-42) fibril surface. This highlights the distinct binding behaviour of the two Aβ isoforms.

Binding of pE-Aβ(3-42). The pE-Aβ(3-42) monomer was found to bind predominantly to the C-terminal region (L34-G38) of the Aβ(1-42) fibril, with M35 from the fibril having the strongest contact frequency. Both the N-, i.e. pE3-Y10, and C-terminal, i.e. I32-V40, regions of the pE-Aβ(3-42) free monomer, as well as F20, A21 and V24 take part in the binding interaction with the Aβ(1-42) fibril surface. This mode of interaction underlines the importance of hydrophobic contacts, given that pE-Aβ(3-42) is more hydrophobic than Aβ(1-42), with fewer charged amino acids at the N-terminus. In addition to strongly binding at the C-terminus of the fibril, the pE-Aβ(3-42) also interacts weakly with part of the N-terminus. These interactions can be identified in the contact map figure between amino acids in the central hydrophobic cluster and the C-terminus of the free monomer, and region H6-H14 from the fibril peptides. This binding mode is exemplified in Fig. **4-8** (a), where a representative state of the system is shown. On top of Fig. **4-8** (a), the monomer is displayed in interaction with the hydrophobic side and the N-terminus of the fibril. From a different angle, shown on the bottom of Fig. **4-8** (a), the bound monomer is observed in contact with the fibril surface in a conformation with elongated geometry. One should note the presence of β-sheet conformations which are not present for the binding modes of Aβ(1-42) monomer. This indicates that, upon binding, pE-Aβ(3-42) preserves its high β-sheet content structure. This is confirmed by the secondary structure propensity per amino acid shown in Fig. **4-7**, where, for 10 amino acids of pE-Aβ(3-42), the propensities increased to above 90% compared to the simulation of a single monomer in the absence of fibrils where the largest propensity was around 70%.

Binding of Aβ(1-42). The Aβ(1-42) monomer has been found to bind on two regions of the Aβ(1-42) fibril surface, located on opposite sides of the fibril core (see Fig. **4-18**). The first contains hydrophobic region L34-A42 at the C-terminus and similar to the binding site

of pE-Aβ(3-42). Most of the amino acids in the free monomer interact with this region, but Y10, D23, I31 and L34-M35 have slightly higher interaction frequencies than the rest. This binding mode is also shown in Fig. **4-8** (b), where the monomer adopts a random coil structure with the N-terminus in contact with the negatively charged C-terminus and the rest of the peptide towards the inner part of the fibril. The second binding site, as identified in the contact map on the right in Fig. **4-6**, contains the highly hydrophilic region E22-K28 of the fibril. In this case, the amino acids from the free monomer which make contact with the fibril are restricted to K16-K28. The representative state corresponding to this binding mode and displayed in Fig. **4-8** (b) reveals a considerably different type of monomer conformation. Whereas in the other binding modes of Aβ(1-42) and pE-Aβ(3-42) the monomer was basically spread along the fibril surface, in this case it has its termini completely immersed in the solvent and only the region K16-K28 is in contact with the fibril. This also implicates that the center of mass of the monomer is further away from the fibril surface. Regarding the β-sheet content upon binding, as discussed in the previous paragraph, the Aβ(1-42) monomer suffers a reduction in number of amino acids with extended conformation. This can be seen in Fig. **4-7** where, for most amino acids, there is considerable reduction in β-sheet propensity to below 20% upon binding.

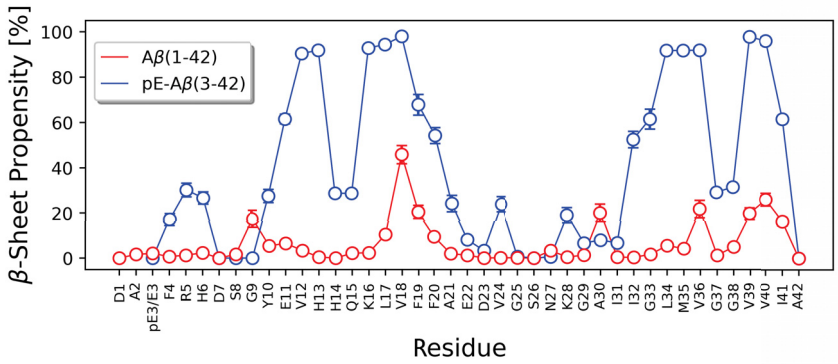

Figure **4-7**: Propensity of β-sheet content in the bound monomers of pE-Aβ(3-42) (blue) and Aβ(1-42) (red). The quantities were calculated only for the trajectory when the monomers were bound to the fibrils.

Considering that both alloforms had very similar β-sheet propensity values in the absence of fibrils, the change in this quantity when the fibril is added to the system is quite dramatic. Furthermore, the fact that both pE-Aβ(3-42) and Aβ(1-42) bind to the same hydrophobic C-terminal region of the fibril leads to the conclusion that the change in secondary structure is a very important effect of the fibril surface on the monomer structure. This observation most likely has important implications for the very different aggregation pathways of the two peptides, especially regarding the secondary nucleation process involved.

pE-Aβ(3-42) monomers bind to the Aβ fibrils with similar affinity as Aβ(1-42) but for different reasons. The binding free energy is a crucial quantity which ultimately defines the secondary nucleation regime of the monomer-fibril system [355]. Importantly, it can be estimated by both experimental and computational methods thus establishing a very sought

for link between the two. Here, we have employed the umbrella sampling (US) simulation

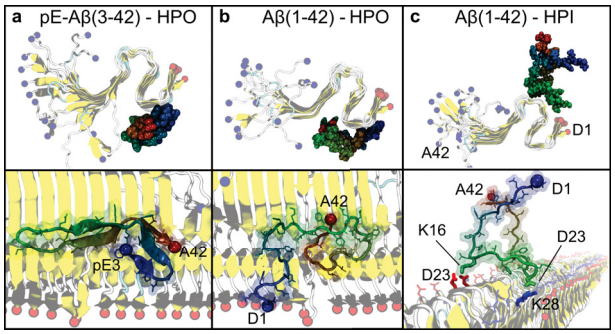

Figure **4-8**: Top clusters for free monomer binding with Aβ(1-42) fibril surface, (a) pE-Aβ(3-42) free monomer binding the hydrophobic side of the fibril, (b) Aβ(1-42) binding the hydrophobic side of the fibril surface and (c) Aβ(1-42) monomer binding the hydrophilic side of the fibril surface.

method for investigating the standard Gibbs free energy (ΔG^o) for the observed main binding modes of the free monomers with the fibril surface. The potential of mean forces (PMF) was calculated for three cases corresponding to one binding mode of pE-Aβ(3-42) monomer on the hydrophobic fibril side, and two binding modes of the Aβ(1-42) monomer on the hydrophobic and hydrophilic fibril sides. For all cases, we used as initial configuration the latest state observed during the H-REMD simulation and corresponding to each binding mode.

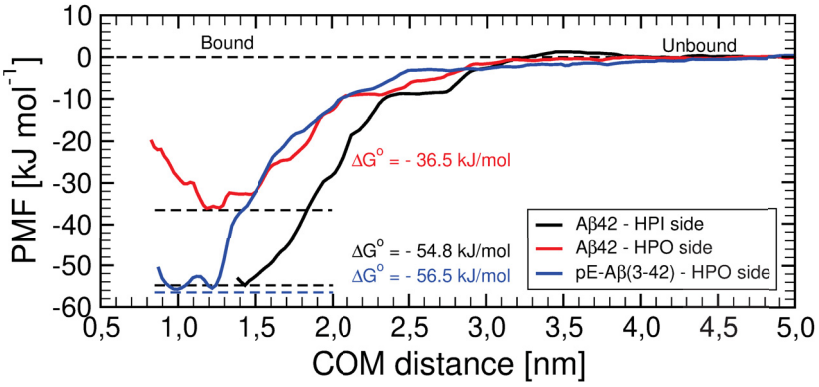

Figure **4-9**: Free energy profiles (PMF) in the dependence of fibril-monomer COM separation, perpendicular to the infinite fibril filament axis, indicated for pE-Aβ(3-42) monomer binding the HPO side of the fibril surface (blue), Aβ(1-42) monomer binding the HPO side of the fibril surface (Red) and Aβ(1-42) monomer binding the HPI side of the fibril surface (black).

The PMF was calculated along the separation distance between the center of mass of the monomer and the center of mass of a group of atoms from the fibril that the monomer was in contact with in the initial state. The PMF curves as functions of the separation distance are shown in Fig. **4-9**. While the unbound state is observed for all peptides at

distances above 4.5 nm, the bound state has different characteristics for different binding modes. Thus, pE-Aβ(3-42) has the lowest PMF value around a value of 1 nm of the reaction coordinate, below that for the Aβ(1-42) monomer. This indicates that the center of mass of the peptide is closer to the fibril surface than for Aβ42 and suggests a very tight binding, most likely enabled by the strong hydrophobic interactions between the monomer and the fibril surface. pE-Aβ(3-42) also has the largest difference between the PMF values in the bound and unbound states, corresponding to a ΔG^o value of -56.5 kJ mol^{-1}. The binding mode of Aβ(1-42) monomer on the hydrophobic side of the fibril core resulted in a PMF with the lowest value at a separation distance larger than that of pE-Aβ(3-42) by about 0.2 nm. In addition, the calculated ΔG^o value for this mode was of -36.5 kJ mol^{-1}, thus indicating a much weaker binding than pE-Aβ(3-42) for the the same fibril region. This difference could be related to the lack of β-sheet secondary structure in the bound Aβ(1-42) monomer as described in the sections above. The binding to the hydrophilic fibril side, in contrast, led to a binding free energy value of -54.8 kJ mol^{-1}, much closer to the value observed for pE-Aβ(3-42). This result is very intriguing, given the fewer contacts involved in this binding mode as observed during the H-REMD analysis. Nevertheless, these contacts were confirmed in Fig. **4-19** as strong hydrogen bonds as well as salt bridges between amino acids K16 and D23 from the monomer and D23 and K28 from the fibril, respectively. The occurrence of these strong non-covalent bonds could indeed explain the large binding free energy calculated. In addition, the lowest PMF value was in this case obtained for the largest value of the separation distance, close to 1.4 nm. This is most likely due to the fact that, during this binding mode, a significant part of the monomer sequence was extending away from the fibril surface as seen in Fig. **4-8**. In the discussion section we provide a detailed comparison of the binding free energies from this studies with reported values from both experimental and computational studies.

4.5 Discussions

Using the dissociation constant values obtained from SPR experiments, we calculated corresponding standard Gibbs free energies (ΔG^o) of -30.7 kJ mol^{-1} for pE-Aβ(3-42) and of -27.7 kJ mol^{-1} for Aβ(1-42) at pH of 8, also included in Table **4-1**. This indicates that the pyroglutamate monomer binds slightly stronger to the fibril surface than the 42 amino acid peptide. Computationally we have observed a large variation in values, depending on the side of the fibril where the binding takes place. pE-Aβ(1-42) binds exclusively to the hydrophobic side of the fibril core with a binding free energy almost twice as large as the experimental value calculated in our study. Interestingly, reported binding free energies of Aβ(1-40) monomers interacting with Aβ(1-40) fibril surface show a similar trend (Table **4-1**), with values obtained from simulations [288], when monomers are binding to the hydrophobic side of the fibril, twice as large as values determined experimentally [299].

One should note that the reported binding free energy of Aβ(1-40) monomers is very similar to that of Aβ(1-42) monomers as discussed below. In the case of Aβ(1-42) monomers, the binding free energies are very similar when a pH of 7.4 (ΔG^o = -28.1 kJ mol^{-1}) or 8 was used. A previous experimental study [67] revealed a value of -27 kJ mol^{-1} for the Aβ(1-42)

monomer, in excellent agreement with our experimental results. The binding free energies calculated from simulations are very diverse, depending on the binding site. When binding to the C-terminus region, similarly to pE-Aβ(3-42), the Aβ(1-42) monomer experiences a free energy difference of -36 kJ mol^{-1}

Table **4-1**: Comparison of Standard Gibbs Free Energy (ΔG^o) of Aβ(1-42) monomer-fibril binding. All values are in units of kJ/mol and refer to a standard state of 1 M monomer and T = 300 K. HPO stands for hydrophobic fibril side and HPI for hydrophilic fibril side.

Peptide	Method	ΔG^o [kJ/mol]
pE-Aβ(3-42)	experiment (pH = 8, 25^{o}C)	-30.7 ± 0.08
pE-Aβ(3-42)	simulation (current study- HPO)	-56.5 ± 5.5
Aβ(1-40)	experiment (Saric et al.[299])	-27.5
Aβ(1-40)	simulation (Schwierz et al.[287])	-63.1 ± 2.5
Aβ(1-42)	experiment (Cohen et al.[67])	-27
Aβ(1-42)	experiment (pH = 8, 25^{o}C)	-27.7 ± 0.02
Aβ(1-42)	experiment (pH = 7, 25^{o}C)	-28.1 ± 0.05
Aβ(1-42)	simulation (Bellaiche et al.[40])	-19 ± 2
Aβ(1-42)	simulation (current study - HPO)	-36.5 ± 8.3
Aβ(1-42)	simulation (current study - HPI)	-54.8 ± 4.5

Error bars for experimental values were propagated from errors in dissociation constants. Error bars for values from simulations were calculated as the standard deviation of ΔG^o values from four non-overlapping intervals.

and close to the experimental value of -27 kJ mol^{-1}. When binding to the hydrophilic region K16-K28 of the fibril, however, the change in free energy reaches larger values, similar to those of pE-Aβ(1-42). A computational study by Bellaiche et al. [40] reported a value of -19 kJ mol^{-1}, lower than the experimental free energies and yet another binding site involving amino acid K16 from the fibril. One of the major strengths of computational methods is that they can capture precisely the binding site of the monomers to the fibril surface, which is not the case for the types of bio-sensing experiments we have performed to determine the binding affinity. Thus, we observe a large range of binding free energy values for three specific locations along the fibrillar peptides, range which also contains the experimental values. In real systems, the binding of monomers to the fibril surface may be composed of a multitude of different binding modes and sites, which taken altogether would lead to the experimental binding free energy values. Ideally, if all the binding sites and modes could be investigated computationally and weighed according to their free energy and stoichiometry, then it might be possible to identify an average free energy value similar to the experimental one.

Depending on the binding site and free energy, the binding of monomers to the fibril surface can have different consequences. Among these are the generation of toxic oligomers (add citation), the formation of new fibrils by secondary nucleation, or the templating of secondary protofilaments onto an already existing one. The last one implies that the peptides attach to

the hydrophobic side of the fibril which is also part of the interface between two filaments in a mature fibril, see Fig. **4-5** (b). This exact type of binding was also observed for pE-Aβ(3-42) monomer and for Aβ(1-42). Eventually, pE-Aβ(3-42) should display a similar behavior to Aβ(1-42), and bind to several sites on the fibril, but the fact that the first preference is for the hydrophobic surface emphasize its highly hydrophobic character and distinction from Aβ(1-42). Interestingly, this strong binding, enabled predominantly by hydrophobic interactions, is also observed when strong hydrogen bonds and salt bridges between hydrophilic amino acids contribute to the molecular interactions, as in the case of Aβ(1-42) binding to the hydrophilic side of the fibril.

It has been proposed that efficient secondary nucleation requires a finely balanced binding free energy of the monomer to the fibril surface - too weak and there is not enough peptide bound, too strong and the monomer cannot undergo the necessary conformational re-arrangements and detachment step to form a fully independent new fibril [355]. In a pure aggregating peptide, the monomer-fibril interaction regime will manifest itself by the efficiency with which the fibrils can proliferate. However, in mixed systems, such as the one we have investigated here, that contains fibrils of one type and monomer of another, even inhibition can be expected, relative to the pure system, if the monomeric peptides interact to form mixed nuclei, or if one peptide strongly and non-productively interacts with fibrils formed by another peptide form. This type of behaviour has been observed in the case of the Aβ(1-42)-pE-Aβ(3-42) mixed system [80], and our experiments and simulations in the present study help to rationalise these observations. We find a slightly higher affinity of the pE-Aβ(3-42) peptide for Aβ(1-42) fibrils, compared to the self-interaction of Aβ(1-42) monomer with Aβ(1-42) fibrils. It is interesting to note that a small difference in affinity can lead to such a dramatic inversion in kinetic behaviour, from acceleration in the case of the pure system to inhibition in the case of the mixed system.

These results highlight the necessity to study mixed peptide systems under a variety of solution conditions in order to be able to approach the full complexity present *in vivo*. Relatively small changes in both solution conditions (pH 7.4-pH 8) and peptide sequence (Aβ(1-42)-pE-Aβ(3-42)) can have dramatic effects on the aggregation behaviour. It has previously been show that the tendency of Aβ(1-42) to form oligomers significantly increases as the pH is lowered [289]. It is possible that the change from pH 8 to pH 7.4 leads to a differential increase in oligomerisation of the two peptides Aβ(1-42) and pE-Aβ(3-42) and that this explains their difference in affinity for the fibril surface. This effect would not be captured in our simulations, as we only had one monomeric peptide molecule in the simulation box. While it is currently still computationally too expensive to simulate several monomers together with a fibril, future studies should aim to simulate such a system. Such simulations may enable the processes of oligomerisation and secondary nucleation to be caught in the act.

4.6 Conclusions

In conclusion, we have performed a combined experimental and computational study of the interaction of the physiologically relevant Aβ isoform pE-Aβ(3-42) with fibrils formed by the Aβ(1-42) peptide. We find that this interaction is of high affinity than the self-interaction between Aβ(1-42) fibrils and Aβ(1-42) monomers in both experiment and simulations. These results rationalise previous observations that Aβ(1-42) fibrils can inhibit, rather than seed, the aggregation pE-Aβ(3-42). Our work highlights the potential of combined experimental and computational studies, as well as the complexity of mixed aggregating peptide systems. Increased focus on such mixed systems is crucial in our quest to reach an ever more realistic description of the situation *in vivo*. Besides, future exploration towards development of a drug candidate or biomarker for early diagnosis of AD might utilizes the understanding towards thermodynamic insights into the interplay of binding between mixed peptide system at a close regime from the current study for therapeutic approach towards AD pathology.

4.7 Acknowledgement

The authors gratefully acknowledge the computing time granted by the John von Neumann Institute for Computing (NIC) and provided on the supercomputer JURECA at Jülich Supercomputing Centre (JSC). Additional computational infrastructure and support were provided by the Centre for Information and Media Technology at Heinrich Heine University Düsseldorf. We also acknowledge DFG grant BA 5956/2-1 for funding the current research. AKB thanks the Novo Nordisk Foundation for support through a Novo Nordisk Foundation Professorship (NNFSA170028392). We thank Sara Linse for help with the SPR experiments.

4.8 Appendix - Chapter 4

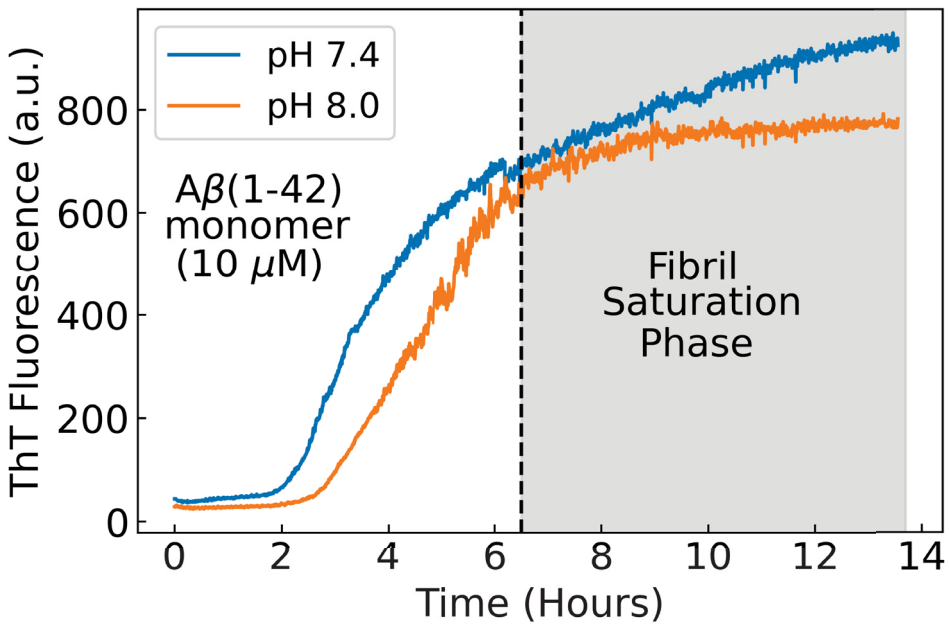

Figure **4-10**: ThT kinetics profile for fibrillation of 10 μM Aβ(1-42) monomer in both pH 7.4 and 8.0; in both cases the fibrils from the highlighted saturation phase were taken for further experiments with QCM and SPR.

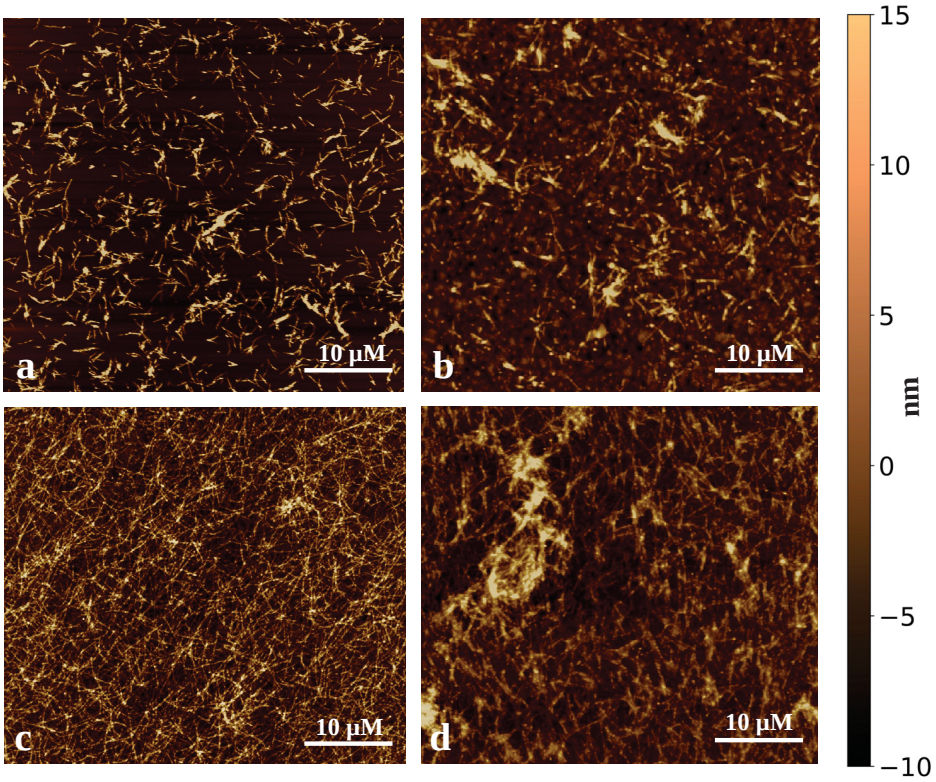

Figure **4-11**: AFM images of the Aβ(1-42) fibril samples at pH 7.4 - (a) Aβ(1-42) fibril sample on the mica surface, (b) Aβ(1-42) fibril sample on the QCM sensor before fibril growth after sonication before monomer injection, (c) Aβ(1-42) fibril samples on the QCM sensor after Aβ(1-42) monomer injection and (d) fully grown Aβ(1-42) fibril samples on the QCM sensor after pE-Aβ(3-42) monomer injection

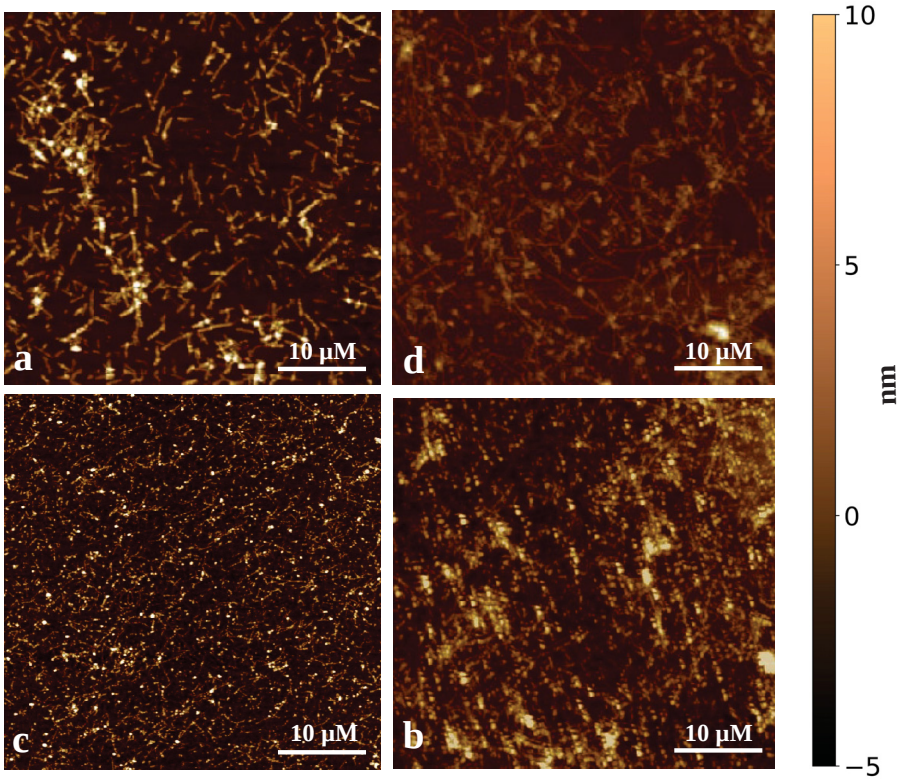

Figure **4-12**: AFM images of the Aβ(1-42) fibril samples at pH 8.0 - (a) Aβ(1-42) fibril sample on the mica surface, (b) Aβ(1-42) fibril sample on the QCM sensor before fibril growth after sonication before monomer injection, (c) Aβ(1-42) fibril samples on the QCM sensor after Aβ(1-42) monomer injection and (d) fully grown Aβ(1-42) fibril samples on the QCM sensor after pE-Aβ(3-42) monomer injection.

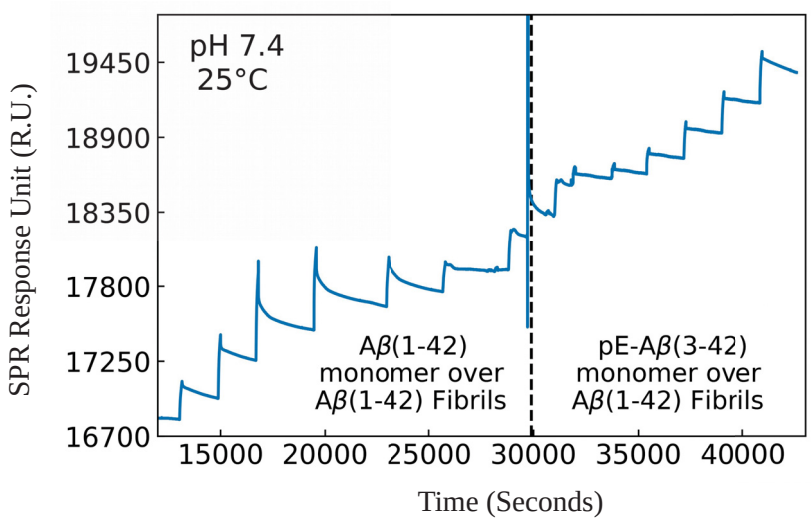

Figure **4-13**: RAW data (blank corrected) of SPR study from binding of both Aβ(1-42) and pE-Aβ(3-42) monomer on the attached Aβ(1-42) fibrils in concentration dependence manner after attaining baseline signal in pH 7.4 at 25°C. The nature of the SPR dissociation signals from the pE-Aβ(3-42) monomer at pH 7.4 is significantly different from the case of Aβ(1-42) monomer.

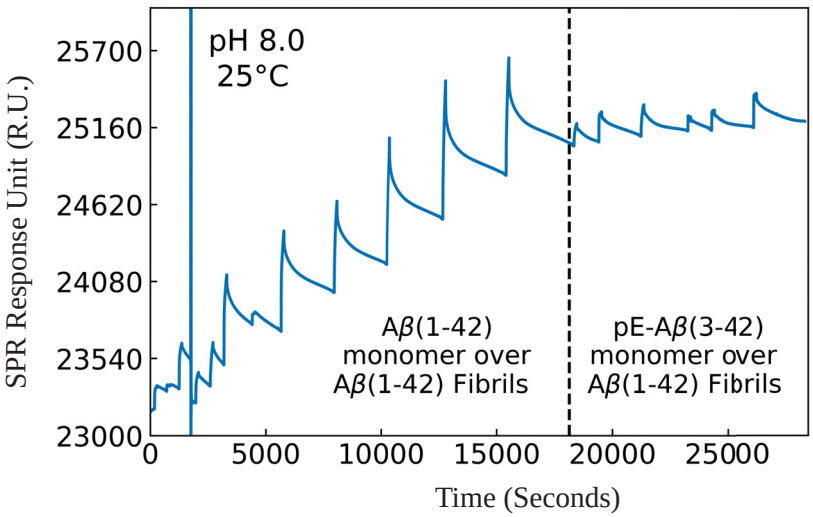

Figure **4-14**: RAW data (blank corrected) of SPR study from binding of both Aβ(1-42) and pE-Aβ(3-42) monomer on the attached Aβ(1-42) fibrils in concentration dependence manner after attaining baseline signal in pH 8.0 at 25°C. The nature of the SPR dissociation signals from the pE-Aβ(3-42) monomer at pH 8.0 is similar to the case of Aβ(1-42) monomer.

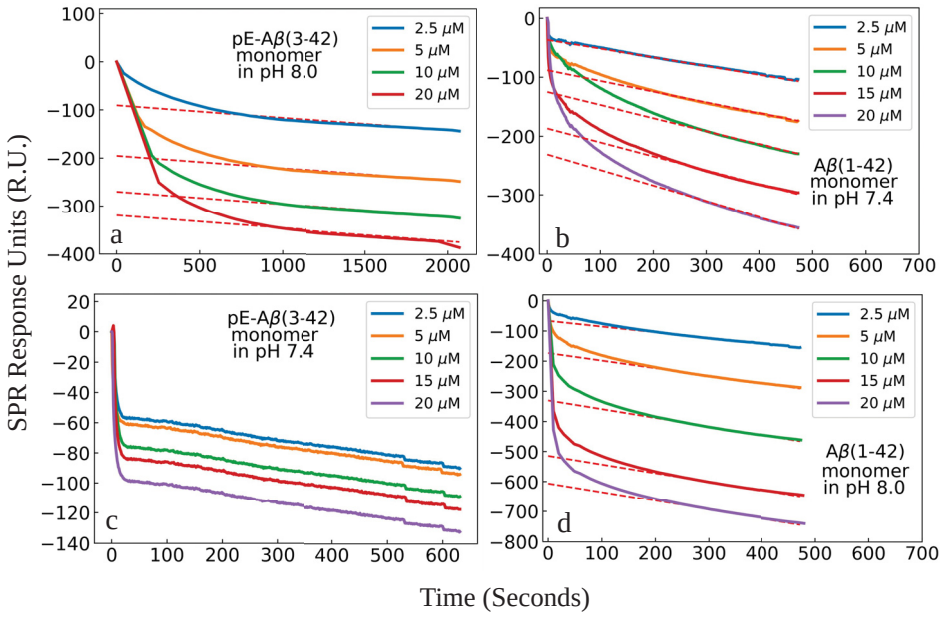

Figure **4-15**: Reverse amplitude calculations for the binding of free monomers to the Aβ(1-42) fibril surface at 25°C using the exponential component of the SPR dissociation signal via linear fit of the linear component of the SPR dissociation signal from different scenarios: (a) pE-Aβ(3-42) monomer in pH 8.0, (b) Aβ(1-42) monomer in pH 8.0, (c) pE-Aβ(3-42) monomer in pH 7.4 and (d) Aβ(1-42) monomer in pH 7.4; in the scenario (c) the reverse amplitudes for the pE-Aβ(3-42) monomer binding to the Aβ(1-42) fibril surface couldn't be done due to absence of exponential component in the SPR dissociation signal which corresponds to irreversible binding nature of pE-Aβ(3-42) monomers with the Aβ(1-42) fibril surface blocking secondary nucleation.

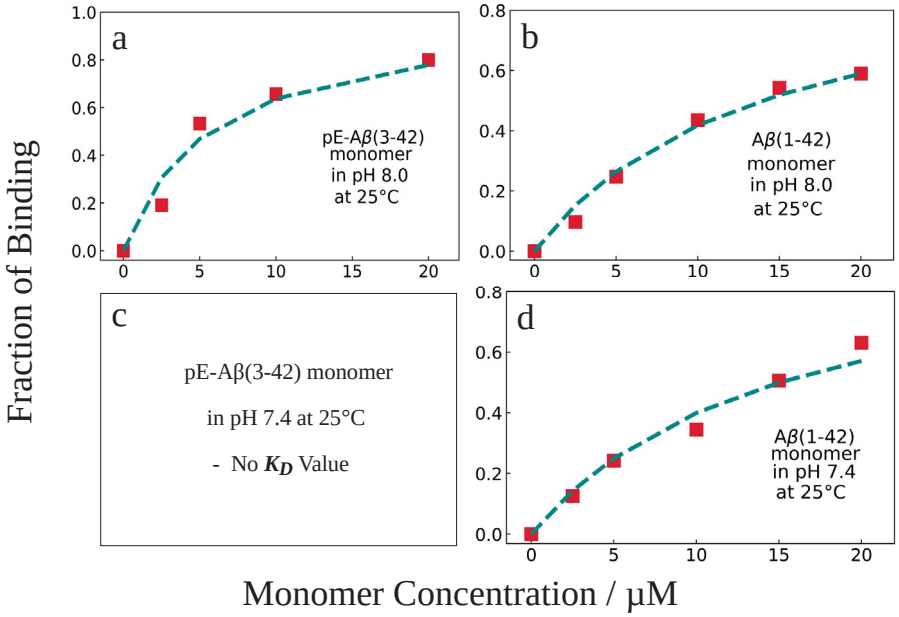

Figure **4-16**: Plot for the Langmuir Isotherm fit with the reverse amplitudes per monomer concentration from the SPR data of free monomers binding to the Aβ(1-42) fibril surface at 25°C in different scenarios as: (a) pE-Aβ(3-42) monomer at pH 8.0, (b) Aβ(1-42) monomer at pH 8.0, (c) pE-Aβ(3-42) monomer at pH 7.4 and (d) Aβ(1-42) monomer at pH 7.4. The K_D value at scenario (c) couldn't be calculated since pE-Aβ(3-42) binding the Aβ(1-42) fibril surface at this condition was irreversible and subsequently no exponential component of the decay signal was observed as showed in Fig. **4-15** (c).

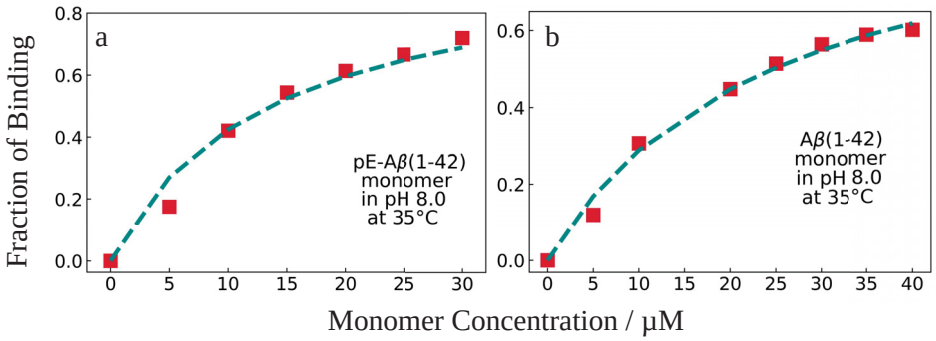

Figure **4-17**: Plot for the Langmuir Isotherm fit with the reverse amplitudes per monomer concentration from the SPR data of free monomers binding to the Aβ(1-42) fibril surface at 35°C in different scenarios as: (a) pE-Aβ(3-42) monomer at pH 8.0 and (b) Aβ(1-42) monomer at pH 8.0.

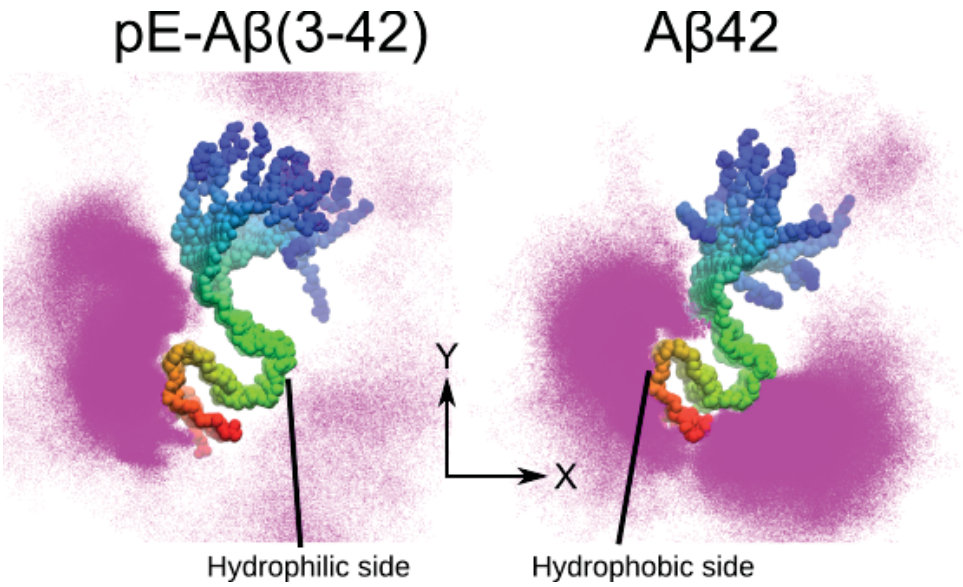

Figure **4-18**: Density maps from HREMD simulations show that pE-Aβ(3-42) monomer prefers binding only to the hydrophobic side of the Aβ(1-42) fibril surface whereas Aβ(1-42) monomer prefers to bind both hydrophillic and hydrophobic side of the Aβ(1-42) fibril surface.

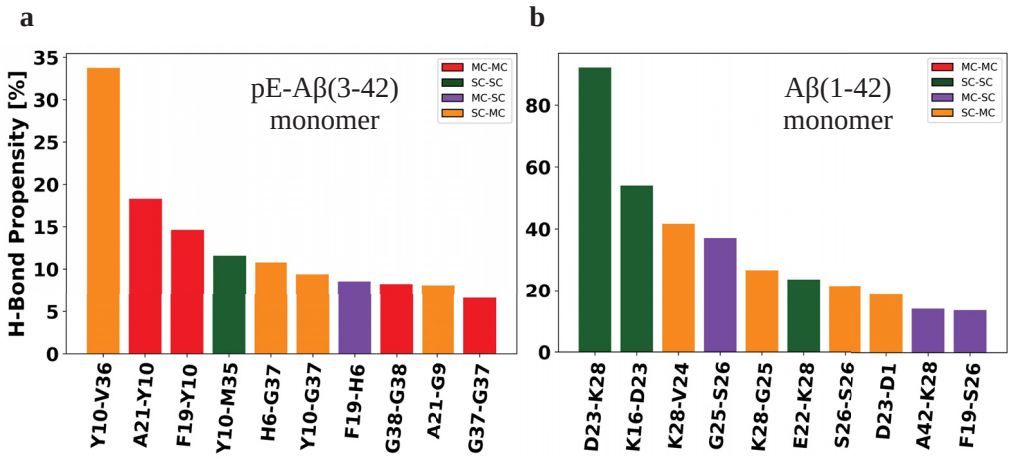

Figure **4-19**: H-bonding propensity between the free monomer and the Aβ(1-42) fibril surface, where all the first residues belong to the free monomers, for the case of (A) pE-Aβ(3-42) monomer and (B) Aβ(1-42) monomer. The interactons are defined as MC-MC: Main-Chain:Main-Chain, SC-SC: Side-Chain:Side-Chain, MC-SC: Main-Chain:Side-Chain and SC-SC: Side-Chain:Side-Chain.

5 Conclusions and Future Perspective

Despite numerous studies have been performed on the generation of amyloid fibrils, a major hallmark of AD; still, a lack of understanding the insights into the underlying *in-vivo* AD pathology prevails, which may be correlated to the presence of various Aβ isoforms in the human brain. It is plausible in a mixed-peptide system as found *in-vivo*, the cross-secondary nucleation mechanism plays a pivotal role in modifying the aggregation kinetics of monomeric Aβ isoforms by the presence of a variety of fibrils of different polymorphs. Generally, an increase in aggregation rates for different monomeric Aβ isoforms has been found in the presence of Aβ(1-42) fibrils in many studies (both *in-vitro* and *in-vivo*), except for the pE-Aβ(3-42) monomer whose aggregation seems to be inhibited by the presence of Aβ(1-42) fibrils. The current work particularly focused on understanding the thermodynamic insights into the binding of pE-Aβ(3-42) monomer with the Aβ(1-42) fibril reveals that pE-Aβ(3-42) monomer bind tightly (having more negative ΔG^{o}) & exclusively towards the hydrophobic side of the fibril compared to the binding of Aβ(1-42) monomer; the latter shows dual-mode of binding both to the hydrophobic & hydrophilic side of the fibril. The conformational analysis at the atomic-scale shows that the pE-Aβ(3-42) monomer adopts a more β-sheet rich structure without many structural rearrangements upon binding to the fibril surface due to the involvement of both N- and C-terminus of the monomer into the binding. However, the propensity of adopting a β-sheet rich structure is found to be declined for the Aβ(1-42) monomer upon binding to the fibril surface and it undergoes significant structural rearrangements for binding the hydrophobic side through its C-terminus & hydrophilic side through it's β-hairpin region. The exclusive binding of pE-Aβ(3-42) monomer to the hydrophobic side of the fibril may be correlated with the results from the conformational analysis for monomers alone. The pE-Aβ(3-42) monomer shows significant exposure of hydrophobic residues to the solvent with a more anti-parallel β-sheet rich structure compared to that of the Aβ(1-42) monomer, which shows adoption of an S-shaped compact-fibril like structure similar to the Aβ(1-42) fibril end. Besides, D23 residue in pE-Aβ(3-42) monomer is found to be more available for strong inter-molecular interactions rather than Aβ(1-42) monomer where this is significantly involved in the D1-D23 salt-bridge formation. The outcomes of my doctoral dissertation rationalize the previous observations of inhibition of pE-Aβ(3-42) monomer aggregation by Aβ(1-42) fibrils in terms of tighter binding of the monomer exclusively to the hydrophobic side of the fibril, outweighing the required structural rearrangement of the monomer for effective cross-nucleation to take place; along with the observed biophysical properties like higher aggregation rate & toxicity of pE-Aβ(3-42) monomer compared to that of Aβ(1-42) monomer. Finally, the knowledge from the current project can be applied for developing potential drug candidates for inhibition of aggregation or biomarkers for early detection of the Aβ(1-42) fibrils generating *in-vivo* targeting irreversible binding with the fibril surface, paving the pathway towards a therapeutic approach of AD pathology.

Author Contributions

Chapter Two

Article: Compact fibril-like structure of amyloid β-peptide (1–42) monomers

Authors: Bogdan Barz, Alexander K. Buell and Soumav Nath

Details: Chem. Comm., 2021, 57, 947-950, DOI:10.1039/d0cc06607a

Contribution: I contributed towards the data analysis. The research design and the paper writing was done in collaboration with Dr. Bogdan Barz and Prof. Dr. Alexander Kai Büll.

Chapter Three

Contribution: I contributed towards performing the MD simulation and data analysis. The research design and the manuscript writing was done in collaboration with Dr. Bogdan Barz and Prof. Dr. Alexander Kai Büll.

Chapter Four

Contribution: I contributed towards performing the experiments, MD simulation and data analysis. The research design and the manuscript writing was done in collaboration with Dr. Bogdan Barz and Prof. Dr. Alexander Kai Büll.

List of Publications

Published Manuscripts

B. Barz*, A.K. Buell, ***S. Nath***, *Compact fibril-like structure of amyloid -peptide (1–42) monomers*, ***Chemical Communications***, 57, 947-950 **(2021)**.

Under Preparation Manuscripts

S. Nath, A.K. Buell, B. Barz*, *N-terminal truncated Pyroglutamate-modified Aβ(3-42) monomer structure differs significantly compared to Aβ(1-42) monomer.***(Manuscript Under Preparation)**

S. Nath, L. Gremer, D. Willbold, B. Barz*, A.K. Buell*, *Pyroglumate-modified Aβ(3-42) monomers bind with higher affinity than Aβ(1-42) monomers to Aβ(1-42) fibrils.***(Manuscript Under Preparation)**

J. Bartl, M. Zanini, A. Forget, D. Picard, N. Qin, Q. Gao, ***S. Nath***, I. M. Koumba, M. Wolter, F. X. H. Kuonen, M. Langini, T. Beez, L. Blümel, D. Pauck, V. Marquardt, H. Yu, M. Korsch, C. Mölders, D. Berger, S. Göbbels, F. D. Meyer, B. Scheffler, B. Rotblat, S. Diederichs, V. Ramaswamy, A. Oro, K. Stühler, U. Fischer, G. Leprivier, D. Willbold, G. Steger, A. K. Büll, M. Kool, P. Lichter, S. M. Pfister, P. A. Northcott, M. D. Taylor, A. Borkhardt, G. Reifenberger*, O. Ayrault*, M. Remke*, *" Epigenetic regulation through the long non coding RNA HHIP-AS1 promotes tumor progression in human SHH-driven brain tumors "***(Submitted)**

Bibliography

[1] Web Site Force-Field AMBER. In: *http://ambermd.org*

[2] A, Alzheimer: On a peculiar disease of the cerebral cortex. In: *Allgemeine Zeitschrift fuer Psychiatrie und Psychischgerichtliche Medizin* 64 (1907), S. 146–148

[3] A, Antonyan ; D, Schlenzig ; S, Schilling ; M, Naumann ; S, Sharoyan ; S, Mardanyan ; HU, Demuth: Concerted action of dipeptidyl peptidase IV and glutaminyl cyclase results in formation of pyrogluta- mate-modified amyloid peptides *in vitro*. In: *Neurochem. Int.* 113 (2018), S. 112–119

[4] A, Arnau: A review of interface electronic systems for AT-cut quartz crystal microbalance applications in liquids. In: *Sensors* 8 (2008), S. 370–411

[5] A, Laio ; FL, Gervasio: Reports on Progress in Physics Metadynamics: a method to simulate rare events and reconstruct the free energy in biophysics, chemistry and material science. In: *Rep. Prog. Phys.* 71 (2008)

[6] A, Modler ; K, Gast ; G, Lutsch ; G, Damaschun: Assembly of Amyloid Protofibrils via Critical Oligomers—A Novel Pathway of Amyloid Formation. In: *J. Mol. Biol.* 325 (2003)

[7] A, Quintas ; MJM, Saraiva ; RMM, Brito: The amyloidogenic potential of transthyretin variants correlates with their tendency to aggregate in solution. In: *Febs. Lett.* 418 (1997)

[8] A, Shkurti ; ID, Styliari ; V, Balasubramanian ; I, Bethune ; C, Pedebos ; S, Jha ; CA, Laughton: CoCo-MD: A Simple and Effective Method for the Enhanced Sampling of Conformational Space. In: *J. Chem. Theory Comput.* 15 (2019), S. 2587−2596

[9] A, Vitalis ; A, Caflisch: 50 Years of Lifson-Roig Models: Application to Molecular Simulation Data. In: *J. Chem. Theory Comput.* 8 (2012), S. 363–373

[10] AD, MacKerell ; D, Bashford ; M, Bellott ; RL, Dunbrack ; JD, Evanseck ; MJ, Field ; S, Fischer ; J, Gao ; H, Guo ; S, Ha ; D, Joseph-McCarthy ; L, Kuchnir ; K, Kuczera ; FTK, Lau ; C, Mattos ; S, Michnick ; T, Ngo ; DT, Nguyen ; B, Prodhom ; WE, Reiher ; B, Roux ; M, Schlenkrich ; JC, Smith ; R, Stote ; J, Straub ; M, Watanabe ; J, Wiorkiewicz-Kuczera ; D, Yin ; M, Karplus: All-atom empirical potential for molecular modeling and dynamics studies of proteins. In: *J. Phys. Chem. B* 102 (1998), S. 3586–3616

[11] AD, Mackerell ; M, Feig ; CL, Brooks: Extending the treatment of backbone energetics in protein force fields: Limitations of gas-phase quantum mechanics in reproducing protein conformational distributions in molecular dynamics simulations. In: *J. Comput. Chem.* 25 (2004), S. 1400–1415

[12] Aguzzi, Adriano ; O'Connor, Tracy: Protein aggregation diseases: pathogenicity and therapeutic perspectives. In: *Nat Rev Drug Discov.* 9 (2010), Nr. 3, S. 237–48

[13] Ahlström, P ; Wallqvist, A ; Engström, S ; Jönsson, B: A molecular-dynamics study of polarizable water. In: *Mol. Phys.* 68 (1989), S. 563–581

[14] AJ, Geddes ; KD, Parker ; EDT, Atkins ; E, Beighton: "Cross-β" conformation in proteins. In: *J. Mol. Biol.* 32 (1968)

[15] et al., AD M.: All-atom empirical potential for molecular modeling and dynamics studies of proteins. In: *J. Phys. Chem.* 102 (1998), S. 3586–3616

[16] et al., JW P.: Current status of the AMOEBA polarizable force field. In: *J. Phys. Chem. B* 114 (2010), S. 2549–2564

[17] AL, Watters ; P, Deka ; C, Corrent ; D, Callender ; G, Varani ; T, Sosnick ; D, Baker: The highly cooperative folding of small naturally occurring proteins is likely the result of natural selection. In: *Cell* 128 (2007)

[18] et al., WD C.: A second generation force field for the simulation of proteins, nucleic acids, and organic molecules. In: *J. Am. Chem. Soc.* 117 (1995), S. 5179–5197

[19] van Gunsteren et al., WF: GROMOS web site. In: *http://www.igc.ethz.ch/GROMOS/index*

[20] Aliev, AE ; Courtier-Murias, D: Experimental verification of force fields for molecular dynamics simulations using Gly-Pro-Gly-Gly. In: *J. Phys. Chem. B* 114 (2010), S. 12358–12375

[21] Allinger, NL: Conformational analysis. 130. MM2. a hydrocarbon force field utilizing V1 and V2 torsional terms. In: *J. Am. Chem. Soc.* 99 (1977), S. 8127–8134

[22] Allinger, NL ; Chen, K ; Lii, JH: Improved force field (MM4) for saturated hydrocarbons. In: *J. Comput. Chem.* 17 (1996), S. 642–668

[23] Allinger, NL ; Yuh, YH ; Lii, JH: Molecular mechanics. the MM3 force field for hydrocarbons. 1. In: *J. Am. Chem. Soc.* 111 (1989), S. 8551–8565

[24] Almeida, Zaida L. ; Brito, Rui M.: Structure and Aggregation Mechanisms in Amyloids. In: *Molecules.* 25

[25] AM, Morris ; MA, Watzky ; JN, Agar ; RG, Finke: Fitting Neurological Protein Aggregation Kinetic Data via a 2-Step, Minimal/"Ockham's Razor" Model: The Finke−Watzky Mechanism of Nucleation Followed by Autocatalytic Surface Growth. In: *Biochemistry* 47 (2008)

[26] AM, Morris ; MA, Watzky ; RG, Finke: Protein aggregation kinetics, mechanism, and curve-fitting: A review of the literature. In: *Biochim. Et Biophys. Acta (BBA)-Proteins Proteom.* 1794 (2009)

[27] Antzutkin, Oleg N. ; Leapman, Richard D. ; Balbach, John J. ; Tycko, Robert: Supramolecular structural constraints on Alzheimer's beta-amyloid fibrils from electron microscopy and solid-state nuclear magnetic resonance. In: *Biochemistry.* 41

[28] AR, Lam ; DB, Teplow ; HE, Stanley ; B, Urbanc: Effects of the Arctic (E22–¿G) mutation on amyloid beta-protein folding: discrete molecular dynamics study. In: *J. Am. Chem. Soc.* 130 (2008), S. 17413−17422

[29] AV, Onufriev ; DA, Case: Generalized Born Implicit Solvent Models for Biomolecules. In: *Annu. Rev. Biophys.* 48 (2019), S. 275–296

[30] B, Morel ; MP, Carrasco ; S, Jurado ; C, Marco ; F, Conejero-Lara: Dynamic micellar oligomers of amyloid beta peptides play a crucial role in their aggregation mechanisms. In: *Phys. Chem. Chem. Phys.* 20 (2018)

[31] B, O'Nuallain ; S, Shivaprasad ; I, Kheterpal ; R, Wetzel: Thermodynamics of Aβ(1−40) Amyloid Fibril Elongation. In: *Biochemistry* 44 (2005)

[32] Ball, K. A. ; Phillips, Aaron H. ; Wemmer, David E. ; Head-Gordon, Teresa: Differences in β-strand Populations of Monomeric Aβ40 and Aβ42. In: *Biophys. J.* 104 (2013), Jun, Nr. 12, S. 2714–2724. – ISSN 0006–3495

[33] Barducci, Alessandro ; Bonomi, Massimiliano ; Derreumaux, Philippe: Assessing the Quality of the OPEP Coarse-Grained Force Field. In: *J. Chem. Theory Comput.* 7 (2011)

[34] Barker, JA ; Watts, RO: Structure of water; a Monte Carlo calculation. In: *Chem. Phys. Lett.* 3 (1969), S. 144–145

[35] Barz, Bogdan ; Buell, Alexander K. ; Nath, Soumav: Compact fibril-like structure of amyloid β-peptide (1-42) monomers. In: *Chem. Commun.* 57 (2021), Nr. 7, S. 947–950

[36] Barz, Bogdan ; Liao, Qinghua ; Strodel, Birgit: Pathways of Amyloid-β Aggregation Depend on Oligomer Shape. In: *J. Am. Chem. Soc.* 140 (2018), Jan, Nr. 1, S. 319–327. – ISSN 0002–7863

[37] Barz, Bogdan ; Strodel, Birgit: Understanding Amyloid-β Oligomerization at the Molecular Level: the Role of the Fibril Surface. In: *Chem. Eur. J* 22 (2016), Mai, S. 8768–8772. – ISSN 1521–3765

[38] Barz, Bogdan ; Urbanc, Brigita: Dimer Formation Enhances Structural Differences between Amyloid β-Protein (1â[U+0080][U+0093]40) and (1â[U+0080][U+0093]42): A n Explicit-Solvent Molecular Dynamics Study. In: *PLoS One* 7 (2012), April, Nr. 4, S. e34345. – ISSN 1932–6203

[39] Bayer, Thomas A. ; Wirths, Oliver: Focusing the amyloid cascade hypothesis on N-truncated Abeta peptides as drug targets against Alzheimer's disease. In: *Acta. Neuropathol.* 127 (2014), Nr. 6, S. 787–801

[40] Bellaiche, M.M.J. ; Best, R.B.: Molecular Determinants of Aβ_{42} Adsorption to Amyloid Fibril Surfaces. In: *J. Phys. Chem. Lett.* 9 (2018), Nr. 22, S. 6437–43

[41] Benzinger, Tammie L. S. ; Gregory, David M. ; Burkoth, Timothy S. ; Miller-Auer, Hélène ; Lynn, David G. ; Botto, Robert E. ; Meredith, Stephen C.: Propagating structure of Alzheimer's β-amyloid(10–35) is parallel β-sheet with residues in exact register. In: *Proc. Natl. Acad. Sci. U.S.A.* 95 (1998), Nov, Nr. 23, S. 13407

[42] Bernstein, S. L. ; Dupuis, N. F. ; Lazo, N. D. ; Wyttenbach, T. ; Condron, M. M. ; Bitan, G. ; Teplow, D. B. ; Shea, J.-E. ; Ruotolo, B. T. ; Robinson, C. V. ; Bowers, M. T.: Amyloid-β protein oligomerization and the importance of tetramers and dodecamers in the aetiology of Alzheimer's disease. In: *Nat. Chem.* 1 (2009), S. 326–331

[43] Best, Robert B. ; Hummer, Gerhard: Optimized Molecular Dynamics Force Fields Applied to the Helixâ[U+0088][U+0092]Coil Transition of Polypeptides. In: *J. Phys. Chem. B* 113 (2009), Juli, Nr. 26, S. 9004–9015. – ISSN 1520–6106

[44] Bitan, G. ; Kirkitadze, M. D. ; Lomakin, A. ; Vollers, S. S. ; Benedek, G. B. ; Teplow, D. B.: Amyloid β-protein (Aβ) assembly: Aβ40 and Aβ42 oligomerize through distinct pathways. In: *Proc. Natl. Acad. Sci.* 100 (2003), Nr. 1, S. 330–335

[45] Brender, Jeffrey R. ; Ghosh, Anirban ; Kotler, Samuel A. ; Krishnamoorthy, Janarthanan ; Bera, Swapna ; Morris, Vanessa ; Sil, Timir B. ; Garai, Kanchan ; Reif, Bernd ; Bhunia, Anirban ; Ramamoorthy, Ayyalusamy: Probing transient non-native states in amyloid beta fiber elongation by NMR. In: *Chem. Commun.* 55 (2019), S. 4483–4486

[46] Buell, AK ; White, DA ; Meier, C ; Welland, ME ; Knowles, TPJ ; Dobson, CM: Surface attachment of protein fibrils via covalent modification strategies. In: *J. Phys. Chem. B* 114 (2010), S. 10925–10938

[47] Buell, Alexander K.: The growth of amyloid fibrils: rates and mechanisms. In: *Biochem. J.* 476

[48] Buell, Alexander K.: The Nucleation of Protein Aggregates - From Crystals to Amyloid Fibrils. In: *Int. Rev. Cell. Mol. Biol.* 329 (2017), S. 187–226

[49] Buell, Alexander K.: The growth of amyloid fibrils: rates and mechanisms. In: *Biochem. J.* 476 (2019), Oct, Nr. 19, S. 2677–2703. – ISSN 0264–6021

[50] Buell, Alexander K. ; Blundell, Jamie R. ; Dobson, Christopher M. ; Welland, Mark E. ; Terentjev, Eugene M. ; Knowles, Tuomas P. J. ; Buell, Alexander K. ; Blundell, Jamie R. ; Dobson, Christopher M. ; Welland, Mark E. ; Terentjev, Eugene M. ; Knowles, Tuomas P. J.: Frequency Factors in a Landscape Model of

Filamentous Protein Aggregation. In: *Phys. Rev. Lett.* 104 (2010), Jun, Nr. 22, S. 228101.. – ISSN 1079–7114

[51] Buell, Alexander K. ; Dhulesia, Anne ; Mossuto, Maria F. ; Cremades, Nunilo ; Kumita, Janet R. ; Dumoulin, Mireille ; Welland, Mark E. ; Knowles, Tuomas P. ; Salvatell, Xavier ; Dobson, Christopher M.: Population of nonnative states of lysozyme variants drives amyloid fibril formation. In: *J. Am. Chem. Soc.* 133

[52] Buell, Alexander K. ; Dhulesia, Anne ; White, Duncan A. ; Knowles, Tuomas P. J. ; Dobson, Christopher M. ; Welland, Mark E.: Detailed Analysis of the Energy Barriers for Amyloid Fibril Growth. In: *Angew. Chem. Int. Ed.* 51 (2012), Mai, Nr. 21, S. 5247–5251. – ISSN 1521–3773

[53] Buell, Alexander K. ; Dobson, Christopher M. ; Welland, Mark E.: Measuring the kinetics of amyloid fibril elongation using quartz crystal microbalances. In: *Methods. Mol. Biol.* 849 (2012), S. 101–119

[54] Bunce, Samuel J. ; Wang, Yiming ; Stewart, Katie L. ; Ashcroft, Alison E. ; Radford, Sheena E. ; Hall, Carol K. ; Wilson, Andrew J.: Molecular insights into the surface-catalyzed secondary nucleation of amyloid-β_{40} (Aβ_{40}) by the peptide fragment A$\beta_{16\text{-}22}$. In: *Sci. Adv.* 5 (2019), Nr. 6, S. eaav8216

[55] Bussi, G. ; Donadio, D. ; Parrinello, M.: Canonical sampling through velocity rescaling. In: *J. Chem. Phys.* 126 (2007), S. 014101

[56] Bussi, Giovanni: Hamiltonian replica exchange in GROMACS: a flexible implementation. In: *Mol. Phys.* 112 (2014), Februar, Nr. 3-4, S. 379–384. – ISSN 0026–8976

[57] C, Haass ; DJ, Selkoe: Cellular processing of beta-amyloid precursor protein and the genesis of amyloid beta-peptide. In: *Cell* 75 (1993), S. 1039–42

[58] C, Priller ; T, Bauer ; G, Mitteregger ; B, Krebs ; HA, Kretzschmar ; J, Herms: Synapse formation and function is modulated by the amyloid precursor protein. In: *J. Neurosci.* 26 (2006), S. 7212–7221

[59] Camargo, Diana C R. ; Chia, Sean ; Menzies, Joseph ; Mannini, Benedetta ; Meisl, Georg ; Lundqvist, Martin ; Pohl, Christin ; Bernfur, Katja ; Lattanzi, Veronica ; Habchi, Johnny ; Cohen, Samuel I. ; Knowles, Tuomas P J. ; Vendruscolo, Michele ; Linse, Sara: Surface-Catalyzed Secondary Nucleation Dominates the Generation of Toxic IAPP Aggregates. In: *Front. Mol. Biosci.* 8 (2021), S. 757425

[60] Cao, Yang ; Tang, Xuan ; Yuan, Miao ; Han, Wei: Chapter Ten - Computational studies of protein aggregation mediated by amyloid: Fibril elongation and secondary nucleation. In: Strodel, Birgit (Hrsg.) ; Barz, Bogdan (Hrsg.): *Computational Approaches for Understanding Dynamical Systems: Protein Folding and Assembly* Bd. 170. Academic Press, 2020. – ISSN 1877–1173, S. 461 – 504

[61] Chakraborty, Debayan ; Straub, John E. ; Thirumalai, D: Differences in the free energies between the excited states of Aβ40 and Aβ42 monomers encode their aggregation propensities. In: *Proc. Natl. Acad. Sci. USA.* 117 (2020), S. 19926–19937

[62] Chen, Guo-fang ; Xu, Ting-hai ; Yan, Yan ; Zhou, Yu-ren ; Jiang, Yi ; Melcher, Karsten ; Xu, H E.: Amyloid beta: structure, biology and structure-based therapeutic development. In: *Acta Pharmacologica Sinica* 38 (2017), Nr. 9, S. 1205–1235

[63] Cieplak, P ; Dupradeau, FY ; Duan, Y ; Wang, J: Polarization effects in molecular mechanical force fields. In: *J. Phys.: Condens. Matter* 21 (2009), S. 333102–21

[64] CM, Dobson: Protein misfolding, evolution and disease. In: *Trends Biochem. Sci.* 24 (1999)

[65] Cohen, Samuel I. A. ; Cukalevski, Risto ; Michaels, Thomas C. T. ; Šarić, Anđela ; Törnquist, Mattias ; Vendruscolo, Michele ; Dobson, Christopher M. ; Buell, Alexander K. ; Knowles, Tuomas P. J. ; Linse, Sara ; Cohen, Samuel I. A. ; Cukalevski, Risto ; Michaels, Thomas C. T. ; Šarić, Anđela ; Törnquist, Mattias ; Vendruscolo, Michele ; Dobson, Christopher M. ; Buell, Alexander K. ; Knowles, Tuomas P. J. ; Linse, Sara: Distinct Thermodynamic Signatures of Oligomer Generation in the Aggregation of the Amyloid-β Peptide. In: *Nat. Chem.* 10 (2018), May, Nr. 5, S. 523–531. – ISSN 1755–4349

[66] Cohen, Samuel I A. ; Linse, Sara ; Luheshi, Leila M. ; Hellstrand, Erik ; White, Duncan A. ; Rajah, Luke ; Otzen, Daniel E. ; Vendruscolo, Michele ; Dobson, Christopher M. ; Knowles, Tuomas P J.: Proliferation of amyloid-β42 aggregates occurs through a secondary nucleation mechanism. In: *Proc. Natl. Acad. Sci. USA* 110

[67] Cohen, S.I.A. ; Cukalevski, R. ; Michaels, T.C.T. ; Šarić, A. ; Törnquist, M. ; Vendruscolo, M. ; Dobson, C.M. ; Buell, A.K. ; Knowles, T.P.J. ; Linse, S.: Distinct thermodynamic signatures of oligomer generation in the aggregation of the amyloid-β peptide. In: *Nat. Chem.* 10 (2018), Nr. 5, S. 523–531

[68] Colvin, Michael T. ; Silvers, Robert ; Ni, Qing Z. ; Can, Thach V. ; Sergeyev, Ivan ; Rosay, Melanie ; Donovan, Kevin J. ; Michael, Brian ; Wall, Joseph ; Linse, Sara ; Griffin, Robert G.: Atomic Resolution Structure of Monomorphic Aβ42 Amyloid Fibrils. In: *J. Am. Chem. Soc.* 138 (2016), August, Nr. 30, S. 9663–9674. – ISSN 0002–7863

[69] Colvin, Michael T. ; Silvers, Robert ; Ni, Qing Z. ; Can, Thach V. ; Sergeyev, Ivan ; Rosay, Melanie ; Donovan, Kevin J. ; Michael, Brian ; Wall, Joseph ; Linse, Sara ; Griffin, Robert G.: Atomic Resolution Structure of Monomorphic Aβ42 Amyloid Fibrils. In: *J. Am. Chem. Soc.* 138 (2016), Aug, Nr. 30, S. 9663–9674. – ISSN 0002–7863

[70] Côté, Sébastien ; Derreumaux, Philippe ; Mousseau, Normand: Distinct Morphologies for Amyloid Beta Protein Monomer: Aβ1–40, Aβ1–42, and Aβ1–40(D23N). In: *J. Chem. Theory Comput.* 7 (2011), Aug, Nr. 8, S. 2584–2592. – ISSN 1549–9618

[71] Crescenzi, Orlando ; Tomaselli, Simona ; Guerrini, Remo ; Salvadori, Severo ; D'Ursi, Anna M. ; Temussi, Piero A. ; Picone, Delia: Solution structure of

the Alzheimer amyloid β-peptide (1–42) in an apolar microenvironment. In: *Eur. J. Biochem.* 269 (2002), Nov, Nr. 22, S. 5642–5648. – ISSN 0014–2956

[72] CSH, Jesus ; ZL, Almeida ; DC, Vaz ; TQ, Faria ; RMM, Brito: A New Folding Kinetic Mechanism for Human Transthyretin and the Influence of the Amyloidogenic V30M Mutation. In: *Int. J. Mol. Sci.* 17 (2016)

[73] CT, Leahy ; A, Kells ; G, Hummer ; NV, Buchete ; E, Rosta: Peptide dimerization-dissociation rates from replica exchange molecular dynamics. In: *J. Chem. Phys.* 147 (2017), S. 152725

[74] Cukalevski, R. ; Yang, X. ; Meisl, G. ; Weininger, U. ; Bernfur, K. ; Frohm, B. ; Knowles, T.P.J. ; Linse, S.: The Aβ40 and Aβ42 peptides self-assemble into separate homomolecular fibrils in binary mixtures but cross-react during primary nucleation. In: *Chem. Sci.* 6 (2015), Nr. 7, S. 4215–33

[75] CY, Zhou ; F, Jiang ; YD, Wu: Residue-Specific Force Field Based on Protein Coil Library. RSFF2: Modification of AMBER ff99SB. In: *J. Phys. Chem. B* 119 (2015), S. 1035–1047

[76] D, Ruzafa ; L, Varela ; AI, Azuaga ; F, Conejero-Lara ; B, Morel: Mapping the structure of amyloid nucleation precursors by protein engineering kinetic analysis. In: *Phys. Chem. Chem. Phys.* 16 (2014)

[77] D, Song ; H, Liu ; R, Luo ; HF, Chen: Environment-Specific Force Field for Intrinsically Disordered and Ordered Proteins. In: *J. Chem. Inf. Model.* 60 (2020), S. 2257−2267

[78] D, Song ; W, Wang ; W, Ye ; D, Ji ; R, Luo ; HF, Chen: ff14IDPs force field improving the conformation sampling of intrinsically disordered proteins. In: *Chem. Biol. Drug Des.* 89 (2017), S. 5–15

[79] D, Thirumalai ; G, Reddy: Protein thermodynamics: Are native proteins metastable? In: *Nat. Chem.* 3 (2011)

[80] Dammers, C ; Schwarten, M ; Buell, A K. ; Willbold, D: Pyroglutamate-modified A(3-42) affects aggregation kinetics of A(1-42) by accelerating primary and secondary pathways. In: *Chem. Sci.* 8 (2017), Nr. 7, S. 4996–5004

[81] Dammers, Christina ; Gremer, Lothar ; Reiss, Kerstin ; Klein, Antonia N. ; Neudecker, Philipp ; Hartmann, Rudolf ; Sun, Na ; Demuth, Hans-Ulrich ; Schwarten, Melanie ; Willbold, Dieter: Structural Analysis and Aggregation Propensity of Pyroglutamate A(3-40) in Aqueous Trifluoroethanol. In: *PLoS. One.* 10 (2015)

[82] Dammers, Christina ; Reiss, Kerstin ; Gremer, Lothar ; Lecher, Justin ; Ziehm, Tamar ; Stoldt, Matthias ; Schwarten, Melanie ; Willbold, Dieter: Pyroglutamate-Modified Amyloid-(3-42) Shows -Helical Intermediates before Amyloid Formation. In: *Biophys. J.* 112 (2017), Nr. 8, S. 1621–1633

[83] Dammers, Christina ; Schwarten, Melanie ; Buell, Alexander ; Willbold, Dieter: Pyroglutamate-modified Aβ(3-42) Affects Aggregation Kinetics of Aβ(1-42) by Accelerating Primary and Secondary Pathways. In: *Chem. Sci.* (2017), Mai. – ISSN 2041–6539

[84] Daura, Xavier ; Gademann, Karl ; Jaun, Bernhard ; Seebach, Dieter ; van Gunsteren, Wilfred F. ; Mark, Alan E.: Peptide Folding: When Simulation Meets Experiment. In: *Angew. Chem. Int. Ed.* 38 (1999), Januar, Nr. 1-2, S. 236–240. – ISSN 1521–3773

[85] DC, Malaspina ; L, Perez-Fuentes ; C, Drummond ; D, Bastos-Gonzalez ; J, Faraudo: Protein-surface interactions at the nanoscale: Atomistic simulations with implicit solvent models. In: *Curr. Opin. Colloid Interface Sci.* 41 (2019), S. 40–49

[86] DG, Myszka ; SJ, Wood ; AL, Biere: Analysis of [U+FB01]bril elongation using surface plasmon resonance biosensors. In: *Methods Enzymol.* 309 (1999), S. 386–402

[87] DJ, Brockwell ; SE, Radford: Intermediates: Ubiquitous species on folding energy landscapes? In: *Curr. Opin. Struct. Biol.* 17 (2007)

[88] DJ, Selkoe ; J, Hardy: The amyloid hypothesis of Alzheimer's disease at 25 years. In: *EMBO Mol. Med.* 8 (2016), S. 595–608

[89] DS, Eisenberg ; MR, Sawaya: Structural Studies of Amyloid Proteins at the Molecular Level. In: *Annu. Rev. Biochem.* 86 (2017)

[90] E, Harder ; W, Damm ; J, Maple ; CJ, Wu ; M, Reboul ; JY, Xiang ; LL, Wang ; D, Lupyan ; MK, Dahlgren ; JL, Knight ; JW, Kaus ; DS, Cerutti ; G, Krilov ; WL, Jorgensen ; R, Abel ; RA, Friesner: OPLS3: A Force Field Providing Broad Coverage of Drug-like Small Molecules and Proteins. In: *J. Chem. Theory Comput.* 12 (2016), S. 281–296

[91] E, Kraepelin: Das senile und prasenile Irresein. In: *Psychiatrie, ein Lehrbuch fur Studierende und Arzte* (1910), S. 593–632

[92] ED, Eanes ; GG, Glennner: X-ray Diffraction Studies on Amyloid Filaments. In: *J. Histochem. Cytochem.* 16 (1968)

[93] EJ, Coulson ; K, Paliga ; K, Beyreuther ; CL, Masters: What the evolution of the amyloid protein precursor supergene family tells us about its function. In: *Neurochem. Int.* 36 (2000), S. 175–184

[94] Esler, William P. ; Stimson, Evelyn R. ; Jennings, Joan M. ; Vinters, Harry V. ; Ghilardi, Joseph R. ; Lee, Jonathan P. ; Mantyh, Patrick W. ; Maggio, John E.: Alzheimer's Disease Amyloid Propagation by a Template-Dependent Dock-Lock Mechanismâ[U+0080] . In: *Biochemistry* 39 (2000), Mai, Nr. 21, S. 6288–6295. – ISSN 0006–2960

[95] ET, Powers ; DL, Powers: The Kinetics of Nucleated Polymerizations at High Concentrations: Amyloid Fibril Formation Near and Above the "Supercritical Concentration". In: *Biophys. J.* 91 (2006)

[96] F, Chiti ; F, Taddei N B. ; C, Capanni ; M, Stefani ; G, Ramponi ; CM, Dobson: Kinetic partitioning of protein folding and aggregation. In: *Nat. Struct. Biol.* 9 (2002)

[97] F, Ferrone: Analysis of protein aggregation kinetics. In: *Methods Enzymol.* 309 (1999)

[98] F, Hasecke ; T, Miti ; C, Perez ; J, Barton ; D, Schölzel ; L, Gremer ; CSR, Grüning ; G, Matthews ; G, Meisl ; TPJ, Knowles: Origin of metastable oligomers and their effects on amyloid fibril self-assembly. In: *Chem. Sci.* 9 (2018)

[99] F, Jiang ; CY, Zhou ; YD, Wu: Residue-Specific Force Field Based on the Protein Coil Library. RSFF1: Modification of OPLS-AA/L. In: *J. Phys. Chem. B* 118 (2014), S. 6983–6998

[100] F, Olsson ; S, Schmidt ; V, Althoff ; LM, Munter ; S, Jin ; S, Rosqvist: Characterization of intermediate steps in amyloid beta (Abeta) production under near-native conditions. In: *J. Biol. Chem.* 289 (2014), S. 1540–1550

[101] Fede, Giuseppe D. ; Catania, Marcella ; Morbin, Michela ; Rossi, Giacomina ; Suardi, Silvia ; Mazzoleni, Giulia ; Merlin, Marco ; Giovagnoli, Anna R. ; Prioni, Sara ; Erbetta, Alessandra ; Falcone, Chiara ; Gobbi, Marco ; Colombo, Laura ; Bastone, Antonio ; Beeg, Marten ; Manzoni, Claudia ; Francescucci, Bruna ; Spagnoli, Alberto ; CantÃ[1], Laura ; Favero, Elena D. ; Levy, Efrat ; Salmona, Mario ; Tagliavini, Fabrizio: A Recessive Mutation in the APP Gene with Dominant-Negative Effect on Amyloidogenesis. In: *Science* 323 (2009), März, Nr. 5920, S. 1473–1477. – ISSN 0036–8075, 1095–9203

[102] Feenstra, K. A. ; Hess, Berk ; Berendsen, Herman J. C.: Improving efficiency of large time-scale molecular dynamics simulations of hydrogen-rich systems. In: *J. Comput. Chem.* 20 (1999), Nr. 8, S. 786–798. – ISSN 1096–987X

[103] Fezoui, Youcef ; Teplow, David B.: Kinetic studies of amyloid beta-protein fibril assembly. Differential effects of alpha-helix stabilization. In: *J. Biol. Chem.* 277 (2002), S. 36948–36954

[104] Finder, Verena H.: Alzheimer's disease: a general introduction and pathomechanism. In: *J. Alzheimer's Dis.* 22 (2010), Nr. s3, S. S5–S19

[105] Foderà, V ; F, Librizzi ; M, Groenning ; van de Weert M ; M, Leone: Secondary Nucleation and Accessible Surface in Insulin Amyloid Fibril Formation. In: *J. Phys. Chem. B* 112 (2008), S. 3853–3858

[106] Frigori, Rafael B. ; Barroso da Silva, Fernando L. ; Carvalho, Patrícia P. D. ; Alves, Nelson A.: Occurrence of Biased Conformations as Precursors of Assembly States in Fibril Elongation of Amyloid-β Fibril Variants: An In Silico Study. In: *J. Phys. Chem. B* 124 (2020), Apr, Nr. 14, S. 2798–2805. – ISSN 1520–6106

[107] Frisch, M. J. ; Trucks, G. W. ; Schlegel, H. B. ; Scuseria, G. E. ; Robb, M. A. ; Cheeseman, J. R. ; Scalmani, G. ; Barone, V. ; Mennucci, B. ; Petersson, G. A. ; Nakatsuji, H. ; Caricato, M. ; Li, X. ; Hratchian, H. P. ; Izmaylov, A. F. ; Bloino, J. ; Zheng, G. ; Sonnenberg, J. L. ; Hada, M. ; Ehara, M. ; Toyota, K. ; Fukuda, R. ; Hasegawa, J. ; Ishida, M. ; Nakajima, T. ; Honda, Y. ; Kitao, O. ; Nakai, H. ; Vreven, T. ; Montgomery, J. A. ; Peralta, J. E. ; Ogliaro, F. ; Bearpark, M. ; Heyd, J. J. ; Brothers, E. ; Kudin, K. N. ; Staroverov, V. N. ; Kobayashi, R. ; Normand, J. ; Raghavachari, K. ; Rendell, A. ; Burant, J. C. ; Iyengar, S. S. ; Tomasi, J. ; Cossi, M. ; Rega, N. ; Millam, J. M. ; Klene, M. ; Knox, J. E. ; Cross, J. B. ; Bakken, V. ; Adamo, C. ; Jaramillo, J. ; Gomperts, R. ; Stratmann, R. E. ; Yazyev, O. ; Austin, A. J. ; Cammi, R. ; Pomelli, C. ; Ochterski, J. W. ; Martin, R. L. ; Morokuma, K. ; Zakrzewski, V. G. ; Voth, G. A. ; Salvador, P. ; Dannenberg, J. J. ; Dapprich, S. ; Daniels, A. D. ; Farkas, Ö. ; Foresman, J. B. ; Ortiz, J. V. ; Cioslowski, J. ; Fox, D. J.: *Gaussian∼09 Revision E.01.* – Gaussian Inc. Wallingford CT 2009

[108] Frishman, D. ; Argos, P.: Knowledge-based secondary structure assignment. In: *Proteins: structure, function and genetics* 23 (1995), S. 566–579

[109] G, Ramachandran ; JB, Udgaonkar: Evidence for the existence of a secondary pathway for fibril growth during the aggregation of tau. In: *J. Mol. Biol.* 421 (2012), S. 296–314

[110] GA, Kaminski ; RA, Friesner ; J, Tirado-Rives ; WL, Jorgensen: Residue-Specific Force Field Based on Protein Coil Library. RSFF2: Modification of AMBER ff99SB. In: *J. Phys. Chem. B* 105 (2001), S. 6474–6487

[111] Gallardo, Rodrigo ; Ranson, Neil A. ; Radford, Sheena E.: Amyloid structures: much more than just a cross-β fold. In: *Curr. Opin. Struct. Biol.* 60 (2020), S. 7–16

[112] Gao, J ; Habibollazadeh, D ; Shao, L: A polarizable intermolecular potential function for simulation of liquid alcohols. In: *J. Phys. Chem.* 99 (1995), S. 16460–16467

[113] Gavezzotti, A: Molecular Aggregation: Structure analysis and molecular simulation of crystals and liquids. In: *Oxford University Press* (2007)

[114] Geerke, DP ; van Gunsteren, WF: On the calculation of atomic forces in classical simulation using the charge-on-spring method to explicitly treat electronic polarization. In: *J. Chem. Theory Comput.* 3 (2007), S. 2128–2137

[115] GG, Glenner ; CW, Wong: Alzheimer's disease and Down's syndrome: sharing of a unique cerebrovascular amyloid fibril protein. In: *Biochem. Biophys. Res. Commun.* 122 (1984)

[116] GG, Glenner ; CW, Wong: Alzheimer's disease: initial report of the purification and characterization of a novel cerebrovascular amyloid protein. In: *Biochem. Biophys. Res. Commun.* 120 (1984)

[117] GG, Glenner ; CW, Wong: Alzheimer's disease: initial report of the purification and characterization of a novel cerebrovascular amyloid protein. In: *Biochemical and Biophysical Research Communications* 425 (2012), S. 534–9

[118] GM, Torrie ; JP, Valleau: Nonphysical sampling distributions in Monte Carlo free-energy estimation: umbrella sampling. In: *J. Comput. Phys.* 23 (1977), S. 187–199

[119] Goldblatt, Greg ; Cilenti, Lucia ; Matos, Jason O. ; Lee, Briana ; Ciaffone, Nicholas ; Wang, Qing X. ; Tetard, Laurene ; Teter, Ken ; Tatulian, Suren A.: Unmodified and pyroglutamylated amyloid peptides form hypertoxic hetero-oligomers of unique secondary structure. In: *FEBS. J.* 284 (2017), Nr. 9, S. 1355–1369

[120] Granata, Daniele ; Baftizadeh, Fahimeh ; Habchi, Johnny ; Galvagnion, Celine ; De Simone, Alfonso ; Camilloni, Carlo ; Laio, Alessandro ; Vendruscolo, Michele: The inverted free energy landscape of an intrinsically disordered peptide by simulations and experiments. In: *Sci. Rep.* 5 (2015), Oct, Nr. 15449, S. 1–15. – ISSN 2045–2322

[121] Gremer, Lothar ; Schölzel, Daniel ; Schenk, Carla ; Reinartz, Elke ; Labahn, Jörg ; Ravelli, Raimond B. G. ; Tusche, Markus ; Lopez-Iglesias, Carmen ; Hoyer, Wolfgang ; Heise, Henrike ; Willbold, Dieter ; Schröder, Gunnar F.: Fibril structure of amyloid-β(1–42) by cryo–electron microscopy. In: *Science* 358 (2017), Oct, Nr. 6359, S. 116–119. – ISSN 0036–8075

[122] GS, Bloom: Amyloid-beta and tau: the trigger and bullet in Alzheimer disease pathogenesis. In: *JAMA Neurol.* 71 (2014), S. 505–508

[123] Guillot, B: A reappraisal of what we have learnt during three decades of computer simulations on water. In: *J. Mol. Liq.* 101 (2002), S. 219–260

[124] H, Liu ; D, Song ; H, Lu ; R, Luo ; HF, Chen: Intrinsically disordered protein-specific force field CHARMM36IDPSFF. In: *Chem. Biol. Drug Des.* 92 (2018), S. 1722−1735

[125] H, Liu ; D, Song ; Y, Zhang ; S, Yang ; R, Luo ; HF, Chen: Extensive tests and evaluation of the CHARMM36IDPSFF force field for intrinsically disordered proteins and folded proteins. In: *Phys. Chem. Chem. Phys.* 21 (2019), S. 21918−21931

[126] H, Meshkin ; F, Zhu: Thermodynamics of protein folding studied by umbrella sampling along a reaction coordinate of native contacts. In: *J. Chem. Theory. Comput.* 13 (2017), S. 2086–2097

[127] Haass, C ; Lemere, CA ; A Capell, M C. ; Seubert, P ; Schenk, D: The Swedish mutation causes early-onset Alzheimer's disease by beta-secretase cleavage within the secretory pathway. In: *Nat. Med.* 1 (1995), S. 1291–1296

[128] Halgren, TA ; Damm, W: Polarizable force fields. In: *Curr. Opin. Struct. Biol.* 11 (2001), S. 236–242

[129] Harigaya, Yasuo ; Saido, Takaomi C. ; Eckman, Christopher B. ; Prada, Cristian-Mihail ; Shoji, Mikio ; Younkina, Steven G.: Amyloid Protein Starting Pyroglutamate at Position 3 Is a Major Component of the Amyloid Deposits in the Alzheimer's Disease Brain. In: *Biochem. Biophys. Res. Commun.* 276 (2000), Nr. 2, S. 422–27

[130] He, Weilan ; Barrow, Colin J.: The Aâ 3-Pyroglutamyl and 11-Pyroglutamyl Peptides Found in Senile Plaque Have Greater â-Sheet Forming and Aggregation Propensities in Vitro than Full-Length Aâ. In: *Biochemistry.* 38 (1999), Nr. 33, S. 10871–10877

[131] He, Weilan ; Barrow, Colin J.: The Aβ 3-Pyroglutamyl and 11-Pyroglutamyl Peptides Found in Senile Plaque Have Greater β-Sheet Forming and Aggregation Propensities in Vitro than Full-Length Aβ. In: *Biochemistry* 38 (1999), Aug, Nr. 33, S. 10871–10877. – ISSN 0006–2960

[132] Hess, Berk ; Kutzner, Carsten ; van der Spoel, David ; Lindahl, Erik: GROMACS 4: Algorithms for highly efficient, load-balanced, and scalable molecular simulation. In: *J. Chem. Theory. Comput.* 4 (2008), März, Nr. 3, S. 435–447

[133] HJC, Berendsen ; JR, Grigera ; TP, Straatsma: The missing term in effective pair potentials. In: *J. Phys. Chem.* 91 (1987), S. 6269−6271

[134] Hornak, Viktor ; Abel, Robert ; Okur, Asim ; Strockbine, Bentley ; Roitberg, Adrian ; Simmerling, Carlos: Comparison of multiple Amber force fields and development of improved protein backbone parameters. In: *Proteins.* 65 (2006), S. 712–725

[135] Hovgaard, MB ; Dong, M ; Otzen, DE ; Besenbacher, F: Quartz crystal microbalance studies of multilayer glucagon fibrillation at the solid-liquid interface. In: *Biophys. J.* 93 (2007), S. 2162–2169

[136] Hu, Xiaoyan ; Crick, Scott L. ; Bu, Guojun ; Frieden, Carl ; Pappu, Rohit V. ; Lee, Jin-Moo: Amyloid seeds formed by cellular uptake, concentration, and aggregation of the amyloid-beta peptide. In: *Proc. Natl. Acad. Sci.* 106 (2009), Nr. 48, S. 20324–9

[137] Huang, Jing ; Rauscher, Sarah ; Nawrocki, Grzegorz ; Ran, Ting ; Feig, Michael ; de Groot, Bert L. ; Grubmüller, Helmut ; MacKerell Jr, Alexander D.: CHARMM36m: an improved force field for folded and intrinsically disordered proteins. In: *Nat. Methods* 14 (2017), Januar, Nr. 1, S. 71–73. – ISSN 1548–7091

[138] Hukushima, Koji ; Nemoto, Koji: Exchange Monte Carlo Method and Application to Spin Glass Simulations. In: *J. Phys. Soc. Jpn.* 65 (1996), S. 1604–1608

[139] Humphrey, William ; Dalke, Andrew ; Schulten, Klaus: VMD – Visual Molecular Dynamics. In: *Journal of Molecular Graphics* 14 (1996), S. 33–38

[140] HW, Horn ; WC, Swope ; JW, Pitera ; JD, Madura ; TJ, Dick ; T, Hura GL Head-Gordon: Development of an improved four-site water model for biomolecular simulations: TIP4P-Ew. In: *J. Chem. Phys.* 120 (2004), S. 9665−9678

[141] J, Homola ; SS, Yee ; G, Gauglitz: Surface plasmon resonance sensors: Review. In: *Sens. Actuators B Chem.* 54 (1999), S. 3–15

[142] J, Huang ; AD, MacKerell: CHARMM36 all-atom additive protein force field: Validation based on comparison to NMR data. In: *J. Comput. Chem.* 34 (2013), S. 2135–2145

[143] J, Huang ; S, Rauscher ; G, Nawrocki ; T, Ran ; M, Feig ; de Groot BL ; H, Grubmuller ; AD, MacKerell: CHARMM36m: an improved force field for folded and intrinsically disordered proteins. In: *Nat. Methods* 14 (2017), S. 71–73

[144] J, Maupetit ; P, Tuffery ; P, Derreumaux: A coarse-grained protein force field for folding and structure prediction. In: *Proteins.* 69 (2007), S. 394−408

[145] J, Nunan ; DH, Small: Regulation of APP cleavage by alpha-, beta- and gamma-secretases. In: *FEBS. Lett.* 483 (2000), S. 6–10

[146] J, Zhang ; H, Gong: Frontier Expansion Sampling: A Method to Accelerate Conformational Search by Identifying Novel Seed Structures for Restart. In: *J. Chem. Theory Comput.* 16 (2020), S. 4813−4821

[147] JA, De F. ; J, Benjamins ; FA, Veer: Ellipsometry as a tool to study the adsorption behavior of synthetic and biopolymers at the air-water interface. In: *Biopolymers* 17 (1978), S. 1759–1772

[148] JA, Duce ; A, Tsatsanis ; MA, Cater ; SA, James ; E, Robb ; K, Wikhe: Iron-export ferroxidase activity of beta-amyloid precursor protein is inhibited by Zinc in Alzheimer's disease. In: *Cell* 142 (2010), S. 857–867

[149] JA, Lemkul ; DR, Bevan: Assessing the stability of Alzheimer's amyloid protofibrils using molecular dynamics. In: *J. Phys. Chem. B* 114 (2010), S. 1652–1660

[150] Jawhar, Sadim ; Wirths, Oliver ; Bayer, Thomas A.: Pyroglutamate amyloid-(A): a hatchet man in Alzheimer disease. In: *J. Biol. Chem.* 286 (2011), Nr. 45, S. 38825–32

[151] Jawhar, Sadim ; Wirths, Oliver ; Bayer, Thomas A.: Pyroglutamate Amyloid-(A): A Hatchet Man in Alzheimer Disease. In: *J. Biol. Chem.* 286 (2011), November, Nr. 45, S. 38825–38832. – ISSN 0021–9258, 1083–351X

[152] JD, Harper ; PT, Lansbury: Models of Amyloid Seeding in Alzheimer's Disease and Scrapie: Mechanistic Truths and Physiological Consequences of the Time-Dependent Solubility of Amyloid Proteins. In: *Annu. Rev. Biochem.* 66 (1997)

[153] JD, Schmit ; K, Ghosh ; K, Dill: What Drives Amyloid Molecules to Assemble into Oligomers and Fibrils? In: *Biophys. J.* 100 (2011)

[154] Jedlovsky, P ; Richardi, J: Comparison of different water models from ambient to supercritical conditions: a Monte Carlo simulation and molecular Ornstein-Zernike study. In: *J. Chem. Phys.* 110 (1999), S. 8019–8031

[155] Jonsson, Thorlakur ; Atwal, Jasvinder K. ; Steinberg, Stacy ; Snaedal, Jon ; Jonsson, Palmi V. ; Bjornsson, Sigurbjorn ; Stefansson, Hreinn ; Sulem, Patrick ; Gudbjartsson, Daniel ; Maloney, Janice ; Hoyte, Kwame ; Gustafson, Amy ; Liu, Yichin ; Lu, Yanmei ; Bhangale, Tushar ; Graham, Robert R. ; Huttenlocher, Johanna ; Bjornsdottir, Gyda ; Andreassen, Ole A. ; Jönsson, Erik G. ; Palotie, Aarno ; Behrens, Timothy W. ; Magnusson, Olafur T. ; Kong, Augustine ; Thorsteinsdottir, Unnur ; Watts, Ryan J. ; Stefansson, Kari: A mutation in APP protects against Alzheimer's disease and age-related cognitive decline. In: *Nature.* 488 (2012), S. 96–99

[156] Jorgensen, William L. ; Chandrasekhar, Jayaraman ; Madura, Jeffry D.: Comparison of simple potential functions for simulating liquid water. In: *J. Chem. Phys.* 79 (1983), S. 126

[157] Jorgensen, WL ; Jensen, KP ; Alexandrova, AN: Polarization effects for hydrogen- bonded complexes of substituted phenols with water and chloride ion. In: *J. Chem. Theory Comput.* 3 (2007), S. 1987–1992

[158] Jorgensen, WL ; Tirado-Rives, J: Potential energy functions for atomic-level simulations of water and organic and bio-molecular systems. In: *Proc. Natl. Acad. Sci. USA* 102 (2005), S. 6665–6670

[159] JT, Huse ; K, Liu ; DS, Pijak ; D, Carlin ; VM, Lee ; RW, Doms: β-Secretase processing in the trans-Golgi network preferentially generates truncated amyloid species that accumulate in Alzheimer's disease brain. In: *J. Biol. Chem.* 277 (2002)

[160] Jülich Supercomputing Centre: JURECA: Modular supercomputer at Jülich Supercomputing Centre. In: *Journal of large-scale research facilities* 4 (2018), Nr. A132

[161] K, Baranger ; AE, Bonnet ; SD, Girard ; JM, Paumier ; L, García-González ; W, Elmanaa ; A, Bernard ; E, Charrat ; D, Stephan ; C, Bauer ; K, Moschke ; SF, Lichtenthaler ; FS, Roman ; F, Checler ; M, Khrestchatisky ; S, Rivera: MT5–MMP promotes Alzheimer's pathogenesis in the frontal cortex of 5XFAD mice and APP trafficking in vitro. In: *Front. Mol. Neurosci.* 9 (2016)

[162] K, Hasegawa ; K, Ono ; M, Yamada ; H, Naiki: Kinetic modeling and determination of reaction constants of Alzheimer's β-amyloid [U+FB01]bril extension and dissociation using surface plasmon resonance. In: *Biochemistry* 41 (2002), S. 13489–13498

[163] K, Ostermeir ; M, Zacharias: Accelerated flexible protein-ligand docking using Hamiltonian replica exchange with a repulsive biasing potential. In: *PLoS ONE.* 12 (2017), S. 1–17

[164] K, Takano ; J, Funahashi ; K, Yutani: The stability and folding process of amyloidogenic mutant human lysozymes. In: *Eur. J. Biochem.* 268 (2001)

[165] K, Wang ; JD, Chodera ; Y, Yang ; MR, Shirts: Identifying ligand binding sites and poses using GPU-accelerated Hamiltonian replica exchange molecular dynamics. In: *J. Comput. Aid. Mol. Des.* 27 (2013), S. 989–1007

[166] KA, Ball ; AH, Phillips ; PS, Nerenberg ; NL, Fawzi ; DE, Wemmer ; T, Head-Gordon: Homogeneous and heterogeneous tertiary structure ensembles of amyloid-β peptides. In: *Biochemistry.* 50 (2011), S. 7612−7628

[167] Kabsch, W. ; Sander, C.: Dictionary of protein secondary structure: pattern recognition of hydrogen-bonded and geometrical features. In: *Biopolymers* 22 (1983), Dec, Nr. 12, S. 2577–2637. – ISSN 0006–3525

[168] Kaminski, George A. ; Friesner, Richard A. ; Tirado-Rives, Julian ; Jorgensen, William L.: Evaluation and Reparametrization of the OPLS-AA Force Field for Proteins via Comparison with Accurate Quantum Chemical Calculations on Peptides. In: *J. Phys. Chem. B* 105 (2001), Juli, Nr. 28, S. 6474–6487

[169] KE, Routledge ; GG, Tartaglia ; GW, Platt ; M, Vendruscolo ; SE, Radford: Competition between Intramolecular and Intermolecular Interactions in an Amyloid-Forming Protein. In: *J. Mol. Biol.* 389 (2009)

[170] Kirkitadze, M D. ; Condron, M M. ; Teplow, D B.: Identification and characterization of key kinetic intermediates in amyloid beta-protein fibrillogenesis. In: *J. Mol. Biol.* 312 (2001), S. 1103–1119

[171] KK, Turoverov ; IM, Kuznetsova ; VN, Uversky: The protein kingdom extended: Ordered and intrinsically disordered proteins, their folding, supramolecular complex formation, and aggregation. In: *Prog. Biophys. Mol. Biol.* 102 (2010)

[172] Knowles, TPJ ; Vendruscolo, M ; Dobson, CM: The amyloid state and its association with protein misfolding diseases. In: *Nat. Rev. Mol. Cell. Biol.* 15 (2014), S. 384–396

[173] Knowles, TPJ ; Waudby, CA ; Devlin, GL ; Cohen, SIA ; Aguzzi, A ; Vendruscolo, M ; Terentjev, EM ; Welland, ME ; Dobson, CM: An analytical solution to the kinetics of breakable filament assembly. In: *Science* 326 (2007), S. 1533–1537

[174] Kotarek, JA ; Johnson, KC ; Moss, MA: Quartz crystal microbalance analysis of growth kinetics for aggregation intermediates of the amyloid-beta protein. In: *Anal. Biochem.* 378 (2008), S. 15–24

[175] Kretschman, Erwin: The determination of optical constants of metals by excitation of surface plasma vibrations. In: *J. Phys. A* 241 (1971), S. 313–324

[176] Krupa, Pawel ; Quoc Huy, Pham D. ; Li, Mai S.: Properties of monomeric Aβ42 probed by different sampling methods and force fields: Role of energy components. In: *J. Chem. Phys.* 151 (2019), Aug, Nr. 5, S. 055101. – ISSN 0021–9606

[177] Kumar, Shankar ; Rosenberg, John M. ; Bouzida, Djamal ; Swendsen, Robert H. ; Kollman, Peter A.: The weighted histogram analysis method for free-energy calculations on biomolecules. I. The method. In: *J. Comput. Chem.* 13 (1992), Oktober, Nr. 8, S. 1011–1021. – ISSN 1096–987X

[178] L, Bonar ; AS, Cohen ; MM, Skinner: Characterization of the Amyloid Fibril as a Cross- Protein. In: *Exp. Biol. Med.* 131 (1969)

[179] L, Bradshaw: Understanding piezoelectric quartz crystals. In: *RF time and frequency* 8 (2000), S. 50–58

[180] Laio, Alessandro ; Parrinello, Michele: Escaping free-energy minima. In: *Proc. Natl. Acad. Sci. USA* 99 (2002)

[181] Lamoureux, G ; Roux, B: Modeling induced polarization with classical Drude oscillators: Theory and molecular dynamics simulation algorithm. In: *J. Chem. Phys.* 119 (2003), S. 3025–3039

[182] Liao, Qinghua ; Kulkarni, Yashraj ; Sengupta, Ushnish ; Petrović, Dušan ; Mulholland, Adrian J. ; van der Kamp, Marc W. ; Strodel, Birgit ; Kamerlin, Shina Caroline L.: Loop Motion in Triosephosphate Isomerase Is Not a Simple Open and Shut Case. In: *J. Am. Chem. Soc.* 140 (2018), S. 15889–15903

[183] Lim, Kwang H. ; Collver, Hilary H. ; Le, Yen T. H. ; Nagchowdhuri, Partha ; Kenney, John M. ; Lim, Kwang H. ; Collver, Hilary H. ; Le, Yen T. H. ; Nagchowdhuri, Partha ; Kenney, John M.: Characterizations of Distinct Amyloidogenic Conformations of the Abeta (1-40) and (1-42) Peptides. In: *Biochem. Biophys. Res. Commun.* 353 (2007), Feb, Nr. 2, S. 443–449. – ISSN 0006–291X

[184] Lincoff, James ; Sasmal, Sukanya ; Head-Gordon, Teresa: The combined force field-sampling problem in simulations of disordered amyloid-β peptides. In: *J. Chem. Phys.* 150 (2019), Mar, Nr. 10, S. 104108. – ISSN 0021–9606

[185] Lindorff-Larsen, Kresten ; Piana, Stefano ; Palmo, Kim ; Maragakis, Paul ; Klepeis, John L. ; Dror, Ron O. ; Shaw, David E.: Improved side-chain torsion potentials for the Amber ff99SB protein force field. In: *Proteins* 78 (2010), Juni, Nr. 8, S. 1950–1958. – ISSN 1097–0134

[186] Linse, Sara: Monomer-dependent secondary nucleation in amyloid formation. In: *Biophys. Rev.* 9 (2017), S. 329–338

[187] Lührs, Thorsten ; Ritter, Christiane ; Adrian, Marc ; Riek-Loher, Dominique ; Bohrmann, Bernd ; Döbeli, Heinz ; Schubert, David ; Riek, Roland: 3D structure of Alzheimer's amyloid-β(1-42) fibrils. In: *Proc. Natl. Acad. Sci.* 102 (2005), November, Nr. 48, S. 17342–17347. – ISSN 0027–8424, 1091–6490

[188] Löhr, Thomas ; Kohlhoff, Kai ; Heller, Gabriella T. ; Camilloni, Carlo ; Vendruscolo, Michele: A kinetic ensemble of the Alzheimer's Aβ peptide. In: *Nat. Comp. Sci.* 1 (2021), S. 71–78

[189] M, Carballo-Pacheco ; AE, Ismail ; B, Strodel: On the Applicability of Force Fields To Study the Aggregation of Amyloidogenic Peptides Using Molecular Dynamics Simulations. In: *J. Chem. Theory Comput.* 14 (2018), S. 6063−6075

[190] M, Rodahl ; B, Kasemo: A simple setup to simultaneously mea- sure the resonant frequency and the absolute dissipation factor of a quartz crystal microbalance. In: *Rev. Sci. Instr.* 67 (1996), S. 3238–3241

[191] M, Rodahl ; F, Höök ; A, Krozer ; P, Brzezinski ; B, Kasemo: Quartz crystal microbalance set up for frequency and Q-factor mea- surements in gaseous and liquids environments. In: *Rev. Sci. Inst.* 66 (1995), S. 3924–3930

[192] M, Sunde ; C, Blake: The Structure of Amyloid Fibrils by Electron Microscopy and X-Ray Diffraction. In: *Adv. Protein Chem.* 50 (1997)

[193] M, Sunde ; LC, Serpell ; M, Bartlam ; PE, Fraser ; MB, Pepys ; CC, Blake: Common core structure of amyloid fibrils by synchrotron X-ray diffraction. In: *J. Mol. Biol.* 273 (1997)

[194] M, Vendruscolo ; E, Paci ; M, Karplus ; CM, Dobson: Structures and relative free energies of partially folded states of proteins. In: *Proc. Natl. Acad. Sci. USA* 100 (2003)

[195] M, Willem ; S, Tahirovic ; MA, Busche ; SV, Ovsepian ; M, Chafai ; S, Kootar ; D, Hornburg ; LD, Evans ; S, Moore ; A, Daria ; H, Hampel ; V, Müller ; C, Giudici ; B, Nuscher ; A, Wenninger-Weinzierl: η-Secretase processing of APP inhibits neuronal activity in the hippocampus. In: *Nature* 526 (2015)

[196] MA, González: Force fields and molecular dynamics simulations. In: *Collection SFN* 12 (2011), S. 169–200

[197] MA, Grant ; ND, Lazo ; A, Lomakin ; MM, Condron ; H, Arai ; G, Yamin ; AC, Rigby ; DB, Teplow: Familial Alzheimer's disease mutations alter the stability of the amyloid beta-protein monomer folding nucleus. In: *Proc. Natl. Acad. Sci. USA* 104 (2007)

[198] MA, Watzky ; AM, Morris ; ED, Ross ; RG, Finke: Fitting Yeast and Mammalian Prion Aggregation Kinetic Data with the Finke−Watzky Two-Step Model of Nucleation and Autocatalytic Growth. In: *Biochemistry* 47 (2008)

[199] Mackerell, AD: CHARMM FF parameters. In: *http://mackerell.umaryland.edu/CHARMM$_f$f$_p$arams.html*

[200] Maloney, Janice A. ; Bainbridge, Travis ; Gustafson, Amy ; Zhang, Shuo ; Kyauk, Roxanne ; Steiner, Pascal ; van der Brug, Marcel ; Liu, Yichin ; Ernst, James A. ; Watts, Ryan J. ; Atwal, Jasvinder K.: Molecular mechanisms of Alzheimer disease protection by the A673T allele of amyloid precursor protein. In: *J. Biol. Chem.* 289 (2014), S. 30990–31000

[201] Massi, F. ; Straub, J. E.: Energy landscape theory for Alzheimer's amyloid beta-peptide fibril elongation. In: *Proteins* 42 (2001), Feb, Nr. 2, S. 217–229. – ISSN 0887–3585

[202] Matos, Jason O. ; Goldblatt, Greg ; Jeon, Jaekyun ; Chen, Bo ; Tatulian, Suren A.: Pyroglutamylated amyloid- peptide reverses cross -sheets by a prion-like mechanism. In: *J. Phys. Chem. B.* 118 (2014), Nr. 21, S. 5637–43

[203] Mayo, SL ; Olafson, BD ; III, WA G.: Dreiding: A generic force field for molecular simulations. In: *J. Phys. Chem.* 94 (1990), S. 8897–8909

[204] Mazzitelli, S. ; Filipello, F. ; Rasile, M. ; Lauranzano, E. ; Starvaggi-Cucuzza, C. ; Tamborini, M. ; Pozzi, D. ; Barajon, I. ; Giorgino, T. ; Natalello, A. ; Matteoli, M.: Amyloid-β 1-24 C-terminal truncated fragment promotes amyloid-β 1-42 aggregate formation in the healthy brain. In: *Acta Neuropathol Commun.* 4(1):110 (2016)

[205] McGibbon, Robert T. ; Beauchamp, Kyle A. ; Harrigan, Matthew P. ; Klein, Christoph ; Swails, Jason M. ; Hernández, Carlos X. ; Schwantes, Christian R. ; Wang, Lee-Ping ; Lane, Thomas J. ; Pande, Vijay S.: MDTraj: A Modern Open Library for the Analysis of Molecular Dynamics Trajectories. In: *Biophysical Journal* 109 (2015), Nr. 8, S. 1528 – 1532

[206] Meisl, Georg ; Hidari, Eric ; Allinson, Kieren ; Rittman, Timothy ; DeVos, Sarah L. ; Sanchez, Justin S. ; Xu, Catherine K. ; Duff, Karen E. ; Johnson, Keith A. ; Rowe, James B. ; Hyman, Bradley T. ; Knowles, Tuomas P J. ; Klenerman, David: In vivo rate-determining steps of tau seed accumulation in Alzheimer's disease. In: *Sci. Adv.* 7 (2021), S. eabh1448

[207] Meisl, Georg ; Yang, Xiaoting ; Hellstrand, Erik ; Frohm, Birgitta ; Kirkegaard, Julius B. ; Cohen, Samuel I A. ; Dobson, Christopher M. ; Linse, Sara ; Knowles, Tuomas P J.: Differences in nucleation behavior underlie the contrasting aggregation kinetics of the Aβ40 and Aβ42 peptides. In: *Proc. Natl. Acad. Sci. USA* 111 (2014), S. 9384–9389

[208] Meng, Fanjie ; Bellaiche, Mathias M. J. ; Kim, Jae-Yeol ; Zerze, Gül H. ; Best, Robert B. ; Chung, Hoi S.: Highly Disordered Amyloid-β Monomer Probed by Single-Molecule FRET and MD Simulation. In: *Biophys. J.* 114 (2018), Feb, Nr. 4, S. 870–884. – ISSN 1542–0086

[209] MI, Ivanova ; MJ, Thompson ; D, Eisenberg: A systematic screen of β2-microglobulin and insulin for amyloid-like segments. In: *Proc. Natl. Acad. Sci. USA* 103 (2006)

[210] Michaels, Thomas C. T. ; Buell, Alexander K. ; Terentjev, Eugene M. ; Knowles, Tuomas P. J.: Quantitative Analysis of Diffusive Reactions at the Solid−Liquid Interface in Finite Systems. In: *J. Phys. Chem. Lett.* 5 (2014), S. 695−–699

[211] Mitchell, PJ ; Fincham, D: Shell model simulations by adiabatic dynamics. In: *J. Phys.: Condens. Matter* 5 (1993), S. 1031–1038

[212] Mittag, Judith J. ; Milani, Silvia ; Walsh, Dominic M. ; Rädler, Joachim O. ; McManus, Jennifer J.: Simultaneous measurement of a range of particle sizes during Aβ1–42 fibrillogenesis quantified using fluorescence correlation spectroscopy. In: *Biochem. Biophys. Res. Commun.* 448 (2014), May, Nr. 2, S. 195–199. – ISSN 0006–291X

[213] MJ, Cannon ; AD, Williams ; R, Wetzel ; DG, Myszka: Kinetic analysis of beta-amyloid [U+FB01]bril elongation. In: *Anal. Biochem.* 328 (2004), S. 67–75

[214] MP, Luitz ; M, Zacharias: Protein-ligand docking using Hamiltonian replica exchange simulations with soft core potentials. In: *J. Chem. Inf. Model.* 54 (2014), S. 1669–1675

[215] MS, Lee ; MA, Olson: Calculation of absolute protein-ligand binding affinity using path and endpoint approaches. In: *Biophys. J.* 90 (2006), S. 864–877

[216] MU, Rahman ; AU, Rehman ; H, Liu ; HF, Chen: Comparison and Evaluation of Force Fields for Intrinsically Disordered Proteins. In: *J. Chem. Inf. Model.* 60 (2020), S. 4912−4923

[217] Nag, Suman ; Sarkar, Bidyut ; Bandyopadhyay, Arkarup ; Sahoo, Bankanidhi ; Sreenivasan, Varun K. A. ; Kombrabail, Mamata ; Muralidharan, Chandrakesan ; Maiti, Sudipta: Nature of the Amyloid-β Monomer and the Monomer-Oligomer Equilibrium. In: *J. Biol. Chem.* 286 (2011), Apr, Nr. 16, S. 13827–13833. – ISSN 0021–9258

[218] Nasica-Labouze, Jessica ; Nguyen, Phuong H. ; Sterpone, Fabio ; Berthoumieu, Olivia ; Buchete, Nicolae-Viorel ; Coté, Sébastien ; De Simone, Alfonso ; Doig, Andrew J. ; Faller, Peter ; Garcia, Angel ; Laio, Alessandro ; Li, Mai S. ; Melchionna, Simone ; Mousseau, Normand ; Mu, Yuguang ; Paravastu, Anant ; Pasquali, Samuela ; Rosenman, David J. ; Strodel, Birgit ; Tarus, Bogdan ; Viles, John H. ; Zhang, Tong ; Wang, Chunyu ; Derreumaux, Philippe: Amyloid β Protein and Alzheimer's Disease: When Computer Simulations Complement Experimental Studies. In: *Chem. Rev.* 115 (2015), May, Nr. 9, S. 3518–3563. – ISSN 0009–2665

[219] Nosé, Shuichi ; Klein, M. L.: Constant pressure molecular dynamics for molecular systems. In: *Mol. Phys.* 50 (1983), Dec, Nr. 5, S. 1055–1076. – ISSN 0026–8976

[220] Novo, Mercedes ; Freire, Sonia ; Al-Soufi, Wajih: Critical aggregation concentration for the formation of early Amyloid-β (1–42) oligomers. In: *Sci. Rep.* 8 (2018), Jan, Nr. 1783, S. 1–8. – ISSN 2045–2322

[221] Nussbaum, Justin M. ; Schilling, Stephan ; Cynis, Holger ; Silva, Antonia ; Swanson, Eric ; Wangsanut, Tanaporn ; Tayler, Kaycie ; Wiltgen, Brian ; Hatami, Asa ; Rönicke, Raik ; Reymann, Klaus ; Hutter-Paier, Birgit ; Alexandru,

Anca ; Jagla, Wolfgang ; Graubner, Sigrid ; Glabe, Charles G. ; Demuth, Hans-Ulrich ; Bloom, George S.: Prion-like behaviour and tau-dependent cytotoxicity of pyroglutamylated amyloid-. In: *Nature.* 485 (2012), Nr. 7400, S. 651–5

[222] Nygaard, Mads ; Kragelund, Birthe B. ; Papaleo, Elena ; Lindorff-Larsen, Kresten ; Nygaard, Mads ; Kragelund, Birthe B. ; Papaleo, Elena ; Lindorff-Larsen, Kresten: An Efficient Method for Estimating the Hydrodynamic Radius of Disordered Protein Conformations. In: *Biophys. J.* 113 (2017), Aug, Nr. 3, S. 550–557. – ISSN 1542–0086

[223] Ono, Kenjiro ; Condron, Margaret M. ; Teplow, David B.: Structureâ[U+0080][U+0093]neurotoxicity relationships of amyloid β-protein oligomers. In: *Proc. Natl. Acad. Sci.* 106 (2009), September, Nr. 35, S. 14745–14750. – ISSN 0027–8424, 1091–6490

[224] Ono, Kenjiro ; Condron, Margaret M. ; Teplow, David B.: Effects of the English (H6R) and Tottori (D7N) familial Alzheimer disease mutations on amyloid beta-protein assembly and toxicity. In: *J. Biol. Chem.* 285 (2010), S. 23186−23197

[225] Oostenbrink, C ; Villa, A ; Mark, AE ; van Gunsteren, WF: A biomolecular force field based on the free enthalpy of hydration and solvation: the GROMOS force-field parameter sets 53A5 and 53A6. In: *J. Comput. Chem.* 25 (2004), S. 1656–1676

[226] P, Arosio ; TPJ, Knowles ; S, Linse: On the lag phase in amyloid fibril formation. In: *Phys. Chem. Chem. Phys.* 17 (2015)

[227] P, Marinelli ; S, Navarro ; M, Baño-Polo ; B, Morel ; R, Graña-Montes ; A, Sabe ; F, Canals ; MR, Fernandez ; F, Conejero-Lara ; S, Ventura: Global Protein Stabilization Does Not Suffice to Prevent Amyloid Fibril Formation. In: *ACS. Chem. Biol.* 13 (2018), S. 2094–2105

[228] P, Robustelli ; S, Piana ; DE, Shaw: Developing a molecular dynamics force field for both folded and disordered protein states. In: *Proc. Natl. Acad. Sci. USA* 115 (2018), S. E4758−E4766

[229] Palop, Jorge J. ; Mucke, Lennart: Epilepsy and cognitive impairments in Alzheimer disease. In: *Arch Neurol.* 66 (2009), Nr. 4, S. 435–40

[230] Parrinello, M. ; Rahman, A.: Polymorphic transitions in single crystals: A new molecular dynamics method. In: *J. Appl. Phys.* 52 (1981), Dezember, Nr. 12, S. 7182–7190. – ISSN 0021–8979

[231] Patel, S ; Jr, AD M. ; ; III, CL B.: CHARMM fluctuating charge force field for proteins: I. Parameterization and application to bulk organic liquid simulations. In: *J. Comput. Chem.* 25 (2004), S. 1–15

[232] Paton, RS ; Goodman, JM: Hydrogen bonding and π-stacking: How reliable are force fields? A critical evaluation of force field descriptions of non-bonded interactions. In: *J. Chem. Inf. Model* 49 (2009), S. 944–955

[233] Paul, Arghadwip ; Samantray, Suman ; Anteghini, Marco ; Khaled, Mohammed ; Strodel, Birgit: Thermodynamics and kinetics of the amyloid-β peptide revealed by Markov state models based on MD data in agreement with experiment. In: *Chem. Sci.* 12 (2021), S. 6652–6669

[234] Peelaerts, W ; Bousset, L ; der Perren, A V. ; Moskalyuk, A ; Pulizzi, R ; Giugliano, M ; den Haute, C V. ; Melki, R ; Baekelandt, V: α-Synuclein strains cause distinct synucleinopathies after local and systemic administration. In: *Nature.* 522 (2015), S. 340–344

[235] Petkova, Aneta T. ; Leapman, Richard D. ; Guo, Zhihong ; Yau, Wai-Ming ; Mattson, Mark P. ; Tycko, Robert: Self-propagating, molecular-level polymorphism in Alzheimer's beta-amyloid fibrils. In: *Science.* 307

[236] PH, Nguyen ; Y, Okamoto ; PJ, Derreumaux: Simulated tempering with fast on-the-fly weight determination. In: *J. Chem. Phys.* 138 (2013), S. 61–102

[237] Piana, Stefano ; Lindorff-Larsen, Kresten ; Shaw, David E.: How Robust Are Protein Folding Simulations with Respect to Force Field Parameterization? In: *Biophys. J.* 100 (2011), April, Nr. 9, S. L47–L49. – ISSN 0006–3495

[238] PJ, Kahle ; B, De S.: Attack on amyloid. In: *EMBO. Rep.* 4 (2003), S. 747–751

[239] PR, Turner ; K, O'Connor ; WP, Tate ; WC, Abraham: Roles of amyloid precursor protein and its fragments in regulating neural activity, plasticity and memory. In: *Prog. Neurobiol.* 70 (2003), S. 1–32

[240] Price, DJ ; III, CL B.: Modern protein force fields behave comparably in molecular dynamics simulations. In: *J. Comput. Chem.* 23 (2002), S. 1045–1057

[241] PS, Nerenberg ; B, Jo ; C, So ; A, Tripathy ; T, Head-Gordon: Optimizing Solute-Water van der Waals Interactions To Reproduce Solvation Free Energies. In: *J. Phys. Chem. B* 116 (2012), S. 4524−4534

[242] R, Harada ; A, Kitao: Parallel cascade selection molecular dynamics (PaCS-MD) to generate conformational transition pathway. In: *J. Chem. Phys.* 139 (2013), S. 035–103

[243] R, Harada ; A, Kitao: Nontargeted Parallel Cascade Selection Molecular Dynamics for Enhancing the Conformational Sampling of Proteins. In: *J. Chem. Theory Comput.* 11 (2015), S. 5493−5502

[244] R, Harada ; K, Yamaguchi ; Y, Shigeta: Enhanced Conformational Sampling Method Based on Anomaly Detection Parallel Cascade Selection Molecular Dynamics: ad-PaCS-MD. In: *J. Chem. Theory Comput.* 16 (2020), S. 6716−6725

[245] R, Harada ; V, Sladek ; Y, Shigeta: Nontargeted Parallel Cascade Selection Molecular Dynamics Using Time-Localized Prediction of Conformational Transitions in Protein Dynamics. In: *J. Chem. Theory Comput.* 15 (2019), S. 5144−5153

[246] R, Harada ; Y, Shigeta: Efficient Conformational Search Based on Structural Dissimilarity Sampling: Applications for Reproducing Structural Transitions of Proteins. In: *J. Chem. Theory Comput.* 13 (2017), S. 1411−1423

[247] R, Harada ; Y, Shigeta: Self-Avoiding Conformational Sampling Based on Histories of Past Conformational Searches. In: *J. Chem. Inf. Model.* 57 (2017), S. 3070−3078

[248] R, Hosoda ; TC, Saido ; L, Otvos ; Jr ; T, Arai ; DM, Mann ; VM, Lee ; JQ, Trojanowski ; T, Iwatsubo: Quantification of modified amyloid β peptides in Alzheimer disease and Down syndrome brains. In: *J. Neuropathol. Exp. Neurol.* 57 (1998), S. 1089 –1095

[249] R, Kodali ; R, Wetzel: Polymorphism in the intermediates and products of amyloid assembly. In: *Curr. Opin. Struct. Biol.* 17 (2007)

[250] R, Laghaei ; N, Mousseau ; G, Wei: Effect of the disulfide bond on the monomeric structure of human amylin studied by combined Hamiltonian and temperature replica exchange molecular dynamics simulations. In: *J. Phys. Chem. B.* 114 (2010), S. 7071–7077

[251] R, Laghaei ; N, Mousseau ; G, Wei: Structure and thermodynamics of amylin dimer studied by Hamiltonian-temperature replica exchange molecular dynamics simulations. In: *J. Phys. Chem. B.* 115 (2011), S. 3146–3154

[252] R, Nelson ; D, Eisenberg: Recent atomic models of amyloid fibril structure. In: *Curr. Opin. Struct. Biol.* 16 (2006)

[253] R, Qi ; Y, Luo ; G, Wei ; R, Nussinov ; B, Ma: Aβ "stretching-and-packing" cross-seeding mechanism can trigger tau protein aggregation. In: *J. Phys. Chem. Lett.* 6 (2015), Nr. 16, S. 3276–3282

[254] R, Vassar ; BD, Bennett ; S, Babu-Khan ; S, Kahn ; EA, Mendiaz ; P, Denis ; DB, Teplow ; S, Ross ; P, Amarante ; R, Loeloff ; Y, Luo ; S, Fisher ; J, Fuller ; S, Edenson ; J, Lile: β-Secretase cleavage of Alzheimer's amyloid precursor protein by the transmembrane aspartic protease BACE. In: *Science* 286 (1999)

[255] Rappe, AK ; Casewit, CJ ; Colwell, KS ; III, WA G. ; Skiff, WM: UFF, a full periodic table force field for molecular mechanics and molecular dynamics simulations. In: *J. Am. Chem. Soc.* 114 (1992), S. 10024–10035

[256] RB, Best ; G, Hummer: Optimized Molecular Dynamics Force Fields Applied to the Helix-Coil Transition of Polypeptides. In: *J. Phys. Chem. B* 113 (2009), S. 9004–9015

[257] RB, Best ; WW, Zheng ; J, Mittal: Balanced Protein-Water Interactions Improve Properties of Disordered Proteins and Non-Specific Protein Association. In: *J. Chem. Theory Comput.* 10 (2014), S. 5113−5124

[258] Rick, SW ; Stuart, SJ ; Berne, BJ: Dynamical fluctuating charge force fields: Application to liquid water. In: *J. Chem. Phys.* 101 (1994), S. 6141–6156

[259] RL, Isaacson ; AG, Weeds ; AR, Fersht: Equilibria and kinetics of folding of gelsolin domain 2 and mutants involved in familial amyloidosis-Finnish type. In: *Proc. Natl. Acad. Sci. USA* 96 (1999)

[260] Roche, Julien ; Shen, Yang ; Lee, Jung H. ; Ying, Jinfa ; Bax, Ad: Monomeric Aβ(1-40) and Aβ(1-42) Peptides in Solution Adopt Very Similar Ramachandran Map Distributions That Closely Resemble Random Coil. In: *Biochemistry.* 55 (2016), S. 762–775

[261] Roche, Julien ; Shen, Yang ; Lee, Jung H. ; Ying, Jinfa ; Bax, Ad: Monomeric Aβ1–40 and Aβ1–42 Peptides in Solution Adopt Very Similar Ramachandran. In: *Biochemistry* 55 (2016), Feb, Nr. 5, S. 762

[262] Rosenman, David J. ; Connors, Christopher R. ; Chen, Wen ; Wang, Chunyu ; García, Angel E.: Aβ Monomers Transiently Sample Oligomer and Fibril-Like Configurations: Ensemble Characterization Using a Combined MD/NMR Approach. In: *J. Mol. Biol.* 425 (2013), Sep, Nr. 18, S. 3338–3359. – ISSN 0022–2836

[263] Ruiz-Riquelme, A. ; Mao, A. ; Barghash, M.M. ; Lau, H.H.C. ; Stuart, E. ; Kovacs, G.G. ; Nilsson, K.P.R. ; Fraser, P.E. ; Schmitt-Ulms, G. ; Watts, J.C.: Aβ43 aggregates exhibit enhanced prion-like seeding activity in mice. In: *Acta Neuropathol Commun.* 9(1):83 (2021)

[264] S, Brown ; T, Head-Gordon: Cool walking: A new Markov chain Monte Carlo sampling method. In: *J. Comput. Chem.* 24 (2003), S. 68–76

[265] S, Campioni ; MF, Mossuto ; S, Torrassa ; G, Calloni ; de Laureto PP ; A, Relini ; A, Fontana ; F, Chiti: Conformational properties of the aggregation precursor state of HypF-N. In: *J. Mol. Biol.* 379 (2008), S. 554–567

[266] S, Kumar ; JB, Udgaonkar: Conformational Conversion May Precede or Follow Aggregate Elongation on Alternative Pathways of Amyloid Protofibril Formation. In: *J. Mol. Biol.* 385 (2009)

[267] S, Kundu: Effects of different force fields on the structural character of α-synuclein β-hairpin peptide (35−56) in aqueous environment. In: *J. Biomol. Struct. Dyn.* 36 (2018), S. 302–317

[268] S, Piana ; A, Laio: A bias-exchange approach to protein folding. In: *J. Phys. Chem. B* 111 (2007), S. 4553−4559

[269] S, Piana ; AG, Donchev ; P, Robustelli ; DE, Shaw: Water Dispersion Interactions Strongly Influence Simulated Structural Properties of Disordered Protein States. In: *J. Phys. Chem. B* 119 (2015), S. 5113−5123

[270] S, Piana ; K, Lindorff-Larsen ; DE, Shaw: How Robust Are Protein Folding Simulations with Respect to Force Field Parameterization? In: *Biophys. J.* 100 (2011), S. L47–L49

[271] S, Samantray ; F, Yin ; B, Kav ; B, Strodel: Different Force Fields Give Rise to Different Amyloid Aggregation Pathways in Molecular Dynamics Simulations. In: *J. Chem. Inf. Model.* 60 (2020), S. 6462−6475

[272] S, Schilling ; U, Zeitschel ; T, Hoffmann ; U, Heiser ; M, Francke ; A, Kehlen ; M, Holzer ; B, Hutter-Paier ; M, Prokesch ; M, Windisch ; W, Jagla ; D, Schlenzig ; C, Lindner ; T, Rudolph ; G, Reuter: Glutaminyl cyclase inhibition attenuates pyroglutamate A [U+2424] and Alzheimer's disease- like pathology. In: *Nat. Med.* 14 (2008), S. 1106 –1111

[273] S, Yang ; H, Liu ; Y, Zhang ; H, Lu ; H, Chen: Residue-Specific Force Field Improving the Sample of Intrinsically Disordered Proteins and Folded Proteins. In: *J. Chem. Inf. Model.* 59 (2019), S. 4793–4805

[274] S, Yang ; MDW, Griffin ; KJ, Binger ; P, Schuck ; GJ, Howlett: An Equilibrium Model for Linear and Closed-Loop Amyloid Fibril Formation. In: *J. Mol. Biol.* 421 (2012), S. 364–377

[275] S, Zhang ; K, Iwata ; MJ, Lachenmann ; JW, Peng ; S, Li ; ER, Stimson ; Y, Lu ; AM, Felix ; JE, Maggio ; JP, Lee: In: *J. Struct. Biol.* 130 (2000)

[276] Sahoo, Bikash R. ; Cox, Sarah J. ; Ramamoorthy, Ayyalusamy: High-resolution probing of early events in amyloid-β aggregation related to Alzheimer's disease. In: *Chem. Commun.* 56 (2020), S. 4627–4639

[277] Saido, Takaomi C. ; Yamao-Harigaya, Wakako ; Iwatsubo, Takeshi ; Kawashima, Seiichi: Amino- and carboxyl-terminal heterogeneity of β-amyloid peptides deposited in human brain. In: *Neurosci. Lett.* 215 (1996), Sep, Nr. 3, S. 173–176. – ISSN 0304–3940

[278] Sanders, Hiromi M. ; Lust, Robert ; Teller, Jan K.: Amyloid-beta peptide Abetap3-42 affects early aggregation of full-length Abeta1-42. In: *Peptides.* 30 (2009), Nr. 5, S. 849–54

[279] Sauerbrey, Gunter: Use of oscillating crystals for weighing thin layers and for microweighing. In: *Magazine for physics* 159 (1959), S. 206–222

[280] SB, Padrick ; AD, Miranker: Islet Amyloid: Phase Partitioning and Secondary Nucleation Are Central to the Mechanism of Fibrillogenesis. In: *Biochemistry* 41 (2002), S. 4694–4703

[281] Scheidt, Holger A. ; Adler, Juliane ; Zeitschel, Ulrike ; Höfling, Corinna ; Korn, Alexander ; Krueger, Martin ; Rossner, Steffen ; Huster, Daniel: Pyroglutamate-Modified Amyloid (11- 40) Fibrils Are More Toxic than Wildtype Fibrils but Structurally Very Similar. In: *Chem. Eur. J.* 23 (2017), Nr. 62, S. 15834–15838

[282] Scheuner, D ; Eckman, C ; Jensen, M ; Song, X ; Citron, M ; Suzuki, N ; Bird, T D. ; Hardy, J ; Hutton, M ; Kukull, W ; Larson, E ; Levy-Lahada,

E ; Viitanen, M ; Peskind, E ; Poorkaj, P ; Schellenberg, G ; Tanzi, R ; W Wasco, L L. ; Selkoe, D ; Younkin, S: Secreted amyloid beta-protein similar to that in the senile plaques of Alzheimer's disease is increased in vivo by the presenilin 1 and 2 and APP mutations linked to familial Alzheimer's disease. In: *Nat. Med.* 2 (1996), Nr. 8, S. 864–870

[283] Schilling, Stephan ; Hoffmann, Torsten ; Manhart, Susanne ; Hoffmann, Matthias ; Demuth, Hans-Ulrich: Glutaminyl cyclases unfold glutamyl cyclase activity under mild acid conditions. In: *FEBS. Lett.* 563 (2004), Nr. 1-3, S. 191–6

[284] Schilling, Stephan ; Lauber, Thomas ; Schaupp, Michael ; Manhart, Susanne ; Scheel, Eike ; Bohm, Gerald ; Demuth, Hans-Ulrich: On the Seeding and Oligomerization of pGlu-Amyloid Peptides (in Vitro). In: *Biochemistry.* 45 (2006), Nr. 41, S. 12393–9

[285] Schlenzig, Dagmar ; Manhart, Susanne ; Cinar, Yeliz ; Kleinschmidt, Martin ; Hause, Gerd ; Willbold, Dieter ; Funke, Susanne A. ; Schilling, Stephan ; Demuth, Hans-Ulrich: Pyroglutamate Formation Influences Solubility and Amyloidogenicity of Amyloid Peptides. In: *Biochemistry.* 48 (2009), Nr. 29, S. 7072–8

[286] Schneider, Mario ; Walta, Stefan ; Cadek, Chris ; Richtering, Walter ; Willbold, Dieter: Fluorescence correlation spectroscopy reveals a cooperative unfolding of monomeric amyloid-β 42 with a low Gibbs free energy. In: *Sci. Rep.* 7 (2017), May, Nr. 2154, S. 1–8. – ISSN 2045–2322

[287] Schwierz, Nadine ; Frost, Christina V. ; Geissler, Phillip L. ; Zacharias, Martin: From Aβ Filament to Fibril: Molecular Mechanism of Surface-Activated Secondary Nucleation from All-Atom MD Simulations. In: *J. Phys. Chem. B* 121 (2017), Feb, Nr. 4, S. 671–682. – ISSN 1520–6106

[288] Schwierz, Nadine ; Frost, Christina V. ; Geissler, Phillip L. ; Zacharias, Martin: From Aβ Filament to Fibril: Molecular Mechanism of Surface-Activated Secondary Nucleation from All-Atom MD Simulations. In: *J. Phys. Chem. B.* 121 (2017), Nr. 4, S. 671–682

[289] Schützmann, Marie P. ; Hasecke, Filip ; Bachmann, Sarah ; Zielinski, Mara ; Hänsch, Sebastian ; Schröder, Gunnar F. ; Zempel, Hans ; Hoyer, Wolfgang: Endo-lysosomal Aβ concentration and pH trigger formation of Aβ oligomers that potently induce Tau missorting. In: *Nat. Commun.* 12

[290] Sciarretta, Kimberly L. ; Gordon, David J. ; Petkova, Aneta T. ; Tycko, Robert ; Meredith, Stephen C.: Aβ40-Lactam(D23/K28) Models a Conformation Highly Favorable for Nucleation of Amyloid. In: *Biochemistry* 44 (2005), Apr, Nr. 16, S. 6003–6014. – ISSN 0006–2960

[291] Sgourakis, Nikolaos G. ; Merced-Serrano, Myrna ; Boutsidis, Christos ; Drineas, Petros ; Du, Zheming ; Wang, Chunyu ; Garcia, Angel E.: Atomic-Level Characterization of the Ensemble of the Aβ(1â[U+0080][U+0093]42) Monomer

in Water Using Unbiased Molecular Dynamics Simulations and Spectral Algorithms. In: *J. Mol. Biol.* 405 (2011), Januar, Nr. 2, S. 570–583. – ISSN 0022–2836

[292] Sgourakis, Nikolaos G. ; Yan, Yilin ; McCallum, Scott A. ; Wang, Chunyu ; Garcia, Angel E.: The Alzheimer's Peptides Aβ40 and 42 Adopt Distinct Conformations in Water: A Combined MD / NMR Study. In: *J. Mol. Biol.* 368 (2007), May, Nr. 5, S. 1448–1457. – ISSN 0022–2836

[293] Shrake, A. ; Rupley, J. A.: Environment and exposure to solvent of protein atoms. Lysozyme and insulin. In: *J. Mol. Biol.* 79 (1973), Sep, Nr. 2, S. 351–371. – ISSN 0022–2836

[294] SI, Cohen ; S, Linse ; LM, Luheshi ; E, Hellstrand ; DA, White ; L, Rajah ; DE, Otzen ; M, Vendruscolo ; CM, Dobson ; TP, Knowles: Proliferation of amyloid-β42 aggregates occurs through a secondary nucleation mechanism. In: *Proc. Natl. Acad. Sci. USA* 110 (2013), S. 9758–9763

[295] SIA, Cohen ; M, Vendruscolo ; CM, Dobson ; TPJ, Knowles: From Macroscopic Measurements to Microscopic Mechanisms of Protein Aggregation. In: *J. Mol. Biol.* 421 (2012)

[296] SIA, Cohen ; M, Vendruscolo ; ME, Welland ; CM, Dobson ; EM, Terentjev ; TPJ, Knowles: Nucleated polymerization with secondary pathways. I. Determination of self-consistent solutions to growth processes described by non-linear master equations. In: *J. Chem. Phys.* 135 (2011)

[297] SIA, Cohen ; M, Vendruscolo ; ME, Welland ; CM, Dobson ; EM, Terentjev ; TPJ, Knowles: Nucleated polymerization with secondary pathways. I. Time evolution of the principal moments. In: *J. Chem. Phys.* 135 (2011)

[298] Sorensen, JM ; Hura, G ; Glaeser, RM ; Head-Gordon, T: What can x-ray scattering tell us about the radial distribution functions of water. In: *J. Chem. Phys.* 113 (2000), S. 9149–9161

[299] Šarić, Anđela ; Buell, Alexander K. ; Meisl, Georg ; Michaels, Thomas C. T. ; Dobson, Christopher M. ; Linse, Sara ; Knowles, Tuomas P. J. ; Frenkel, Daan: Physical determinants of the self-replication of protein fibrils. In: *Nat. Phys.* 12 (2016), Sep, Nr. 9, S. 874–880. – ISSN 1745–2481

[300] Straub, John E. ; Thirumalai, D.: Toward a Molecular Theory of Early and Late Events in Monomer to Amyloid Fibril Formation. In: *Annu. Rev. Phys. Chem.* 62 (2011), Mar, Nr. 1, S. 437–463. – ISSN 0066–426X

[301] Strodel, Birgit ; Barz, Bogdan: Computational Approaches for Understanding Dynamical Systems: Protein Folding and Assembly: Volume 170. In: *Elsevier Science Publishing Co Inc* (2020)

[302] Strodel, Birgit ; Barz, Bogdan: *Computational Approaches for Understanding Dynamical Systems: Protein Folding and Assembly: Volume 170.* San Diego, CA, USA : Academic Press Inc, Mar 2020. – ISBN 978–0–12821135–9

[303] Strooper, Bart D. ; Vassar, Robert ; Golde, Todd: The secretases: enzymes with therapeutic potential in Alzheimer disease. In: *Nat. Rev. Neurol.* 6 (2010), Nr. 2, S. 191–6

[304] Sugita, Yuji ; Okamoto, Yuko: Replica-exchange molecular dynamics method for protein folding. In: *Chem. Phys. Lett.* 314 (1999), November, Nr. 1â[U+0080][U+0093]2, S. 141–151. – ISSN 0009–2614

[305] Suzuki, N ; Cheung, T T. ; Cai, X D. ; Odaka, A ; Jr, L O. ; Eckman, C ; Golde, T E. ; Younkin, S G.: An increased percentage of long amyloid beta protein secreted by familial amyloid beta protein precursor (beta APP717) mutants. In: *Science.* 264 (1994), Nr. 5163, S. 1336–1340

[306] Swart, M ; van Duijnen, PTh: DRF90: Polarizable force field. In: *Mol. Sim.* 32 (2006), S. 471–484

[307] Szczepankiewicz, O. ; Linse, B. ; Meisl, G. ; Thulin, E. ; Frohm, B. ; Frigerio, C.S. ; Colvin, M.T. ; Jacavone, A.C. ; Griffin, R.G. ; Knowles, T. ; Walsh, D.M. ; Linse, S.: N-Terminal Extensions Retard Aβ42 Fibril Formation but Allow Cross-Seeding and Coaggregation with Aβ42. In: *J Am Chem Soc.* 137 (2015), Nr. 46, S. 14673–85

[308] T, Iwatsubo: The gamma-secretase complex: machinery for intramembrane proteolysis. In: *Curr. Opin. Neurobiol.* 14 (2004), S. 379–383

[309] Tarus, Bogdan ; Straub, JE ; Thirumalai, D: Dynamics of Asp23-Lys28 salt-bridge formation in A$\beta_{10\text{-}35}$ monomers. In: *J. Am. Chem. Soc.* 128 (2006)

[310] Thacker, Dev ; Sanagavarapu, Kalyani ; Frohm, Birgitta ; Meisl, Georg ; Knowles, Tuomas P J. ; Linse, Sara: The role of fibril structure and surface hydrophobicity in secondary nucleation of amyloid fibrils. In: *Proc. Natl. Acad. Sci. USA* 117 (2020), S. 25272–25283

[311] Todorova, N ; Legge, FS ; Treutlein, H ; Yarovsky, I: Systematic comparison of empirical force fields for molecular dynamics simulation of insulin. In: *J. Phys. Chem. B* 112 (2008), S. 11137–11146

[312] Tomaselli, Simona ; Esposito, Veronica ; Vangone, Paolo ; van Nuland, Nico A. J. ; Bonvin, Alexandre M. J. J. ; Guerrini, Remo ; Tancredi, Teodorico ; Temussi, Piero A. ; Picone, Delia: The α-to-β Conformational Transition of Alzheimer's Aβ-(1–42) Peptide in Aqueous Media is Reversible: A Step by Step Conformational Analysis Suggests the Location of β Conformation Seeding. In: *ChemBioChem* 7 (2006), Feb, Nr. 2, S. 257–267. – ISSN 1439–4227

[313] Tonda-Turo, Chiara ; Carmagnola, Irene ; Ciardelli, Gianluca: Quartz Crystal Microbalance With Dissipation Monitoring: A Powerful Method to Predict the *in vivo* Behavior of Bioengineered Surfaces. In: *Front. Bioeng. Biotechnol.* 6 (2018), S. 158

[314] Torrie, G. M. ; Valleau, J. P.: Nonphysical sampling distributions in Monte Carlo free-energy estimation: Umbrella sampling. In: *J. Comput. Phys.* 23 (1977), Feb, Nr. 2, S. 187–199. – ISSN 0021–9991

[315] TPJ, Knowles ; CA, Waudby ; GL, Devlin ; SIA, Cohen ; A, Aguzzi ; M, Vendruscolo ; EM, Terentjev ; ME, Welland ; CM, Dobson: An analytical solution to the kinetics of breakable filament assembly. In: *Science (New York N.Y.)* 326 (2009)

[316] TR, Jahn ; SE, Radford: Folding versus aggregation: Polypeptide conformations on competing pathways. In: *Arch. Biochem. Biophys.* 469 (2008)

[317] Törnquist, Mattias ; Linse, Sara: Chiral Selectivity of Secondary Nucleation in Amyloid Fibril Propagation. In: *Angew. Chem. Int. Ed.* 60 (2021), S. 24008–24011

[318] Törnquist, Mattias ; Michaels, Thomas C T. ; Sanagavarapu, Kalyani ; Yang, Xiaoting ; Meisl, Georg ; Cohen, Samuel I A. ; Knowles, Tuomas P J. ; Linse, Sara: Secondary nucleation in amyloid formation. In: *Chem. Commun.* 54 (2018), S. 8667–8684

[319] Vega, C ; Abascal, JLF ; Conde, MM ; Aragones, JL: What ice can teach us about water interactions: a critical comparison of the performance of different water models. In: *Faraday Discuss* 141 (2009), S. 251–276

[320] Viswanathanand, A ; Greenberg, SM: Cerebral amyloid angiopathy in the elderly. In: *Ann. Neurol.* 70 (2011), S. 871–880

[321] Vivekanandan, Subramanian ; Brender, Jeffrey R. ; Lee, Shirley Y. ; Ramamoorthy, Ayyalusamy: A partially folded structure of amyloid-beta(1-40) in an aqueous environment. In: *Biochem. Biophys. Res. Commun.* 411 (2011), S. 312–316

[322] Vögeli, Beat ; Ying, Jinfa ; Grishaev, Alexander ; Bax, Ad: Limits on Variations in Protein Backbone Dynamics from Precise Measurements of Scalar Couplings. In: *J. Am. Chem. Soc.* 129 (2007), Aug, Nr. 30, S. 9377–9385. – ISSN 0002–7863

[323] VT, Duong ; M, Thapa ; R, Luo: Improved Accuracy and Convergence of Intrinsically Disordered Protein Molecular Dynamics Simulations Using the ff14IDPSFF Force Field. In: *Biophys. J.* 114 (2018), S. 432A−432A

[324] W, Kang ; F, Jiang ; YD, Wu: Universal Implementation of a Residue-Specific Force Field Based on CMAP Potentials and Free Energy Decomposition. In: *J. Chem. Theory Comput.* 14 (2018), S. 4474−4486

[325] W, Wang ; W, Ye ; C, Jiang ; R, Luo ; HF, Chen: New Force Field on Modeling Intrinsically Disordered Proteins. In: *Chem. Biol. Drug Des.* 84 (2014), S. 253–269

[326] W, Ye ; Ji ; DJ ; W, Wang ; R, Luo ; HF, Chen: Test and Evaluation of ff99IDPs Force Field for Intrinsically Disordered Proteins. In: *J. Chem. Inf. Model.* 55 (2015), S. 1021−1029

[327] Wang, Lingle ; Friesner, Richard A. ; Berne, B. J.: Replica Exchange with Solute Scaling: A More Efficient Version of Replica Exchange with Solute Tempering (REST2). In: *J. Phys. Chem. B* 115 (2011), August, Nr. 30, S. 9431–9438. – ISSN 1520–6106

[328] Wang, ZX ; Zhang, W ; Wu, C ; Lei, H ; Cieplak, P ; Duan, Y: Strike a balance: Optimization of backbone torsion parameters of AMBER polarizable force field for simulations of proteins and peptides. In: *J. Comput. Chem.* 27 (2006), S. 781–790

[329] Warshel, A ; Kato, M ; Pisliakov, AV: Polarizable force fields: History, test cases and prospects. In: *J. Chem. Theory Comput.* 101 (2007), S. 2034—-2045

[330] Weiffert, T. ; Meisl, G. ; Flagmeier, P. ; De, S. ; Dunning, C.J.R. ; Frohm, B. ; Zetterberg, H. ; Blennow, K. ; Portelius, E. ; Klenerman, D. ; Dobson, C.M. ; Knowles, T.P.J. ; Linse, S.: Increased Secondary Nucleation Underlies Accelerated Aggregation of the Four-Residue N-Terminally Truncated Aβ42 Species Aβ5-42. In: *ACS Chem. Neurosci.* 10 (2019), Nr. 5, S. 2374–84

[331] Wennmalm, Stefan ; Chmyrov, Volodymyr ; Widengren, Jerker ; Tjernberg, Lars: Highly Sensitive FRET-FCS Detects Amyloid β-Peptide Oligomers in Solution at Physiological Concentrations. In: *Anal. Chem.* 87 (2015), Dec, Nr. 23, S. 11700–11705. – ISSN 0003–2700

[332] Willbold, Dieter ; Strodel, Birgit ; Schröder, Gunnar F. ; Hoyer, Wolfgang ; Heise, Henrike: Amyloid-type Protein Aggregation and Prion-like Properties of Amyloids. In: *Chem. Rev.* 121 (2021), Jul, Nr. 13, S. 8285–8307. – ISSN 0009–2665

[333] WP, Esler ; ER, Stimson ; JM, Jennings ; HV, Vinters ; JR, Ghilardi ; JP, Lee: Alzheimer's disease amyloid propagation by a template-dependent dock-lock mechanism. In: *Biochemistry* 39 (2000), S. 6288–6295

[334] WS, Gosal ; IJ, Morten ; EW, Hewitt ; DA, Smith ; NH, Thomson ; SE, Radford: Competing Pathways Determine Fibril Morphology in the Self-assembly of β2-Microglobulin into Amyloid. In: *J. Mol. Biol.* 89 (2005)

[335] Wulff, Melanie ; Baumann, Monika ; Thümmler, Anka ; Yadav, Jay K. ; Heinrich, Liesa ; Knüpfer, Uwe ; Schlenzig, Dagmar ; Schierhorn, Angelika ; Rahfeld, Jens-Ulrich ; Horn, Uwe ; Balbach, Jochen ; Demuth, Hans-Ulrich ; Fändrich, Marcus: Enhanced Fibril Fragmentation of N-Terminally Truncated and Pyroglutamyl-Modified A Peptides. In: *Angew. Chem. Int. Ed.* 55 (2016), Nr. 16, S. 5081–4

[336] Wälti, Marielle A. ; Ravotti, Francesco ; Arai, Hiromi ; Glabe, Charles G. ; Wall, Joseph S. ; Böckmann, Anja ; Güntert, Peter ; Meier, Beat H. ; Riek, Roland: Atomic-resolution structure of a disease-relevant Aβ(1–42) amyloid fibril. In: *Proc. Natl. Acad. Sci.* 113 (2016), August, Nr. 34, S. E4976–E4984. – ISSN 0027–8424, 1091–6490

[337] X, Jiang ; Y, Cao ; W, Han: In silico study of recognition between Aβ40 and Aβ40 fibril surfaces: an N-terminal helical recognition motif and its implications for inhibitor design. In: *ACS. Chem. Nerosci.* 9 (2018), Nr. 5, S. 935—-944

[338] Xiao, Yiling ; Ma, Buyong ; McElheny, Dan ; Parthasarathy, Sudhakar ; Long, Fei ; Hoshi, Minako ; Nussinov, Ruth ; Ishii, Yoshitaka: Aβ(1-42) fibril structure illuminates self-recognition and replication of amyloid in Alzheimer's disease. In: *Nat. Struct. Mol. Biol.* 22 (2015), Juni, Nr. 6, S. 499–505. – ISSN 1545–9993

[339] Xiao, Yiling ; Ma, Buyong ; McElheny, Dan ; Parthasarathy, Sudhakar ; Long, Fei ; Hoshi, Minako ; Nussinov, Ruth ; Ishii, Yoshitaka: Aβ(1–42) fibril structure illuminates self-recognition and replication of amyloid in Alzheimer's disease. In: *Nat. Struct. Mol. Biol.* 22 (2015), Jun, Nr. 6, S. 499–505. – ISSN 1545–9985

[340] Y, Chebaro ; X, Dong ; R, Laghaei ; P, Derreumaux ; N, Mousseau: Replica Exchange Molecular Dynamics Simulations of Coarse-grained Proteins in Implicit Solvent. In: *J. Phys. Chem. B* 113 (2009), S. 267−274

[341] Y, Hori ; T, Hashimoto ; Y, Wakutani ; K, Urakami ; K, Nakashima ; MM, Condron ; S, Tsubuki ; TC, Saido ; DB, Teplow ; T, Iwatsubo: The Tottori (D7N) and English (H6R) familial Alzheimer disease mutations accelerate Abeta fibril formation without increasing protofibril formation. In: *J. Biol. Chem.* 282 (2007)

[342] Y, Sekijima ; RL, Wiseman ; J, Matteson ; P, Hammarström ; SR, Miller ; AR, Sawkar ; WE, Balch ; JW, Kelly: The Biological and Chemical Basis for Tissue-Selective Amyloid Disease. In: *Cell* 121 (2005)

[343] Y, Sugita ; A, Kitao ; Y, Okamoto: Multidimensional replica-exchange method for free-energy calculations. In: *J. Chem. Phys.* 113 (2000), S. 6042–6051

[344] Y, Sugita ; Y, Okamoto: Replica-exchange multicanonical algorithm and multicanonical replica-exchange method for simulating systems with rough energy landscape. In: *Chem. Phys. Lett.* 329 (2000), S. 261–270

[345] Y, Zhang ; H, Liu ; S, Yang ; R, Luo ; HF, Chen: Well-Balanced Force Field ff03CMAP for Folded and Disordered Proteins. In: *J. Chem. Theory Comput.* 15 (2019), S. 6769–6780

[346] Y, Zhang ; Y, Zhou ; L, He ; Y, Fu ; W, Zhang ; J, Hu ; Z, Shi: Hydration effects on Leu's polyproline II population in AcLXPNH2. In: *Chem. Commun.* 54 (2018), S. 5764−5767

[347] Yan, Yilin ; McCallum, Scott A. ; Wang, Chunyu: M35 Oxidation Induces Aβ40-like Structural and Dynamical Changes in Aβ42. In: *J. Am. Chem. Soc.* 130 (2008), Apr, Nr. 16, S. 5394–5395. – ISSN 0002–7863

[348] Yan, Yilin ; Wang, Chunyu: Abeta42 is more rigid than Abeta40 at the C terminus: implications for Abeta aggregation and toxicity. In: *J. Mol. Biol.* 364 (2006), S. 853–862

[349] Yang, Yang ; Arseni, Diana ; Zhang, Wenjuan ; Huang, Melissa ; Lövestam, Sofia ; Schweighauser, Manuel ; Kotecha, Abhay ; Murzin, Alexey G. ; Peak-Chew, Sew Y. ; Macdonald, Jennifer ; Lavenir, Isabelle ; Garringer, Holly J. ; Gelpi, Ellen ; Newell, Kathy L. ; Kovacs, Gabor G. ; Vidal, Ruben ; Ghetti, Bernardino ; Ryskeldi-Falcon, Benjamin ; Scheres, Sjors H W. ; Goedert, Michel: Cryo-EM structures of amyloid-β 42 filaments from human brains. In: *Science.* 375 (2022), Nr. 6577, S. 167–172

[350] Yeh, IC ; Hummer, G: Peptide loop-closure kinetics from microsecond molecular dynamics simulations in explicit solvent. In: *J. Am. Chem. Soc.* 124 (2002), S. 6563–6568

[351] Young, Laurence J. ; Schierle, Gabriele S. K. ; Kaminski, Clemens F.: Imaging Aβ(1–42) fibril elongation reveals strongly polarised growth and growth incompetent states. In: *Phys. Chem. Chem. Phys.* 19 (2017), Oct, Nr. 41, S. 27987–27996. – ISSN 1463–9084

[352] Zhao, Li N. ; Lu, Lanyuan ; Chew, Lock Y. ; Mu, Yuguang: Alzheimer's disease–a panorama glimpse. In: *Int. J. Mol. Sci.* 15 (2014), Nr. 7, S. 12631–50

[353] Zheng, Weihua ; Tsai, Min-Yeh ; Chen, Mingchen ; Wolynes, Peter G.: Exploring the aggregation free energy landscape of the amyloid-β protein (1-40). In: *Proc. Natl. Acad. Sci. USA.* 113 (2016), S. 11835–11840

[354] Zurdo, J ; Guijarro, JI ; Jiménez, JL ; Saibil, HR ; Dobson, CM: Dependence on solution conditions of aggregation and amyloid formation by an SH3 domain. In: *J Mol Biol.* 311 (1998), S. 325–40

[355] Šarić, A. ; Buell, A.K. ; Meisl, G. ; Michaels, T.C.T. ; Dobson, C.M. ; Linse, S. ; Knowles, T.P.J. ; Frenkel, D.: Physical determinants of the self-replication of protein fibrils. In: *Nat. Phys.* 12 (2016), Nr. 9, S. 874–880